Constraining calving dynamics of marine-terminating glaciers: Developing 4D data of Store Glacier, Greenland, from repeat UAV photography

Jonathan Vautrey

Scott Polar Research Institute,
University of Cambridge

Abstract

In the past few decades several of the Greenland Ice Sheet's (GISs) marine-terminating outlet glaciers have shown patterns of swift retreat and thinning, but the mechanism of calving, which controls this loss, is still not fully constrained. This research uses UAV-borne remote sensing data to analyse the calving events of Store Glacier, west Greenland, in order to develop our knowledge of this important glaciological process. Repeat aerial photography of the terminus of Store Glacier were collected by the RESPONDER project. These images were taken and run through photogrammetry software in order to produce 3D point clouds, and ultimately orthomosaics and DEMs of the calving front at a 20 cm spatial resolution. By doing this for the multiple sorties carried out by the UAV, 4D data was created, permitting detailed analysis of crevassing and calving processes over a 5-day period at a sub-daily temporal scale. Maps of the crevasses across the glacier front for each survey were produced through Gaussian blurring of the DEMs, and show a clear progression of the fractures over time. However, there is no strong connection between the crevasse patterns and observed calving events throughout the study period at this aerial view.

The orientation of crevasses across moving and fixed transects, 100 m and 150 m from the glacier front respectively, were also obtained. Additionally, the principal axes of strain within the ice across the caving front were calculated from surface velocity and strain rate components. These two datasets were compared and reveal the influence of both Mode I and Mode III fracturing in the formation of crevasses across Store Glacier's snout, with mixed mode fracturing also being common in some regions. But, the basal topography of the bed and overdeepening below Store Glacier may also play a key factor in controlling these patterns and the types of crevasses observed on the glacier surface.

Finally, measurements of the dimensions of crevasses across these transects, plus depth profiles longitudinally up the glacier, show that the monitoring of individual crevasses provides a more robust method of determining how crevasse propagation influences the occurrence of calving events compared to their mass-measurement. A diurnal cycle of crevasse deepening is revealed, while the debutressing of the glacier front following a calving event seemingly also helps other surface crevasses and rifts to propagate due to the spread of tensile stresses in the local area. However, basal crevasses are also likely to contribute to the calving at Store Glacier and attempts should be made to continually monitor their development at the same time as surface crevasses in order to improve our understanding of the crevasse-calving relationship.

Acknowledgements

There are a number of expressions of gratitude I must give for those who have provided help and support in order for me to complete this thesis.

I am indebted to my supervisor, Dr Poul Christoffersen, who has provided much support and knowledge throughout the development and writing of this report. Thank you too to the rest of the RESPONDER team for initially collecting the data used in this study in the field at Store Glacier, Greenland, and permitting me to analyse it further. Particular mention must go to Thomas Chudley for not only obtaining the initial data, but also for processing the photographs using structure from motion photogrammetry to produce the DEMs and orthomosaics, in addition to providing the velocity fields and velocity component data. His continued support during both the analysis and write-up process was much appreciated.

Thank you also to Vandan Parmar for his help with processing and understanding concepts behind the research. And finally thanks to my parents for their constant support and encouragement throughout this process.

RESPONDER

UNIVERSITY OF CAMBRIDGE

Contents

List of Figures

Cover Page

Photograph of surface crevasse observed on Store Glacier (captured by members of the RESPONDER team in 2017).

Introduction

Literature Review

Methodology

Results

Discussion

List of Tables

1. INTRODUCTION

1.1 Introduction and Rationale

Observed changes in contemporary climate have had significant impacts on the retreat of glaciers across the globe (Kaser *et al.*, 2004; Mark *et al.*, 2010). Several of the Greenland Ice Sheet's (GIS's) marine-terminating outlet glaciers have particularly shown patterns of swift retreat and thinning in the past few decades (Joughin *et al.*, 2010; Pritchard *et al.*, 2009). This ice loss is contributed to a combination of iceberg calving from the glacier front and surface meltwater runoff. Calving in particular has been a major component of Greenlandic ice loss over recent decades, comprising two thirds of the total net annual ice loss from 2000 to 2009 (Rignot and Kanagaratnam, 2006), and between one third and one half since 2010 (Enderlin et al., 2014). However, despite this, the process of iceberg calving is still not fully constrained and much more needs to be understood about the multifaceted processes involved (Benn *et al.*, 2007).

One big factor that is critical to this understanding is the connection between the development of crevasses across glaciers with the occurrence of calving events. Crevasses are brittle fractures that identify the stress patterns within a body of ice (Colgan *et al.*, 2016; Harper *et al.*, 1998), and are one of the main shared features between glaciers, ice shelves and ice sheets across the globe. Calving is suggested to transpire when the propagation of surface and basal crevasses down and up respectively cuts through the entire thickness of a glacier front (Nick *et al.*, 2010). However, while this criterion for crevasse depth calving has been employed to a number of one or two dimensional models (Cook *et al.*, 2012, 2014; Pollard *et al.*, 2015; Todd and Christoffersen, 2014), its application with three dimensional models and data has only just been carried out (Todd *et al.*, 2018). Additionally, despite the improvements in temporal and spatial resolution of satellite imagery to allow the tracking of crevasse movements between recurring imagery (Colgan *et al.*, 2011; Glasser and Scambos, 2008; Glasser *et al.*, 2009), little work has been carried out at finite temporal scales with daily and sub-daily repeat surveys.

Unmanned aerial vehicles (UAVs), aircraft navigated through on-board computers or remote human control, are an emerging technology that is providing a low-cost alternative to repeat aerial imagery surveys (Bhardwaj *et al.*, 2016). Their effectiveness to provide cloud-free, high-resolution images at a chosen high temporal scale reduces the number of compromises

that must be made by researchers compared to when using other satellite alternatives (Immerzel *et al.*, 2017; Whitehead *et al.*, 2013).

In addition, aerial surveys by UAVs have helped facilitate a rise in the use of structure from motion (SfM) photogrammetry in glacial regions (Gindraux *et al.*, 2017; Westoby *et al.*, 2012). SfM uses the stereoscopic images captured by UAVs to construct high-resolution orthorectified images (orthophotos / orthomosaics) and digital elevation models (DEMs; Immerzeel *et al.*, 2014; James and Robson, 2012). The technique's currently unmatched resolution quality can be employed at a vast variety of temporal (sub-second to decades) and spatial (sub-millimetre to kilometres) scales (Eltner *et al.*, 2016). Thus, UAV imagery and its subsequent analysis through SfM photogrammetry provide an important opportunity to explore sub-daily and daily changes in glacial environments.

This study analyses the crevasse patterns and calving events at the snout of Store Gletscher (Glacier), a marine-terminating glacier on the western side of the GIS. A high resolution and sub-daily temporal approach using imagery captured by UAVs and processing though SfM photogrammetry has been utilised to assess what influences crevasse development has on iceberg calving.

1.2 Significance of the Research

In order to more accurately constrain sea level models and the impact that glacier and ice sheets will have on the rises in sea level of the 21st century and beyond, our knowledge of the processes behind iceberg calving events must first be improved. The analysis undertaken in this research project will advance this understanding by exploring the sub-daily calving events occurring at the snout of Store Glacier over a five-day period in July 2017. Specifically, the crevasse depth calving criterion will be assessed by examining the connections between crevasse development and calving events over the study period.

This study will provide one of the first evaluations of calving mechanics over both such a high spatial and temporal resolution. The application of new emerging techniques, such as UAVs and SfM, will additionally permit a four dimensional assessment of these processes to take place by analysing changes in crevasse length, width and depth over time. Through this improvement of our present scientific knowledge of crevassing and calving mechanics, our ability to accurately and reliably assess the impact of contemporary climate change on glacier behaviour could be considerably enhanced.

1.3 Aims and Objectives

1.3.1 Research Aims

This research aims to assess the sub-daily connections between crevasse development and calving events at the snout of Store Glacier, west Greenland. Through the production of orthomosaics and DEMs, four dimensional spatial and temporal patterns of change will be investigated and analysis will be done to understand why these changes have occurred.

1.3.2 Research Objectives

1. **To examine the changes in crevasse patterns of Store Glacier at a sub-daily scale and whether this relates to the observed occurrence of calving events across the glacier front**

Aerial imagery taken from sub-daily frequency UAV surveys will be put through SfM photogrammetry software in order to produce a series of orthomosaics and DEMs to allow crevasses along the snout to be mapped and an insight gained into the progression of fractures. Key calving events over the study period shall also be identified and the total area of icebergs calved between each survey calculated in order to compare to any changes in crevasse pattern.

2. **To investigate how the dynamics of the ice and forces acting within it impact on the types of crevassing observed at the surface of the calving front**

Crevasse orientation for each fracture along defined fixed and moving transects will be measured and compared to the principal angle of strain for that region of the glacier front. Velocity profiles of the snout will also be used to help identify key crevasse types.

3. **To assess the growth and propagation of crevasses along the calving front of Store Glacier at a high temporal frequency and how their growth links to the incidence of calving events**

The dimensions of crevasses will be measured along the specified fixed and moving transects and statistical analysis shall be employed to reveal any significant changes over time and determine the key processes affecting crevasse growth. Moreover, depth profiles will be taken using the produced DEMs for each time slice at the location of the key calving

events in order to identify any significant propagation of crevasses during the study period that led to a calving event.

1.4 Study Area

Store Glacier (70°24’ N, 50°32’ W) is a marine-terminating (tidewater) outlet glacier on the western side of the Greenlandic Ice Sheet, situated in the Uummannaq district (Figure 1.1). The Uummannaq region includes eleven marine-terminating outlet glaciers altogether that drain into a shared fjord system. This fjord system leads into a channel measuring 50 km in width (Howat *et al*, 2010) before connecting to Baffin Bay through the Uummannaq Trough.

Store Glacier’s calving front has a visible freeboard height of up to 110 m above sea level and a width of 5.3 km (Ahn and Box, 2010). The terminus is located at the narrowing of a lateral valley, where a velocity of approximately 5,800 m yr^{-1} / 16 m d^{-1} is usually reached (Todd *et al.*, 2018). Over the period of a year the glacier seasonally advances and retreats

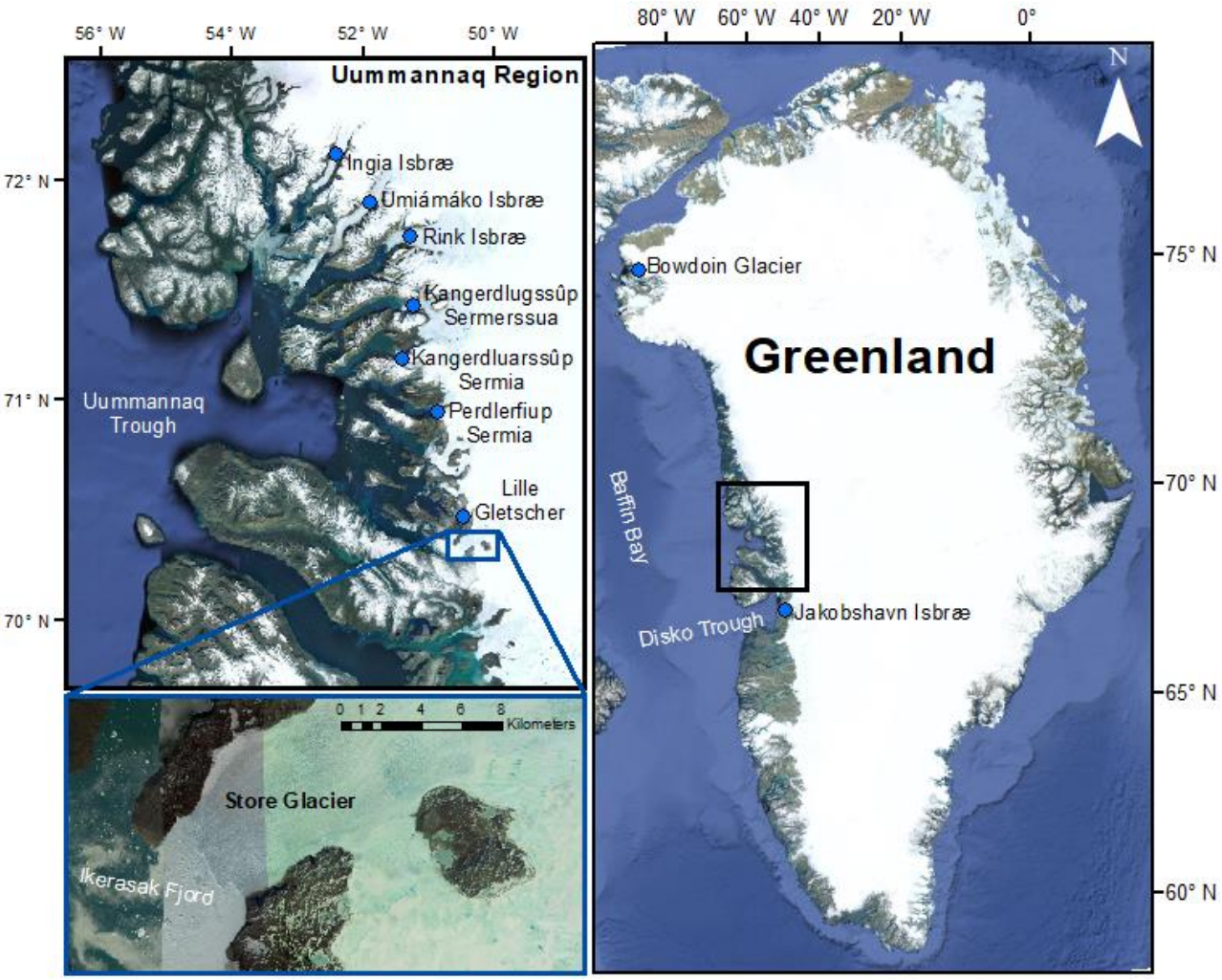

Figure 1.1: *Map of Greenland, with insets of Ummannaq Region and Store Glacier, detailing the location of sites referred to in this study. Landsat/Copernicus imagery taken from Google Earth Pro (2016).*

up to 400 m (Howat *et al.*, 2010). Of the outlet glaciers located in West Greenland, Store Glacier ranks as the second biggest overall in regards to ice flux (Weidick & Bennike, 2007).

Additionally, bathymetry measurements indicate Store Glacier's terminus sits upon a sill situated approximately 450 m below sea level (Morlighem *et al.*, 2014; Rignot *et al*., 2015). Downstream, the Ikerasak Fjord, into which the glacier calves, is between 700 and 800 m deep (Figure 1.2; Morlighem *et al.*, 2014). Inland, Store Glacier flows for 30 km along an overdeepening, which attains a depth of 900 m below sea level (Todd *et al.*, 2018). The full ice catchment of the glacier continues to the ice divide, 280 km away, and drains a 30,500 km^2 catchment basin into the Atlantic Ocean (Rignot and Mouginot, 2012).

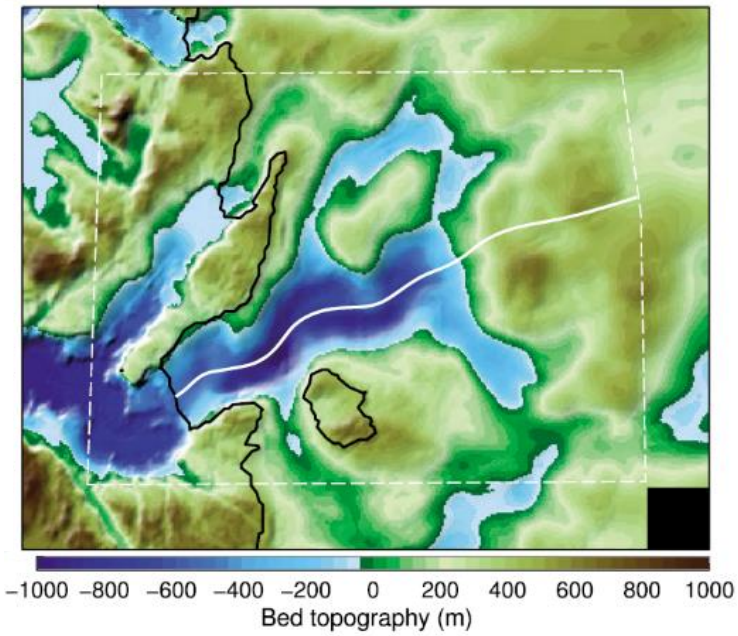

Figure 1.2: *Bed topography underneath and around Store Glacier. The black line indicates the ice edge, while the white line shows the central flow line of the glacier. Taken from Morlighem et al. (2016).*

2. LITERATURE REVIEW

2.1 Glacial History

2.1.1 West Greenland

Greenland's glacial history since the Last Glacial Maximum has been recorded through the use of numerous dating techniques, including carbon-14 dating of marine cores (Ó Cofaigh *et al.*, 2013), cosmogenic nuclide surface exposure dating (Håkansson *et al.*, 2008), identification of moraines (Long and Roberts, 2002) and geophysical analysis of the continental shelf (Evans *et al.*, 2009). It is now believed that during the Last Glacial Maximum (~26.5-19 ka BP) much of the GIS, including the western margin, extended to the continental shelf break at its peak extent (Funder and Hansen, 1996; Ó Cofaigh *et al.*, 2004; Weidick *et al.*, 2004; Williams, 1993). In the west, the ice sheet's initial retreat from this maximum extent has been dated to 14,880 cal yr BP at the mouth of the Uummannaq trough and 13,800 cal yr BP at the edge of Disko trough (Figure 1.1; Ó Cofaigh *et al.*, 2013). This western ice then retreated onto land by approximately 9,000 cal yr BP (Donner and Jungner, 1975; Weidick, 1972), before reaching its current position.

Over the past two decades, however, it has been possible to observe changes in the GIS durectly. Studies of the net mass loss from the GIS show it has accelerated substantially (Howat *et al.*, 2007; Khan *et al.*, 2010; Velicogna, 2009). This has predominantly been attributed to a combination of increased supraglacial meltwater production (Hanna, 2005; van den Broeke *et al.*, 2009), plus the acceleration and increased calving of fjord-terminating outlet glaciers (Luckman and Murray, 2005; Howat et al., 2005), such as Store Glacier and others in the Uummannaq region. Such marine-terminating glaciers dominate the sum ice discharge of the GIS to the ocean (Rignot and Mouginot, 2012) and the highest concentration of outlet glaciers across Greenland is presently in the central west region (Reeh, 1985; Velicogna and Wahr, 2006). As well as the Uummannaq glaciers this includes Jakobshavn Isbræ, Greenland's largest outlet glacier (Echelmeyer *et al.*, 1991) located in the Disko Bugt region (Figure 1.1), which saw a swift acceleration from approximately 4,000 m a^{-1} to 17,000 m a^{-1} between 1995 and 2012 following the persistent retreat of its calving front (Joughin et al., 2012, 2014a).

Changes in atmospheric conditions were originally believed to be the dominant control of these increases (Zwally *et al.*, 2002a). However, after further research, a consensus has been reached detailing that oceanic forces have chiefly driven these recent observations

(Hanna *et al.*, 2009; Holland *et al.*, 2008; Murray *et al.*, 2010). It is proposed that a pulse of warm Atlantic water encroached into Greenland's fjords near the beginning of the 21st century (Christoffersen *et al.*, 2011; Straneo *et al.*, 2010). This pulse has been linked to a dominance of calving within the 2000's, with the process comprising the majority of ice loss from the GIS during that decade (Rignot and Kanagaratnam, 2006), but less so since (Enderlin et al., 2014). Thus, the calving of marine-terminating glaciers around the GIS, and particularly the western fjords, is believed to be particularly sensitive to oceanic influences (Holland *et al.*, 2008).

2.1.2 Uummannaq Region

The majority of Uummannaq glaciers have undergone retreat over the past 50 years. A number have seen retreat of between 1 and 1.5 km, including Kangerdluarsuup Sermia (1.5 km since 1964), Rink Isbræ (1.4 km retreat since 1964) and Lille Gletscher (1.2 km since 1989) (Rignot *et al.*, 2016). This retreat has continued over recent decades, with retreat rates between 400 and 800 m a^{-1} witnessed from 1992 to 2000 by Moon and Joughin (2008). Into the start of the millennium, however, a number of glaciers saw reduced discharge rates, with Rignot and Kanagaratnam (2006) observing more stable conditions at Rink Isbræ and Umiámáko Isbræ within a five-year period from November 2000 to April 2005. Rink Isbræ has continued to be quasi-stable since 2005 (Box and Decker, 2011; Moon *et al.*, 2014).

Nevertheless, several of the Uummannaq glaciers have continued to undergo substantial retreat over the past 20 years. Rignot and Kanagaratnam (2006) noted that the retreat rate of Kangerdlugssûp Sermerssua more than doubled between November 2000 and April 2005. Moreover, since 2002, Rignot *et al.* (2016) report that Ingia Isbræ, Umiámáko Isbræ and Perdlerfiup Sermia retreated 6.8 km, 3.5 km and 2.8 km respectively.

2.1.3 Store Glacier

Despite the retreat of other glaciers in the Uummannaq region over recent decades (Howat *et al.*, 2010), the frontal position and velocity of Store Glacier has remained relatively stable (Joughin *et al.*, 2008a; Rignot *et al.*, 2015). Indeed, aerial imagery has shown that the glacier's position has continued to remain comparatively unchanged since at least 1948 (Weidick, 1995), with further evidence to suggest this stable period has lasted for a century (Weidick and Bennike, 2007), or even since the Little Ice Age (Weidick, 1968). It is proposed that this stability is attributable to the glacier being pinned to the basal sill, as well as being located at the narrowing of a lateral valley (Todd *et al.*, 2018).

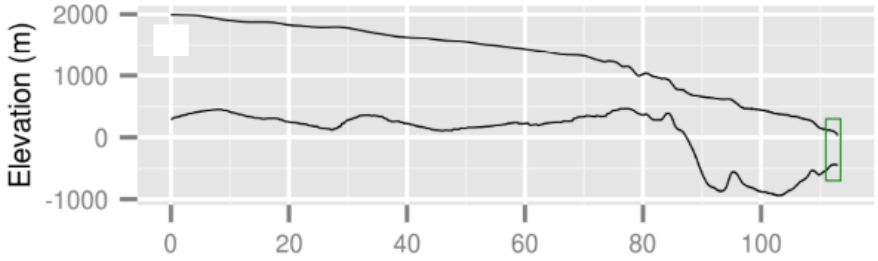

Figure 2.1: *Surface and basal topography of Store Glacier along a central flow line showing the retrograde bed at the snout. Taken from Todd and Christoffersen (2014).*

An additional influence on the position of Store Glacier's calving front and its calving activity is the seasonal development of firm proglacial mélange, a compact group of calved icebergs held together by sea ice without a clearly defined floe (Amundson *et al.*, 2010). The mélange usually develops between late January and early February and persists until the end of May (Howat *et al.*, 2010). Its growth applies a substantial buttressing force on the glacier's snout, which can be determined from the calving front's velocity perturbation at the time of mélange breakup. Walter *et al.* (2012) calculate a velocity perturbation of approximately 1.5 m d^{-1} and subsequent buttressing force of 30-60 kPa using time-lapse photography during late May 2008. However, using repeat imagery from sorties by UAVs in early June 2014 (Hubbard *et al.*, 2015; Toberg *et al.*, 2016), Todd *et al.* (2018) deduce a higher buttressing force of 120 kPa from a velocity perturbation of approximately 4 m d^{-1}.

Despite this stability however, it is important to note that due to the overdeepening immediately behind the sill upon which Store Glacier is currently pinned, the bed slope inland of the glacier's present position is retrograde (Figure 2.1). Thus, if Store Glacier was to retreat in the future following an increase in calving and surface meltwater production, as a result of rising oceanic and atmospheric temperatures, a process of systematic, unstoppable retreat could ensue for 30 km (Figure 2.2) as outlined by the marine ice sheet instability theory (Favier *et al.*, 2014; Joughin *et al.*, 2014b; Weertman, 1974).

2.2 Advent and Use of UAVs in Glaciological Research

Continual observation of crevassing and calving through continuous fieldwork-based surveys is often unfeasible due to difficulties with accessing the study area, and the significant funds and resources that would be required (Bhardwaj *et al.*, 2015). Additionally, despite the effectiveness of satellite-based remote sensing techniques in monitoring glaciers and ice sheets (Arnold *et al.*, 2006; Quincey and Luckman, 2009; Solbø and Storvold, 2013), this approach is still often limited by high costs, the incidence of measurements and procuring imagery that is cloud-free, which results in compromises between the scale,

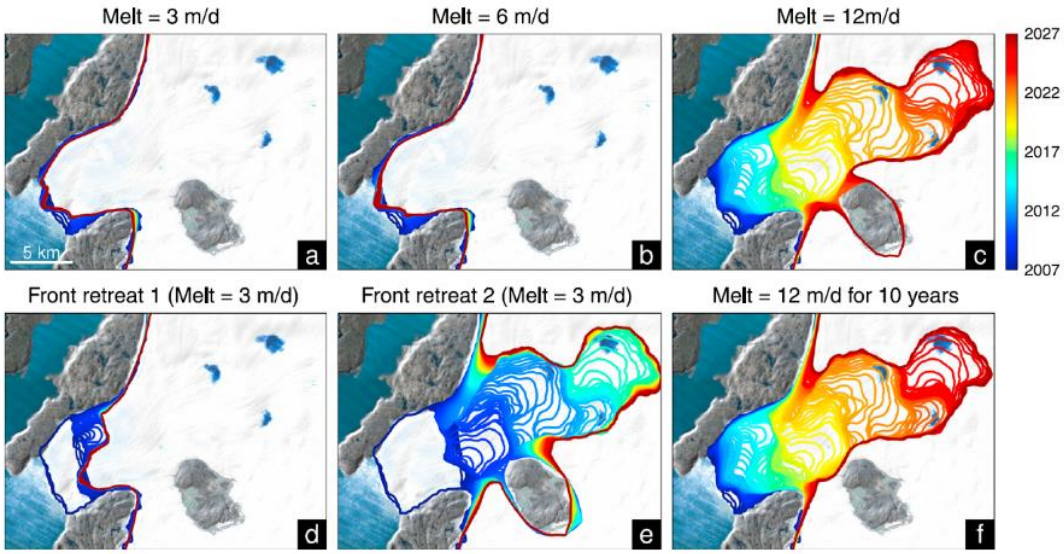

Figure 2.2: *Ice front positions of Store Glacier from 2007 to 2027 modelled under varying melt scenarios demonstrating the possibility for unstoppable retreat. Taken from Morlighem et al. (2016).*

resolution and occurrence of data used in studies (Whitehead *et al.*, 2013). However, the advent of UAVs with the ability to transport a variety of remote sensing equipment has resulted in a new lower cost opportunity for the monitoring of glacier crevasses and calving events (Bhardwaj *et al.*, 2016).

2.2.1 Advent

The introduction of UAVs and their early development occurred during the First World War, with military endeavours in both the United States of America and United Kingdom seeking to manufacture an UAV packed with explosive material (Bhardwaj *et al.*, 2016). Civilian use of UAVs commenced in the late 20th century when test flights of model helicopters and fixed wings were carried out, often with cameras attached (Przybilla and Wester-Ebbinghaus, 1979; Wester-Ebbinghaus, 1980). This provided a basis for using UAVs for the mapping of geographical locations and the utilisation of UAVs for scientific purposes became easier following the investment of private firms and further enhancements of hardware and software.

Initial UAV surveys were undertaken in Alaska in 1999, where meteorological measurements were obtained (Curry *et al.*, 2004). The first study using an UAV in the Arctic was subsequently published in 2007, with Hodson *et al.* (2007) recording the spatial gradient in the ration of cryoconite forms using a 323 Heli Ball system. There has subsequently been a growth in UAV based research across the Earth Sciences (e.g. d'Oleire-Oltmanns *et al.*, 2012; Hugenholtz *et al.*, 2012, 2013; Kääb *et al.*, 2014).

2.2.2 Use

In glaciology the functionality of UAVs is primarily influenced by the payloads that they carry. At their most basic, UAVs are fitted with a GPS to provide a detailed geolocation of the vehicles location, as well as autopilot and flight planning capabilities (Bhardwaj *et al.*, 2016). Digital cameras are also regular fixtures and are able to provide researchers with a considerable amount of data (e.g. Ayala *et al.*, 2016; Corripio, 2004; Dumont *et al.*, 2011; Garvelmann *et al.*, 2013; Rippin *et al.*, 2015; Rivera *et al.*, 2008). Ryan *et al.* (2017) used such a payload, in addition to broadband pyrometers, on-board a fixed-wing UAV over a 280 km^2 area of the west GIS in order to gather albedo measurements. This UAV approach was able to achieve 20cm resolution and ±5% accuracies (Ryan *et al.*, 2017). Therefore, using UAVs it became possible to improve upon other past studies analysing albedo fields for energy balance models that used in-situ measurements, numerical modelling and/or satellite imagery (e.g. Fettweis *et al.*, 2013; Gardner and Sharp, 2010; Noël *et al.*, 2015; van As *et al.*, 2012; van den Broeke *et al.*, 2011).

The digital camera used by Ryan *et al.* (2017), however, only permitted albedo measurements within the visible spectrum of light (400-700 nm) to be obtained. Therefore, the variations in albedo that are limited to the near-infrared wavelengths of the spectrum (~ 700 nm – 1 mm), for example those that result from variations in the size of snow grains (Wiscombe and Warren, 1980), were not recorded. Such measurements warrant the use of a multispectral camera that can detect longer and shorter wavelengths of surface reflectance (e.g. MacArthur *et al.*, 2014; von Bueren *et al.*, 2015). However, while UAVs with multispectral cameras on-board have been operated in other fields of study (e.g. Berni *et al.*, 2009), their use is still limited within glaciological studies. Such sensors can often be costly and weigh considerably more than a standard digital camera, therefore, further progress in their development is first needed for them to become both cost-effective for regular use.

Nonetheless, an industry is developing to provide UAVs with small payloads that allow combinations of light detection and ranging (LIDAR), hyperspectral and synthetic-aperture radar (SAR) sensors to be used (Hugenholtz *et al.*, 2012). The CU LIDAR Profilometer and Imaging System (CULPIS) produced by Crocker *et al.* (2012) is one such model. The payload contains LIDAR, command and data handling (C&DH) systems, power regulation, video and static cameras, GPS, as well as an inertial measurement unit (IMU). Collecting elevation data of both land and sea ice surfaces, in addition to imagery, when flown at 200 m above ground level the CULPIS is able to reach a sub-decimetre resolution (Smith, 2007;

Edwards, 2008; Crocker *et al.*, 2009). Short-baseline measurements are also of a similar standard to NASA's Land, Vegetation and Ice Sensor (LVIS), Geoscience Laser Altimeter System (GLAS) and Airborne Topographic Mapper (ATM) (Hofton *et al.*, 2006; Krabill *et al.*, 2002; Zwally *et al.*, 2002b). Due to this high level of accuracy the CUPLIS has consequently been included in a number of glacial Arctic research studies using UAVs. The BAE Systems Manta UAV was one of these, which used CULPIS to map surface features on the GIS in the region next to Jakobshavn Isbræ (Figure 1.1) as part of the National Oceanic and Atmospheric Administration (NOAA) MUSCOX project (Patterson and Brescia, 2008; Patterson and Morris, 2009). CULPIS-X, an improved model, was also used by the US Coast Guard on-board a UAV near Kodiak in the Alaskan Arctic and Beaufort Seas seasonal ice zone, where measurements of sea ice thickness and surface characteristics were acquired (Tschundi, 2013; Tschundi *et al.*, 2016).

2.3 Advent and Use of Structure from Motion Photogrammetry in Glaciological Research

SfM has arisen as a key technique for glaciological research due to its ease of use for use in isolated regions and comparatively low costs (Westoby *et al.*, 2012). The method has subsequently grown to be an important part of our topographic studies in glacial regions, including the mapping of glaciers and ice sheets (Ely *et al.*, 2017; James *et al.*, 2017).

2.3.1 Advent

General photogrammetry concerns the processing of overlapping photographs using control points with known x, y and z coordinates in order to form 3D datasets and structures. The technique's origin can be traced back more than five centuries ago, when scholars began trying to attain a point's coordinate by means of a series of images in relation to the geometry of perspectives (Doyle, 1964). Further advancements were made during the late 19th century, with projective geometry employed on imagery obtained from balloons and kites as well as ground-based surveys and used to map the regional topography (Laussedat, 1899).

Photogrammetry techniques have continued to develop swiftly within the past few decades. Improvements in digital sensors have permitted fast and easy image collection (Eltner *et al.*, 2016), while the capability for 'non-experts' to grasp the method has been enabled through developments in the quality and reductions in the cost of smaller, non-metric single lens reflex (SLR) cameras (Chandler *et al.*, 2005; Fraser and Cronk, 2009; Keutterling and Thomas, 2006; Matthews, 2008; Remondino and Fraser, 2006). Furthermore, progressions

made in soft-copy triangulation and image-based terrain extraction algorithms have considerably enhanced the overall accuracy of terrain data that is collected from overlying stereo-photos (Chandler, 1999; Lane *et al.*, 2000).

SfM photogrammetry first arose in the 1980s and 1990s following the developments in automatic feature-matching algorithms (e.g. Förstner, 1986; Harris and Stephens, 1988) and the computer vision community (e.g. Boufama et al., 1993; Spetsakis and Aloimonos, 1991; Szeliski and Kang, 1994). The advancement of both commercial, particularly Agisoft PhotoScan (Eltner *et al.*, 2016), and open-source software packages (Castillo *et al.*, 2015; Pierrot-Deseiligny and Clery, 2011) has subsequently expanded SfM within the fields of geomorphology and glaciology throughout the last ten years.

The main steps of a typical SfM workflow, as outlined in Figure 2.3, include: pin-pointing homologous points on overlapping stereoscopic photos (e.g. Lowe, 1999); production of a sparse point cloud; georeferencing of the sparse point cloud; and finally increasing the resolution in order to construct a dense point cloud and mesh (Eltner *et al.*, 2016; Smith *et al.*, 2016). The initial photos are commonly additionally mosaicked together to produce an orthophoto and the dense mesh gridded in order to create a DEM.

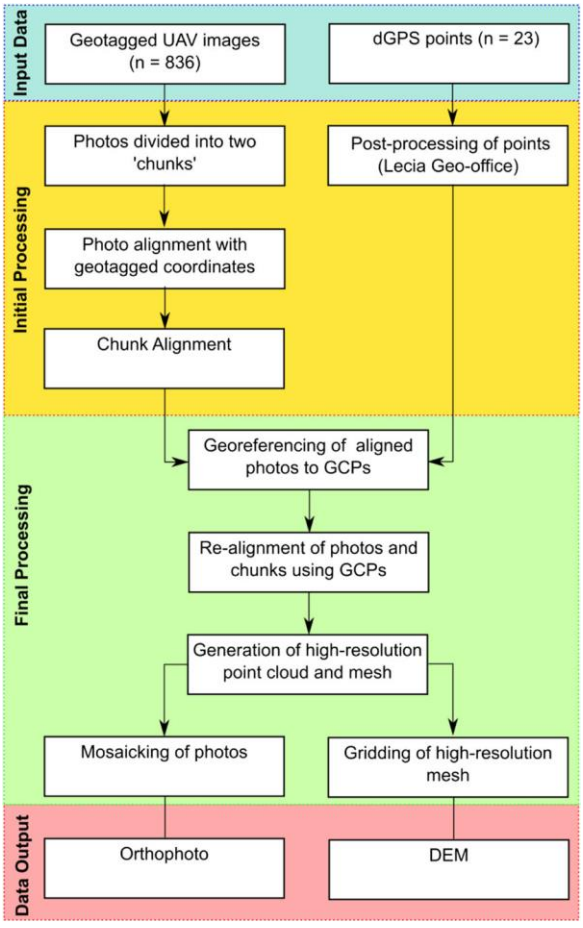

Figure 2.3: *Workflow of the structure from motion photogrammetry process, detailing the input data, initial and final processing stages, plus data outputs. Taken from Ely et al. (2017).*

Comparing traditional stereoscopic photogrammetry and SfM the biggest difference in workflow is that control points are not needed for the latter. Alternatively, SfM software automatically identifies consistently observed landforms as image tie points using a repeated bundle adjustment process and then uses this information to determine the position/orientation of cameras, as well as the study area's geometry (Snavely, 2008; Triggs *et al.*, 2000). Since bundle adjustment requires a large number of tie points, or georeferenced ground control points (GCPs), SfM is therefore best applied to photographs that have a sizeable amount of overlay area (Luhmann

et al., 2014; Kraus, 2007; Mikhail *et al.*, 2001). GCPs are particularly beneficial for SfM studies in order to reduce the possibility of any errors that may otherwise result from poor parameter correlation, for instance non-linear error across a DEM (Eltner and Schneider, 2015; James and Robson, 2014; Wu, 2014). The use of GCPs has been demonstrated to improve the accuracy of DEMs and other outputs significantly specifically in glacial regions (Kääb *et al.*, 2014; Ryan *et al.*, 2015), owing to the high reflectance and lack of certifiable features on glacier surfaces (Gindraux *et al.*, 2017). Thus, an average of six uniformly spread GCPs for every square kilometre of the study area has been suggested previously (Immerzeel *et al.*, 2017). However, the remoteness of some field sites can prevent this being a suitable option and alternative methods of geolocation are required.

2.3.2 Use

SfM has been employed for various glaciological-based studies and with imagery collected from numerous sources. Watson *et al.* (2017) used terrestrial photographs in order to observe ice cliff retreat of Khumbu Glacier, Nepal. Through SfM photogrammetry in Agisoft PhotoScan, in addition to multi-view stereo, they produced nine dense 3D point clouds of the ice cliffs over a twelve-month time frame. This 4D data series permitted analysis of the seasonal and spatial changes in ice cliff retreat, with a mean winter (November – May) retreat rate of 0.030-1.49 cm d^{-1} and summer (May – October) rate of 0.74-5.18 cm d^{-1} calculated (Watson *et al.*, 2017).

Time-lapse photography has also been used in glaciological SfM studies and has the advantage of permitting a recurrent series of 3D topographic data to be analysed at small temporal scales over periods of a season or year (Amundson *et al.*, 2010; Danielson and Sharp, 2013; Murray *et al.*, 2015a; Petilicki *et al.*, 2015). This method was undertaken at an ice-marginal lake on the western GIS by Mallalieu *et al.* (2017) who deployed fifteen cameras to take photographs three times a day over 426 days. This produced a total of approximately 19,000 photographs that were used to create eighteen 3D point clouds of the margin of the ice sheet (Mallalieu *et al.*, 2017). Precise calving events could subsequently be identified and examined from the point clouds, with single calving events seen to range from 234 to 1,475 m^2 / 815 to 8,725 m^3 (Mallalieu *et al.*, 2017). Problems do continue to persist with time-lapse camera orientated SfM research however. As a study goes ahead it becomes increasingly likely that the in-field camera will be disturbed or cease completely. Moreover, studies of finer-scale ice margin dynamics may be hindered by limited ambient

light levels since this can affect both GCP discernibility within photographs and the overall quality of images captured (Katoh *et al.*, 1998).

More recently, researchers using SfM photogrammetry for glaciological projects have increasingly gravitated towards using photographs collected by UAVs: Dall'Astra *et al.* (2015) used such data in the monitoring of rock glaciers; Rippin *et al.* (2015) use a UAV-based method to analyse systems of supraglacial meltwater runoff; and Meunier-Cardinal *et al.* (2016) demonstrate UAV-based SfM photogrammetry has the potential to allow the monitoring of glacier changes on a frequent and on-demand basis. UAV-captured imagery has often been chosen in order to eliminate the 'dead-ground' problem (Wolf *et al.*, 2014), where features and landforms in the foreground of a photograph hide those in the background and subsequently causes significant holes in the SfM data (Westoby *et al.*, 2012).

UAVs also offer the use of close-range photography, which allows SfM to be carried out at considerably smaller spatial scales. Satellite imagery and DEMs do not normally provide a high enough resolution to permit the mapping of smaller glacial landforms such as glacial flutes (Gordon *et al.*, 1992; Hart, 1995; Kjær *et al.*, 2016) and crevasses squeeze ridges (Bennett *et al.*, 1996; Rea and Evans, 2011). Ground-based mapping of such landforms in the field can be arduous and is usually difficult in glacial environments. However, UAV SfM photogrammetry provides a fast and comparatively low cost technique for producing high resolution orthophotos and DEMs that allow for topography mapping even at a sub-decimetre level (Ely *et al.*, 2017; Smith *et al.*, 2016).

For example, Ely *et al.* (2017) create a geomorphological map of the foreland of Sweden's Isfallsglaciären through such UAV SfM photogrammetry in Agisoft PhotoScan. A horizontal resolution of approximately 2 cm was reached for the orthophoto and DEM as a result of this close-range imagery. This allowed small-scale landforms such as glacial flutes to be recorded and their length, width and height to be measured (Ely *et al.*, 2017). Previous research at Isfallsglaciären (Åmark, 1980; Eklund and Hart, 1996; Hoppe and Schytt, 1953) corresponds with the flute measurements recorded by Ely *et al.* (2017), proving the competence of UAV SfM studies.

However, UAV photogrammetry has yet to be used extensively to monitor the development of crevasses and their link to calving events. Ryan *et al.* (2015) were the first to undertake such research, assessing the calving dynamics of Store Glacier through multiple UAV

surveys and SfM assessments. Jouvet *et al.* (2017) employed similar techniques at Bowdoin Glacier, North West Greenland (Figure 1.1), to track the development of a crevasse that instigated a major calving event. Nevertheless, neither study undertook frequent repeated surveys that allowed the monitoring of crevasse propagation and calving at a sub-daily scale. Thus, there is a desire for more detailed data that will capture all stages of the processes leading up to when and after calving occurs.

2.4 Principles of Crevassing

Crevasses are one of the most recurrent surface features on glaciers and ice sheets. Large crevasses have been recognised for several decades, with Meier *et al.* (1957) noting consistently spaced fractures up to 33 m wide in Greenland's Blue Ice Valley. Additionally, Schuster and Rigsby (1954) discerned air-filled crevasses in Palmer Land, Antarctica, with a depth of up to 45 m. But crevasse fractures can also measure to a millimetre-scale where both of the crack's ice faces are in contact, otherwise known as incipient crevasses (Holdsworth, 1969). Monitoring the distribution of crevasses allows a qualitative understanding of ice flow regimes to be obtained, for instance identifying between extensional and compressional or comparatively slow and fast ice flow (Harper *et al.*, 1998; Vornberger and Whillans, 1990).

2.4.1 Formation, Depth Penetration and Closure

In its simplest terms, crevasses form when the strength of the ice can no longer withstand the forces pulling the ice apart. There are, however, three modes of fracture (Figure 2.4):

1) Opening Mode / Mode I – tensile stresses pull the crack plane apart
2) Sliding Mode / Mode II – shear stresses parallel to the crack plane enlarge it in the same direction as that of the shear direction
3) Tearing Mode / Mode III – shear stresses pull the crack plane at right angles to the shear direction

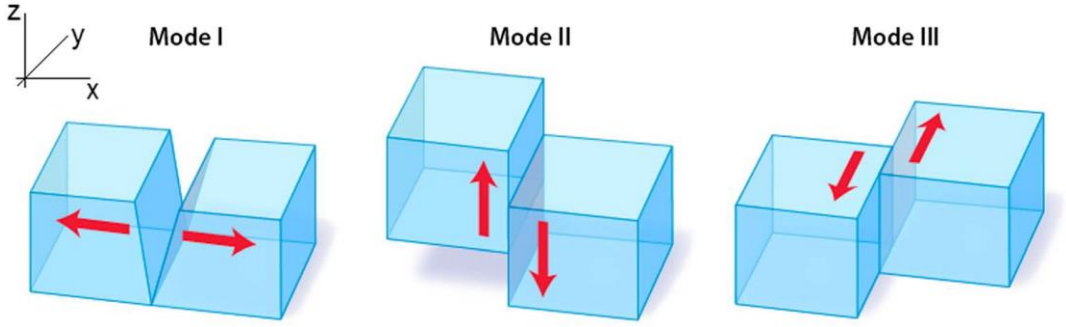

Figure 2.4: *The three modes of fracture: Mode I (Opening), Mode II (Sliding) and Mode III (Tearing). Taken from Colgan et al. (2016).*

It is possible for glacial crevasses to grow through mixed-mode fracture (van der Veen, 1999), that is, as a result of one, two or more of these modes at the same time. However, due to the somewhat small vertical or shear movement of crevasses compared to their large horizontal movement, the formation and fracturing of crevasses is predominantly controlled by the Opening Mode in theory (van der Veen, 1998a, b). Additionally, field observations suggest that the Tearing Mode results in a greater amount of overall displacement than the Sliding Mode, demonstrating the dominance of horizontal shearing over vertical sliding in relation to the fracturing of crevasses (Hambrey, 1976; Meier *et al.*, 1957)

Being able to comprehend the penetration depth of crevasses is continually important and this is often the key aim of crevasse models (Colgan *et al.*, 2016). Although it can be understandably challenging to quantify a narrowing crevasse's depth, in-field measurements are a crucial part of simulating modelled crevasse depths. There is some degree of evidence that crevasses continue to open as a strict wedge as soon as they have opened at the surface, whereby the opening rate of the crevasse reduces linearly with depth, albeit with thermal expansion and contraction causing potential diurnal cycles in the opening rate (Meier, 1958; Meier *et al.*, 1957). This wedge opening is a result of the compressive stresses from the weight of the glacier ice above increasingly offsetting the tensile stretching stresses of the ice motion with increased depth (Figure 2.5a). It is, therefore, possible to determine the depth of a crevasse by calculating the point at which these tensile and compressive stresses are precisely balanced (Nye, 1957). The results of field studies to

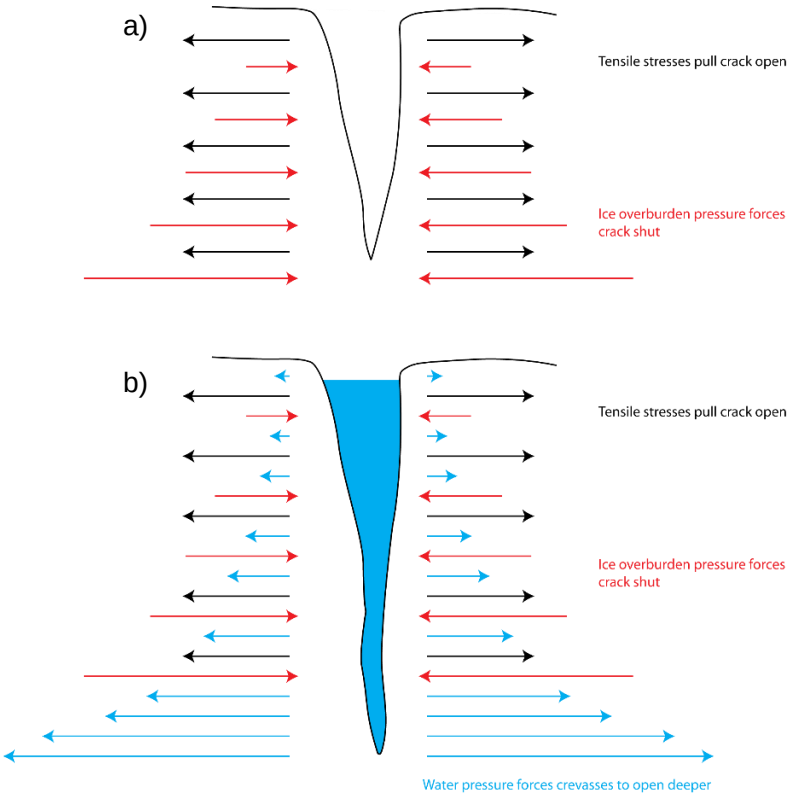

Figure 2.5: *Forces controlling the penetration depth of surface crevasses: a) Crevasses are pulled open by extending flow and closed by compressive stresses as a result of the weight of the ice. These overburden pressures increase with depth, thus placing a threshold on crevasse depth; b) Water in a crevasse creates additional pressures that allows them to propagate deeper into the ice. Adapted from Benn and Evans (2010).*

measure the depths of crevasses on Breiðamerkurjökull, Iceland, by Mottram and Benn (2009) were indeed close to the theoretical depths calculated by this principle.

Due to the swift increase in ice overburden pressures with depth, a maximum theoretical depth of 30 m is often quoted for air-filled crevasses on temperate glaciers (Irvine-Fynn *et al.*, 2011; Seligman, 1955), though in polar regions this can be considerably greater owing to the stiffer and colder ice present (Paterson, 1994). Nonetheless, in-field observations have recorded some crevasses with depths that surpass this theoretic limit by at least 50% (Cook, 1956; Hambrey, 1976; Holdsworth, 1969; Schuster and Rigsby, 1954; Mottram and Benn, 2009).

However, the depth of a crevasse can be notably different if the fracture is infilled by surface meltwater. The resulting water pressure resists the ice overburden pressure and attempts to continue to pull the crevasse apart (Figure 2.5b). This can result in hydrofracturing if the meltwater fills up about 92% of the crevasse's depth (Weeertman, 1973), allowing the fracture to propagate downward. This can continue if the crevasse is recurrently filled with new meltwater, eventually leading to expansion throughout the full thickness of the glacier. Such is the case for moulins, which can often develop at the location where supraglacial meltwater initially flowed into a surface crevasse, leading to a link between a glacier's supraglacial and subglacial hydrologic networks (Hooke, 1989; Irvine-Fynn *et al.*, 2011).

Eventually, the sharp edges of the crevasse at the glacier's surface start to fray away over time through the spalling of fragments and surface ablation (Cathles *et al.*, 2011). As the glacier continues to move forward the crevasse can ultimately close through the active compressional forces of the ice, or due to the infilling of snow and frozen meltwater, or additionally as a result of differential surface ablation (Harper *et al.*, 1998; Meier, 1960). Finally, once a crevasse is closed after the two ice faces are restored together it leaves behind a linear scar referred to as a crevasse trace (Hambrey, 1975, 1994; Hambrey and Lawson, 2000).

2.4.2 Orientation and Relationship to Strain Axis

The orientation of crevasses can be an important measure of the dynamics of a glacier and a display of how forces within the ice are acting. As a straightforward theory, crevasse orientation is controlled by the three strain rate components $\dot{\varepsilon}_{xx}$, $\dot{\varepsilon}_{yy}$ and $\dot{\varepsilon}_{xy}$ (Nye, 1952; van der Venn, 1999a). These can be calculated using the surface velocity components U_s and V_s and their parallel x and y directions as outlined by Benn (2007) as follows:

$$\dot{\varepsilon}xx = \frac{\partial Us}{\partial x} \quad (1)$$

$$\dot{\varepsilon}yy = \frac{\partial Vs}{\partial y} \quad (2)$$

$$\dot{\varepsilon}xy = \frac{1}{2}\left(\frac{\partial Vs}{\partial x} + \frac{\partial Us}{\partial y}\right) \quad (3)$$

The angle at which the chief extensional axis of strain is orientated, θ, can subsequently be calculated using:

$$tan2\theta = \frac{2\dot{\varepsilon}xy}{(\dot{\varepsilon}xx - \dot{\varepsilon}yy)} \quad (4)$$

These strain rates can result in two types of shear: pure and simple. If pure shear is the only component of ice deformation (Eqs. (1) and (2)), then crevasses are expected to form perpendicular to the principal direction of strain. On the other hand, crevasses will be angled 45° relative to the shear axis if simple shear is the dominant factor leading to the deformation of glacier ice (Eq (3)). Varying mixtures of pure and simple shear will result in crevasses with orientations that lie in between this range (Benn, 2007; Nye, 1952). Although in some instances crevasses can correlate well to this theoretical relationship (Harper *et al.*, 1998), ever since early field studies were undertaken it has been seen that fractures very rarely completely correspond with the axes of strain (Kehle, 1964; Whillans *et al.*, 1993).

Difficulty in determining the relationship between strain axis and crevasse orientation can occur however. For instance, if multiple mode fracture occurs then one mode of crevasse may be superimposed over another (van der Veen, 1999, 2013). Furthermore, crevasses that develop in the upper areas of a glacier may be rotated as they move down the glacier. This can often be seen at calving fronts, where the crevasses resulting in calving events can either be those forming at the front itself as a result of localised stress patterns, or those that have travelled from other regions (Benn, 2007).

2.4.3 Types and Patterns

Figure 2.6 shows the principal types of crevasses observed on glaciers. As a straightforward theory, crevasses form at right angles to the direction of the main tensile stress (Nye, 1952; Paterson, 1994). Transverse crevasses are typical of this, forming perpendicular under the extensional stress of the forward glacier flow through slip faults (Figure 2.7a) (Glen, 1955). Such crevasses may stretch across glaciers for large distances if the stress regime is

uninterrupted. However, where lateral drag at the valley margin occurs the primary tensile stress gradually pivots and results in crevasses that begin to concave down-flow. Compressive flow on the other hand produces thrust faults and splaying crevasses (Figure 2.7b) (Glen, 1955; Nye, 1952). The resulting fractures are roughly parallel to the glacier's flow direction, but curve at angles under 45° to meet the margins.

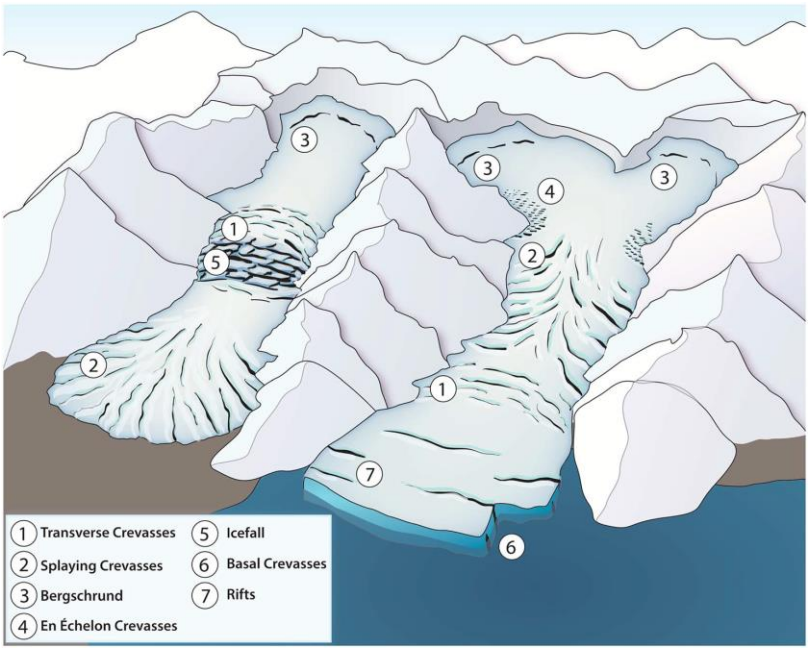

Figure 2.6: *The various types of crevasses found on glaciers. Taken from Colgan et al (2016).*

Although the varying styles of surface crevasses are more often widely observed and measured, basal crevasses, fractures that propagate from the bottom of an ice sheet or glacier upwards, can also play an important role in the dynamics of marine-terminating glaciers. Basal crevasses can occur when the substantial compressive stresses at the bottom of an ice mass are overpowered by both very large basal water pressures and tensile stresses (van der Veen, 1998b). Therefore, basal crevasses usually only develop under glacial ice that is both floating and rapidly extending (Bassis & Walker, 2012; Ma *et al.*, 2017).

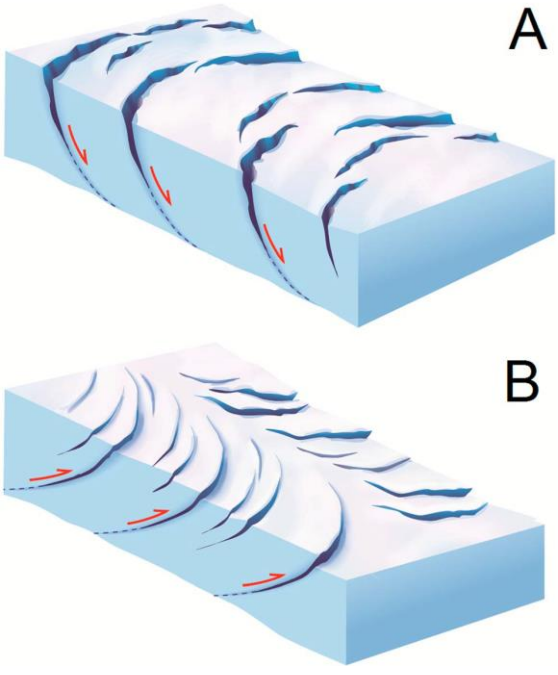

Figure 2.7: *Graphic portraying: a) transverse crevasses resulting from extensional flow and slip-faulting; b) splaying crevasses formed through compressive flow and thrust-faulting. Taken from Colgan et al (2016).*

Todd *et al.* (2018) have previously modelled the penetration depth of surface and basal crevasses across the snout of Store Glacier. Surface crevasses are shown to be prevalent across the majority of the snout with deeper crevasses towards the front of the terminus (Figure 2.8a), deemed to be as a consequence of the ice cliff force imbalance that intensifies extensional stresses at the glacier's surface (Hanson and

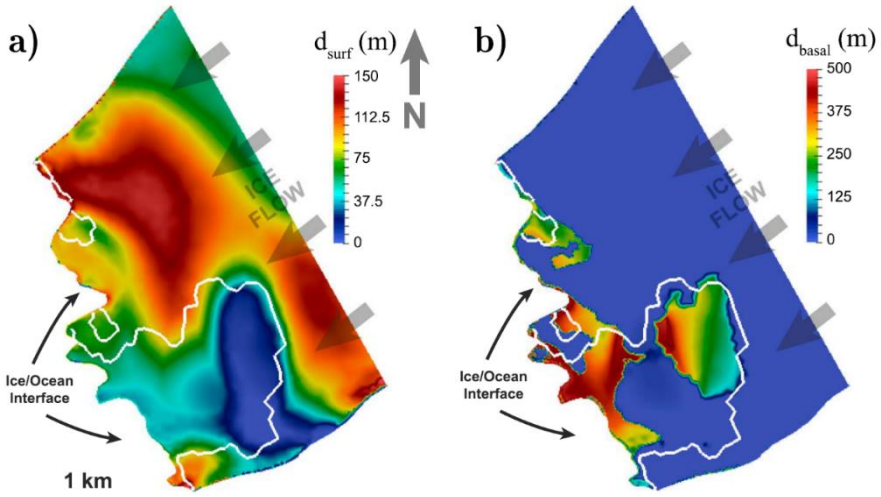

Figure 2.8: *Models of a) depth of surface crevasses, and b) height of basal crevasses, across the snout of Store Glacier. The white line represents the glacier's grounding line; note the different colour scales. Taken from Todd et al (2018).*

Hooke, 2003; Todd *et al.*, 2018). Nonetheless, while crevasses are widespread across the glacier, those in the north are modelled to be substantially deeper than those in the south, by up to 150 m (Figure 2.8a).

Basal crevasses, however, are simulated to be far more confined in their location, as observed in Figure 2.8b. Since basal crevasses can only form underneath floating ice this predominantly restricts their development to the southern side of the terminus where the overdeepening is located and the grounding line is situated 30 km inland of the calving front (Figure 2.8b). The resulting basal crevasses are estimated to be up to 500 m in height (Todd *et al.*, 2018). Such crevasse depth simulations, as well as other research through remote sensing techniques, insinuate that topography/bathymetry and the geometry of a glacier can be significant factors in determining the pattern of crevasses across a body of ice (Carr *et al.*, 2013; Krug *et al.*, 2014; Moon *et al.*, 2015; Ultee and Bassis, 2016).

2.5 Principles of Calving

Dynamic ice loss from calving outlet glaciers is a key contributor to the GIS's mass balance, with 546 ± 11 Gt yr^{-1} being lost in 2012, an increase of 18% from 2000 (Enderlin *et al.*, 2014). All calving events transpire when crevasses, either surface and/or basal, propagate through the entire thickness of a glacier due to strong tensile stresses at the snout. However, the mechanisms that lead to the expansion of these crevasses, plus the location and timing of individual calving events, are less well understood (O'Neel *et al.*, 2003; Warren *et al.*, 1995). Nevertheless, investigations into the calving of Greenlandic glaciers have predominantly

concentrated on two mechanisms: buoyancy-driven calving, and calving as a result of ice front submarine melting (Benn *et al.*, 2017a).

Buoyancy-driven calving results in some of the globe's most dramatic calving events, with the released tabular icebergs often hundreds of metres long and wide (James *et al.*, 2014; Medrzycka *et al.*, 2016; Warren *et al.*, 2001; Xie *et al.*, 2016). The fast flow of large glaciers into deep water can generate a super-buoyant environment where the ice front is not at hydrostatic equilibrium and thus exposed to net upward torque forces (Figure 2.9; Benn *et al.*, 2017a, b). As the glacier snout becomes progressively further away from equilibrium, bending forces close to the connection with grounded ice cause the front to elevate and rotate (James *et al.*, 2014; Murray *et al.*, 2015b). This movement permits basal crevasses to penetrate upwards (O'Neel *et al.*, 2003; Scambos *et al.*, 2008; Wagner *et al.*, 2016) and increase the propagation depth of surface fractures in high strain environments where crevasses are partly filled with meltwater (O'Neel et al., 2003; van der Veen, 1998a). Following the propagation of crevasses through the glacier, calving and overturning of the calved ice block occurs. This important role of basal crevasses in the calving of buoyant glaciers has been demonstrated in Greenland at Helheim Glacier (James *et al.*, 2014; Murray *et al.*, 2015b) and validates the idea that both basal and surface crevasses must be accurately modelled in order to satisfactorily parameterise iceberg calving (Colgan *et al.*, 2016).

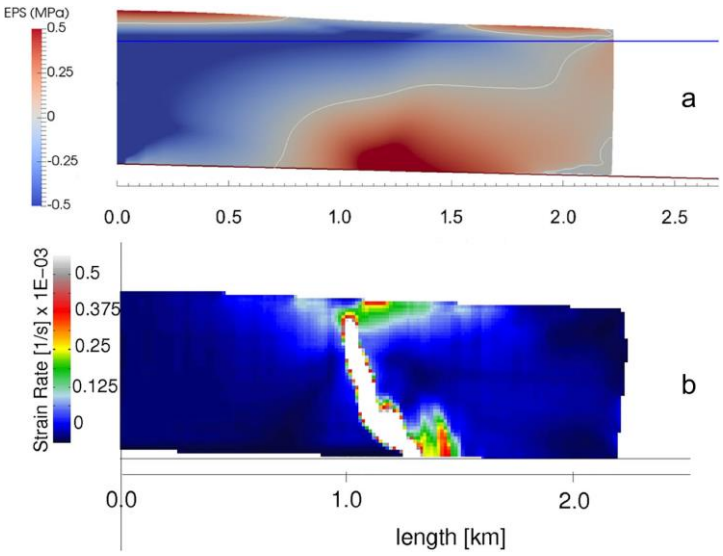

Figure 2.9: *Model of buoyancy-driven calving: a) A stress field across a superbuoyant ice tongue, EPS = effective principal stress; b) Average strain rates in inter-particle bonds with white areas representing broken bonds. This demonstrates thin fracture grow upwards from the centres of concentrated tensile stresses at the base of ice. Taken from Benn et al (2017a).*

Calving ensuing from subaqueous melting, meanwhile, has grown as a topic of discussion following the identification of warm Atlantic waters making its way into the deep fjord systems of Greenland (Bendtsen *et al.*, 2015; Christoffersen *et al.*, 2011; Straneo *et al.*, 2012, 2013). Submarine melting can gradually undercut a grounded calving front or destabilise a floating terminus (Luckman *et al.*, 2015; Münchow *et al.*, 2014; O'Leary and Christoffersen, 2013;

Truffer and Motyka, 2016), intensifying the force imbalances already present at the ice cliff. As these forces continue to increase, crevasses have an easier time to propagate through the glacier, particularly since there is less ice to break through. Eventually calving can occur through the collapse of the undercut ice in addition to the failure of ice along arcuate fractures in the roof of the melt notches (Benn *et al.*, 2001; Haresign and Warren, 2005; Iken, 1977; Warren and Kirkbride, 2003). Additionally, if subaqueous melting occurs at the bottom of the ice cliff, Xie *et al.* (2016) propose that this can subsequently lead to buoyancy-driven calving as the ice block is not gravitationally stable anymore, rotates and allows a basal crevasse to develop, leading to calving (Figure 2.10).

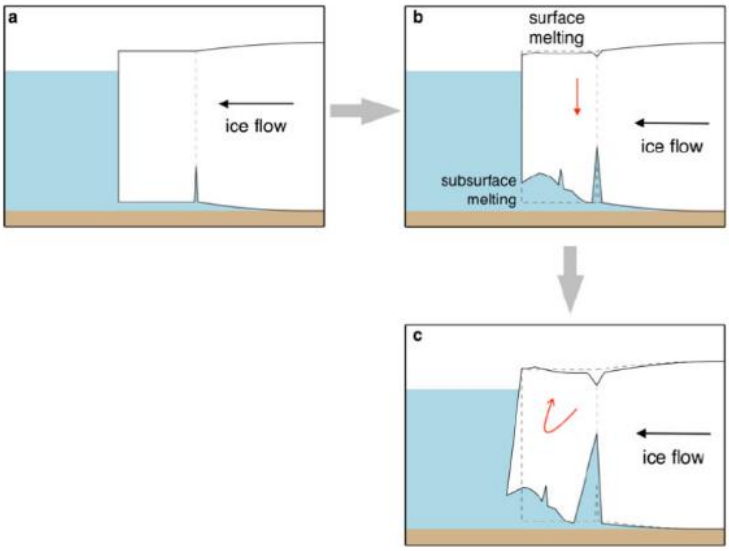

Figure 2.10: *Schematic of subaqueous-melting-induced calving: a) stable ice front; b) subaqueous melting outweighs melting at the surface this the ice becomes gravitationally unstable; c) rotation and upward torque forces allows the basal crevasse to propagate upwards and the ice ultimately calves. Taken from Xie et al. (2016).*

Studies have estimated that the average submarine melt rate of a glacier terminus is between approximately 1 and 10 m day^{-1} (Chauché, 2016; Inall *et al.*, 2014; Rignot *et al.*, 2010; Sutherland and Straneo, 2012), with the range of values a result of the regional variations of subglacial discharge and heat content in the oceans (Jackson and Straneo, 2016). It had previously been thought that this rate of submarine melting would be low in all regions (Russel-Head, 1980), as free convection, where water movement is directed merely by temperature differences in the water column, is a comparatively slow process. In spite of this however, the upwelling of meltwater from a glacier's bed in plumes can result in forced convection, which powers a far greater flux of energy and melt rate, even attaining values analogous to the total amount of ice lost by a glacier through calving (Haresign and Warren, 2005; Motyka *et al.*, 2003).

Such meltwater plumes were observed at Store Glacier by Chauché *et al.* (2014), where they were seen to be producing embayments in the calving front (c.f. Figure 2.11). Naturally, the enlargement of these embayments lessens the lateral buttressing of the adjacent

peninsulas, causing calving to occur due to the loss of stability in the ice (Benn *et al.*, 2017). Meltwater plumes were additionally a key control factor in the model of Store Glacier produced by Todd *et al.* (2018). Despite the confined nature of the melting attributed to meltwater plumes, their reduction of lateral support means they can prompt calving along a wide section of a glacial terminus, increasing their influence on the amount of ice a glacier loses. This means that calving is potentially influenced by the distribution of subaqueous melting more so than the overall volume of meltwater (Todd *et al.*, 2018). Thus, topography/bathymetry and glacial hydrology (the factors that regulate the position of meltwater plumes) again emerge as principal influencers of glacier stability and calving.

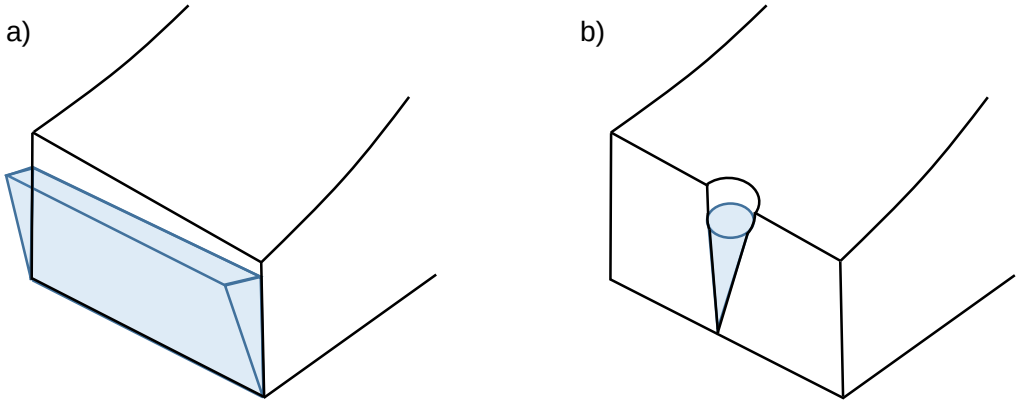

Figure 2.11: *One dimensional model representation of: a) free convection and its impact across the entire front; b) meltwater plume flow and subsequent melting of the ice front and creation of an embayment. Adapted from Chauché et al. (2014).*

3. METHODOLOGY

3.1 Structure from Motion

Members of the RESPONDER (Resolving subglacial properties, hydrological networks and dynamic evolution of ice flow on the Greenland Ice Sheet) project obtained imagery of Store Glacier's calving front using a Skywalker X8 2m wide fixed-wing UAV over a period of five days between 10th and 14th July 2017 (Chudley *et al.*, 2018). Table 3.1 details the timings of each of the ten surveys undertaken within the study period, while an example flight path of the 11_2 survey and the amount of overlap between images are shown in Figure 3.1. The location of photographs taken on the 11_2 sortie and their error estimates are additionally displayed in Figure 3.2.

Table 3.1: *Flight times of the ten UAV surveys undertaken by the RESPONDER team across the calving front of Store Glacier.*

Day	Survey No.	First Image (Local Time)	Last Image (Local Time)	Hours Since Last Survey
10/07/2017	10_1	12:22	12:44	-
	10_2	18:36	18:54	6.2
11/07/2017	11_1	10:10	10:30	15.6
	11_2	16:41	17:00	6.5
	11_3	21:57	22:16	5.3
12/07/2017	12_1	09:54	10:21	12.0
	12_2	16:05	16:31	6.2
	12_3	22:07	22:27	6.0
13/07/2017	13_1	10:01	10:30	12.0
14/07/2017	14_1	21:47	22:18	35.8

The Skywalker X8 has previously been successively employed by Jouvet *et al.* (2017) and a similar payload was used by the RESPONDER team here, containing a Sony Alpha 6000 on-board camera (16 mm lens and 24 megapixels) and Pixhawk open-source autopilot operating a APM ArduPlane software. In addition, a carrier phase GPS was also installed to use as the chief way to geolocate the photographs taken instead of GCPs due to the lack of natural tie points available across the glacier snout and the inaccessibility to lay down additional points in the field. This alternative, termed GNSS-supported triangulation, was tested by Benassi *et al.* (2017) who demonstrated that it provided a root-mean-square-error of 2-3 cm compared to use of GCPs. Although this accuracy is not absolute, applying only for a specific altitude, GNSS-supported triangulation was deemed to be an accessible and accurate determiner of GPS position, plus a suitable alternative to the use of GCPs in this field location.

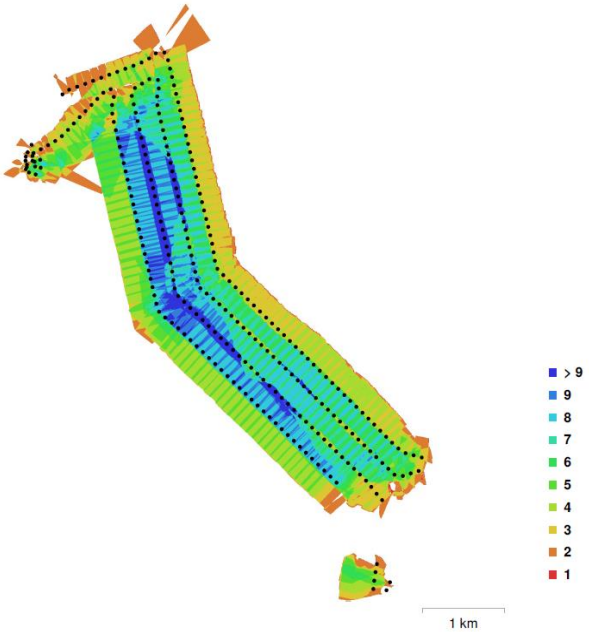

Figure 3.1: *Flight path of the 11_2 UAV survey (black dots) and overlap of the photographs taken (colour scale).*

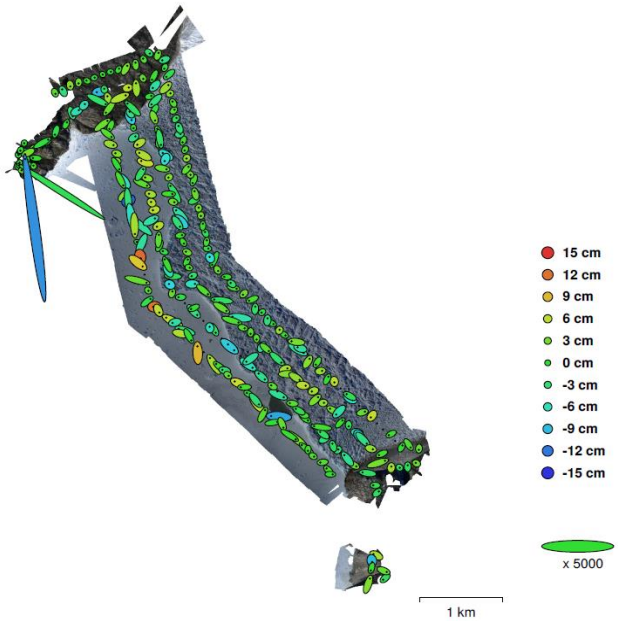

Figure 3.2: *Camera locations of the images taken during the 11_2 UAV survey and error estimates for each of the images. Z error is represented by ellipse colour; X,Y errors are represented by ellipse shape.*

The SfM photogrammetry software Agisoft PhotoScan 1.3.3 was subsequently used to process the obtained imagery, with Figure 3.3 detailing the various stages and chosen settings at every stage of the procedure. First of all, to eliminate the orientation data incorporated within them, the images were transformed into a .tif format, before they were inputted into PhotoScan as a 'chunk' (Figure 3.3a). The images had, on average, errors of between 10 and 12 cm, and this was considered to be suitable for analysis to take place. A GPS offset of x = 0 m, y = -0.795 m, z = 0.1322 m was also recorded in order to account for the disparity in location of the UAV's camera and GPS antenna (Figure 3.3b).

A batch process was consequently designed to create the desired DEMs and orthomosaics, and the photos from each of the ten surveys were put through it. This batch process first involved photo alignment (Figure 3.3), with a tie point limit and key point limit of 40,000 and 4,000 chosen respectively. In order that the estimates of camera/photo location were as precise as possible, the highest accuracy setting was also selected. When inputting UAV photography into SfM software it is frequently beneficial to authorise the 'Constrain features by mask' setting due to the tilting of the on-board camera when a UAV goes around corners in an attempt to prevent the wide, inaccurate point cloud that this can result in. However, this was not selected here as no long ranging images were obtained since the ice front of Store Glacier is constrained within valley walls (Figure 1.1). A sparse point cloud was subsequently constructed after this alignment was optimised (Figure 3.3d).

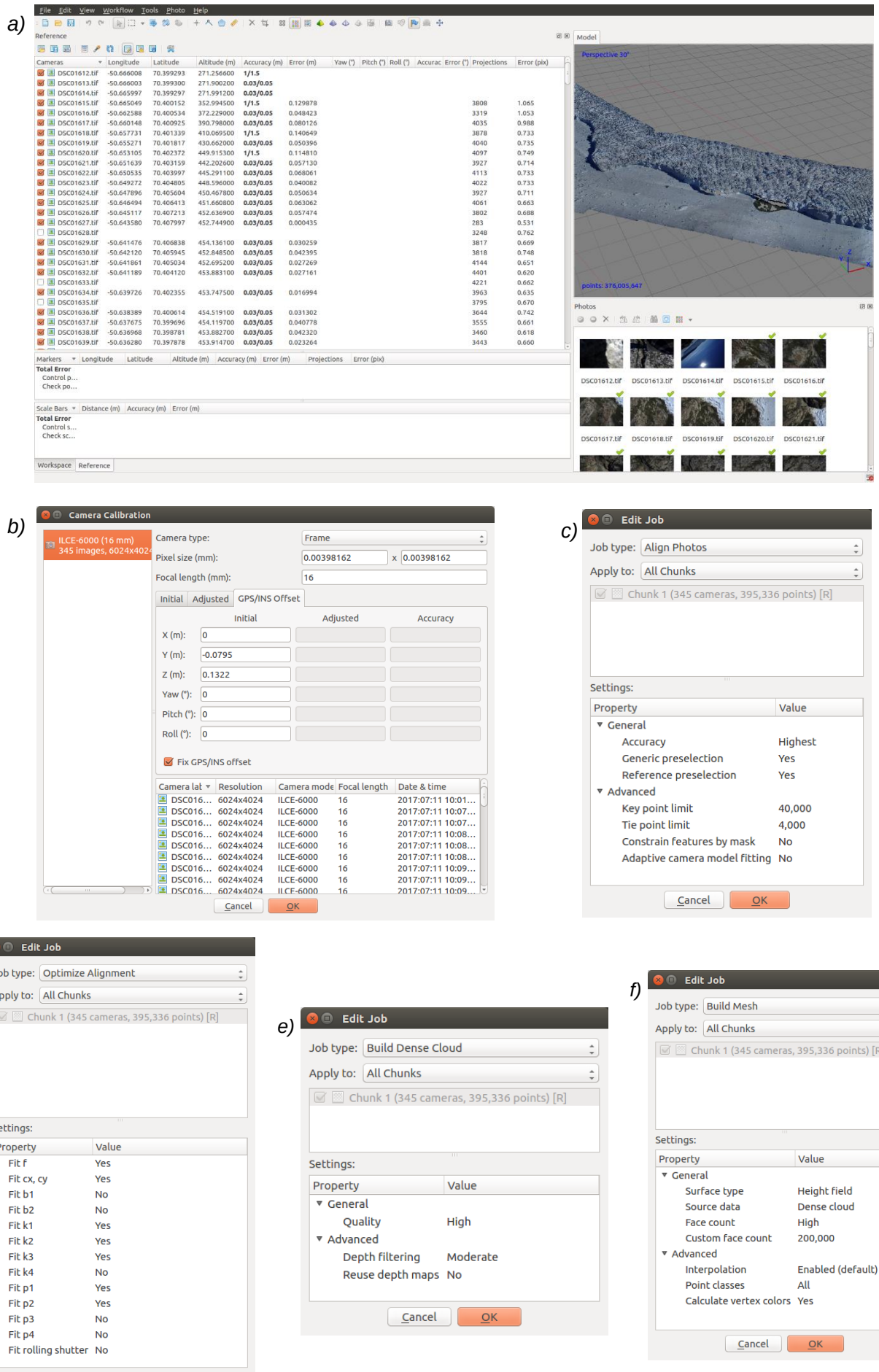

Figure 3.3: *continued on next page*

g)

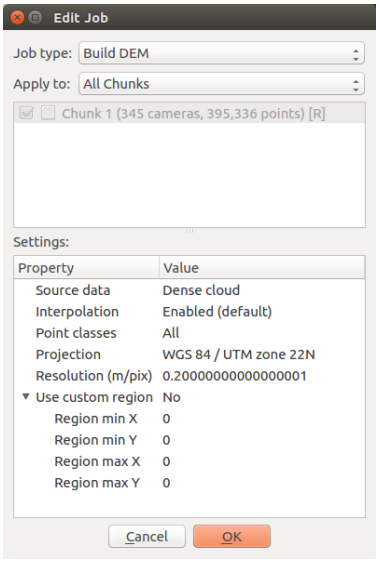

h)

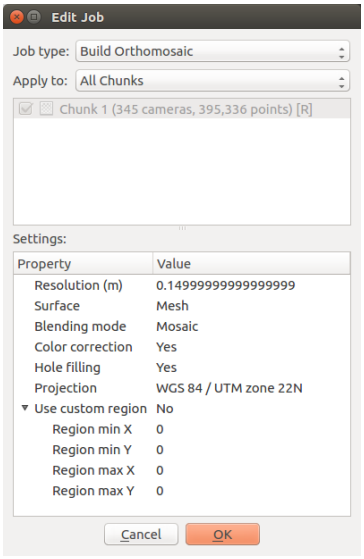

Figure 3.3: *Screenshots of the settings selected during the steps undertaken in Agisoft PhotoScan for structure from motion photogrammetry: a) add photos; b) GPS offset; c) align photos; d) optimise alignment; e) build dense cloud; f) build mesh; g) build DEM; h) build orthomosaic.*

The batch process was then set up to use this preliminary sparse point cloud in order to produce a dense cloud (Figure 3.3e), an example of which for the 11_2 survey is shown in Figure 3.4. Moderate (instead of aggressive) depth filtering was chosen so that PhotoScan did not 'flatten out' the point cloud by eliminating any smaller details as outliers. Additionally, the quality of the dense cloud was fixed at high (rather than ultra-high) owing to the available computer memory space. An initial model could then be obtained from the dense point cloud by converting it into a mesh (Figure 3.3f). 'Height field' was chosen for the mesh production because it requires less memory space, therefore permits bigger datasets of aerial images to effortlessly be processed, and is also optimised for planar surfaces like topography and terrains.

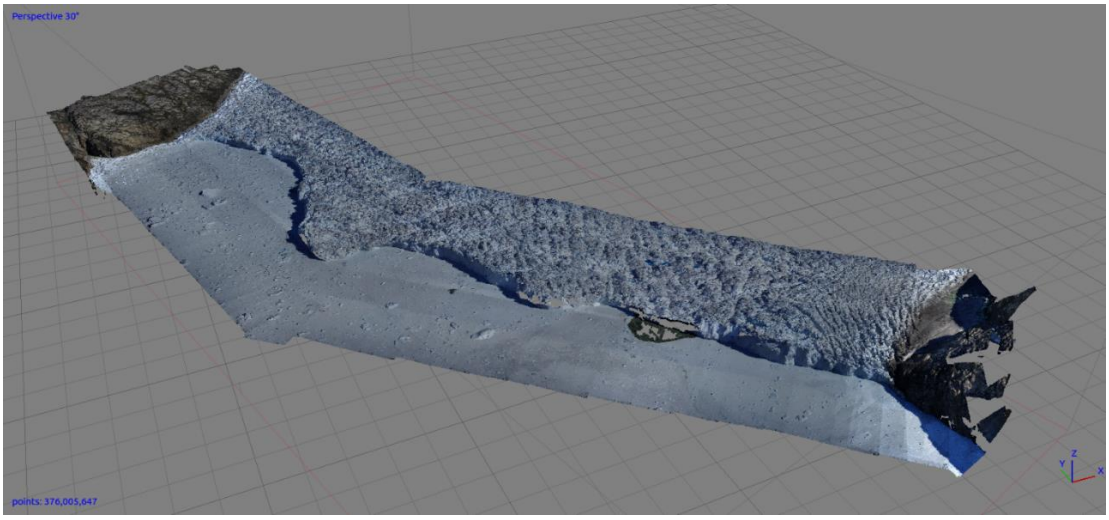

Figure 3.4: *Dense point cloud of Store Glacier snout during the 11_2 survey, as viewed in Agisoft PhotoScan.*

The final DEM and orthomosaic were then successively created from the dense point cloud and mesh respectively (Figures 3.3g, h and 3.5). A resolution of 15 cm was set for the orthomosaic, with hole filling and colour correction also employed. Meanwhile, the resolution of the DEM was set to 20 cm and then projected over UTM 22N, the coordinate zone of Store Glacier. This resolution of 20 cm delivers topographical data with far finer detail compared to previous data of this region. The ArcticDEM, a public-private programme generating an entire Arctic-wide DEM from satellite imagery, presently has a 2-5 m resolution (Showstack, 2017). Additionally, while Ryan *et al.* (2015) previously used SfM to analyse the snout of Store Glacier, the DEM produced only obtained a resolution of 38-40 cm; a choice taken due to the time needed to process such a high resolution output. The resulting DEMs were finally geoid corrected in ArcMap 10.5.1 using the EGM2008 geoid model and clipped in order to only cover the glacier's extent. Hillshades of the glacier from each survey were additionally created from the DEMs.

3.2 Crevasse Mapping

From the generated DEM and orthomosaic for each survey the crevasse patterns of the caving front were subsequently mapped in ArcMap. Due to the laborious effort required to map all crevasses by hand, a simple automatic method was sought after.

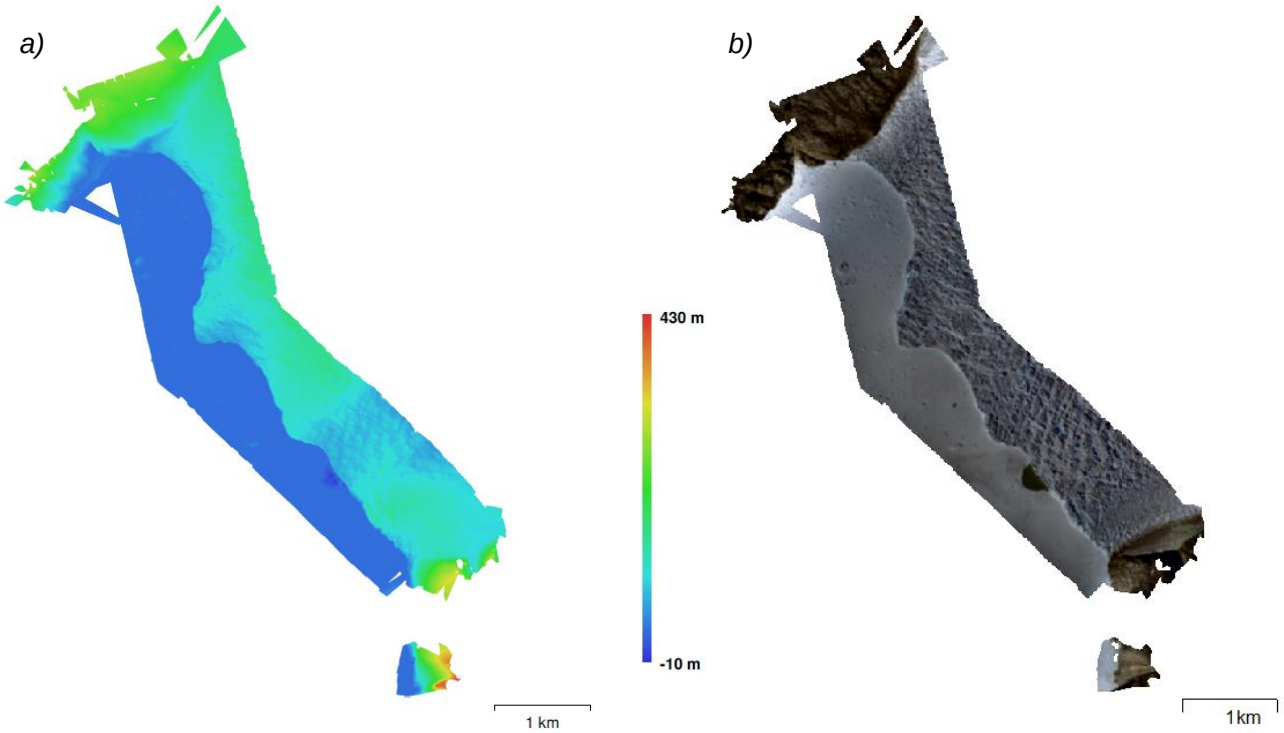

Figure 3.5: *Examples of the a) digital elevation model, and b) orthomosaic, produced of Store Glacier's calving front for the 11_2 survey.*

3.2.1 Method Selection

Two main mapping methods were tested: Gaussian blurring of the DEMs and object-based image analysis (OBIA) of the orthomosaics/hillshades. Since surface crevasses are essentially topographic features, with a height/depth axis, it should be possible to identify/map such features using a DEM. During their research of Store Glacier's snout, Ryan *et al.* (2015) did just this, undertaking a Gaussian filter at 200 pixels (100 m) to produce negative surface anomalies that were then used to map crevasses at the calving front. The same method was initially tested here, however, due to the higher resolution of the DEMs obtained in this study the blurring at 200 pixels was equivalent to 40 m. The blurred DEMs were then subtracted from the originals in order to obtain the negative surface anomalies, which were consequently reclassified and converted into polygon shapefiles of the glacier's crevasses. This process was repeated for blurs at 100 pixels (20 m) and 400 pixels (80 m) in order to compare and determine the best level at which to map the crevasses.

The 200-pixel blur allowed crevasses of a 5 m amplitude to be mapped (Figure 3.6b), encompassing all first order crevasses. However, the blurring at 400 pixels merged a few crevasses together (Figure 3.6c) and was therefore not deemed as the suitable level at which to accurately map the crevasses. The 100-pixel blurring was also tested and was able to pick up smaller crevasses at a 2 m amplitude (Figure 3.6a). But, due to the relatively little difference between the 100 and 200-pixel blur, yet the increased computing time required, it was decided that the blurring would be done at 200 pixels. This research focuses on the development of large crevasses over time that could potentially lead to a calving event, and the 200-pixel blurring was deemed appropriate to monitor this without the need of mapping smaller second order crevasses that would not influence this.

As well as topographic, surfaces crevasses are also visible features and should be able to be mapped through aerial imagery, thus OBIA was also tested out. Initially, the orthomosaics were run through a supervised and unsupervised classification process in ArcMap. While this was able to pick out even relatively small crevasses, there was difficulty in distinguishing those in areas of the glacier that were more debris covered, and the process additionally often picked out entire surface meltwater ponds as crevasses (Figure 3.7). In order to improve the outcome, tests were run using OBIA on combinations of the orthomosaics, DEMs and developed hillshades in a similar manner to Kraaijenbrink *et al.* (2016), who used a both the RGB bands of an orthomosaic as well as elevation and slope data from a DEM in order to map and characterise surface features on a debris-covered glacier. It was

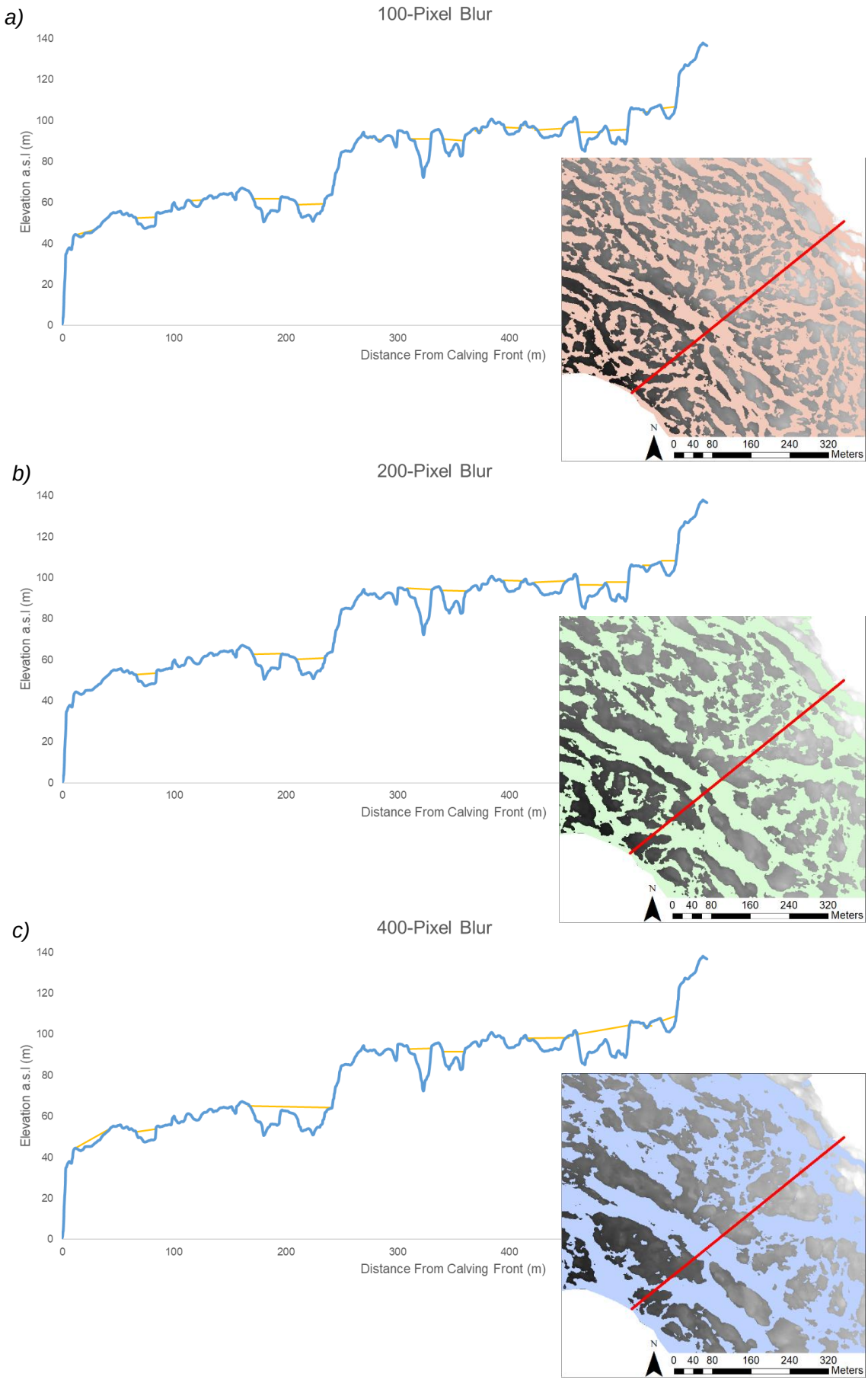

Figure 3.6: *Depth profiles across a selected extract of the 10_1 DEM showing the crevasses picked up through the different scale blurring techniques, with insets showing the chosen transect (red line) and mapping extent at each scale: a) 100 pixels; b) 200 pixels; c) 400 pixels.*

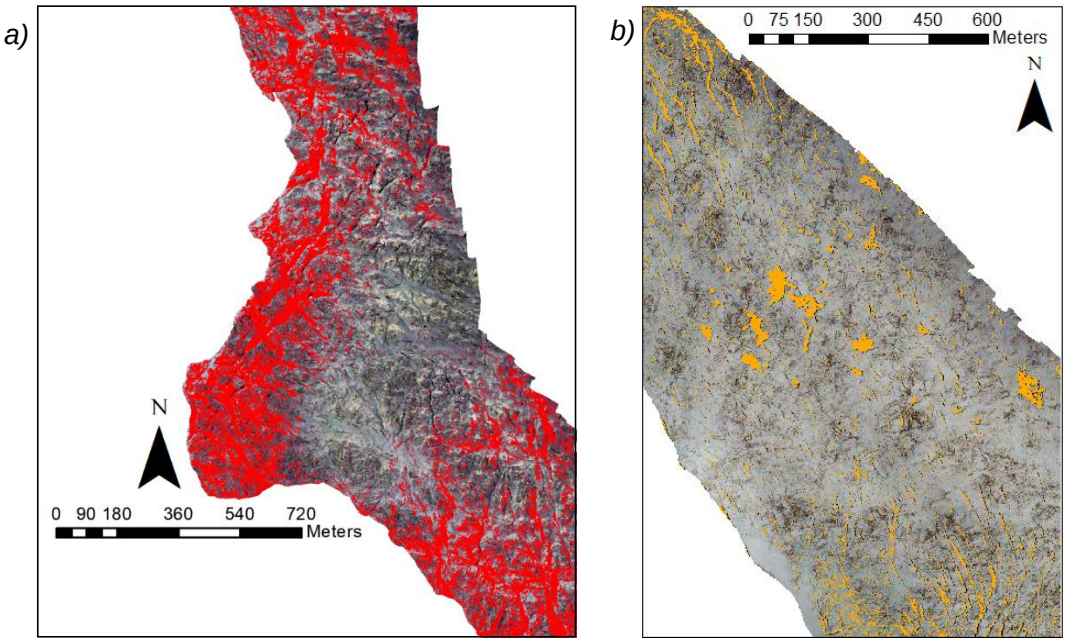

Figure 3.7: *Object-based image analysis tests using the orthomosaics depicting a) a problem picking out crevasses in debris-covered areas, and b) the representation of large meltwater ponds as crevasses.*

determined that the hillshade provided the best outcome, with a much clearer pattern of crevasses being mapped than compared to using the orthomosaic alone.

In determining whether the Gaussian blurring or OBIA was the most suitable method for mapping the crevasses the two results were compared (Figure 3.8). Both methods had the disadvantage that the crevasses were predominantly amalgamated into one large shapefile,

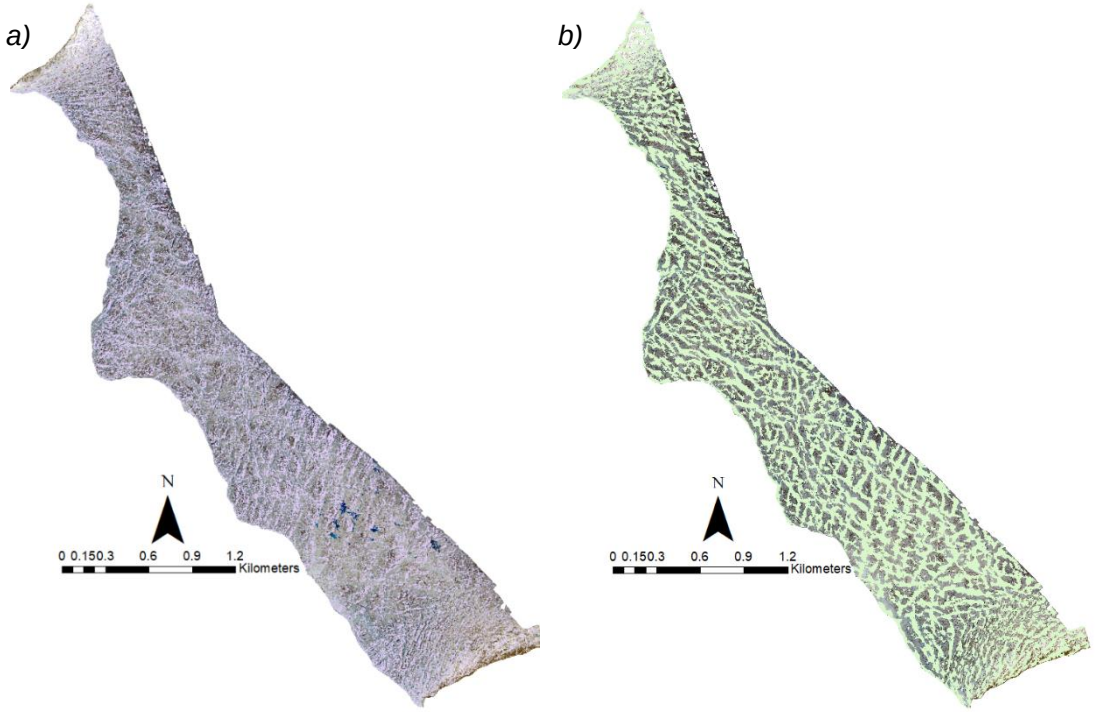

Figure 3.8: *Examples of the crevasse maps of the 10_1 survey produced through; a) object-based image analysis, and b) Gaussian blurring.*

therefore making it hard to systematically calculate the characteristics of each individual crevasse in an automated way. In the end it was decided that the Gaussian blurring method provided a clearer representation of Store Glacier's crevasses, with more visible progression between surveys that allows the changes in crevasses over time to be better documented. Although OBIA may pick up on more individual and smaller crevasses, as stated previously the emphasis of this study is on how the expansion of large crevasses and their possible influences on specific calving events. Therefore, the higher detail of the OBIA mapping does not in fact aid the answering of the outlined aim of this project, while the Gaussian method offers an easier means by which to do this. Thus, the research moved forward with use of the Gaussian blurring mapping.

3.2.2 Measurement of Crevasse Characteristics

Once a map of crevasses had been created for each of the ten surveys the changes over the five-day study period were noted. The different types of crevasses observed across the calving front were also recorded and this was used to split the snout up into different analysis regions. Five regions were chosen, similarly to Ryan *et al.* (2015): region A and E represent the north and south side of the snout respectively, C the central area, plus B and D more transitionary areas on the north and south side respectively (Figure 3.9).

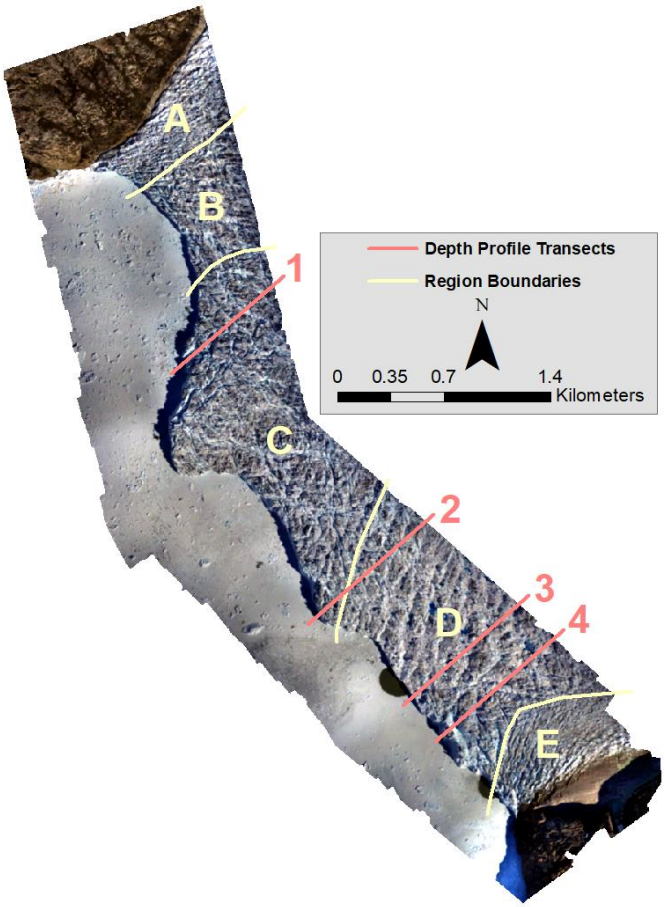

Figure 3.9: *The five regions used to split up the snout of Store Glacier (A-E) and four transects used to obtain the depth profile information (1-4).*

The length, width, depth and orientation of crevasses within each of these five regions were subsequently recorded. Due to the labour intensive nature and amount of time required to measure each individual crevasse by hand a sampling method was put in place using a fixed and moving transect (Figure 3.10). Crevasses were additionally only measured from the first (10_1) and last (14_1) surveys; this was because Store Glacier advanced at approximately 16.7 m d^{-1} throughout the

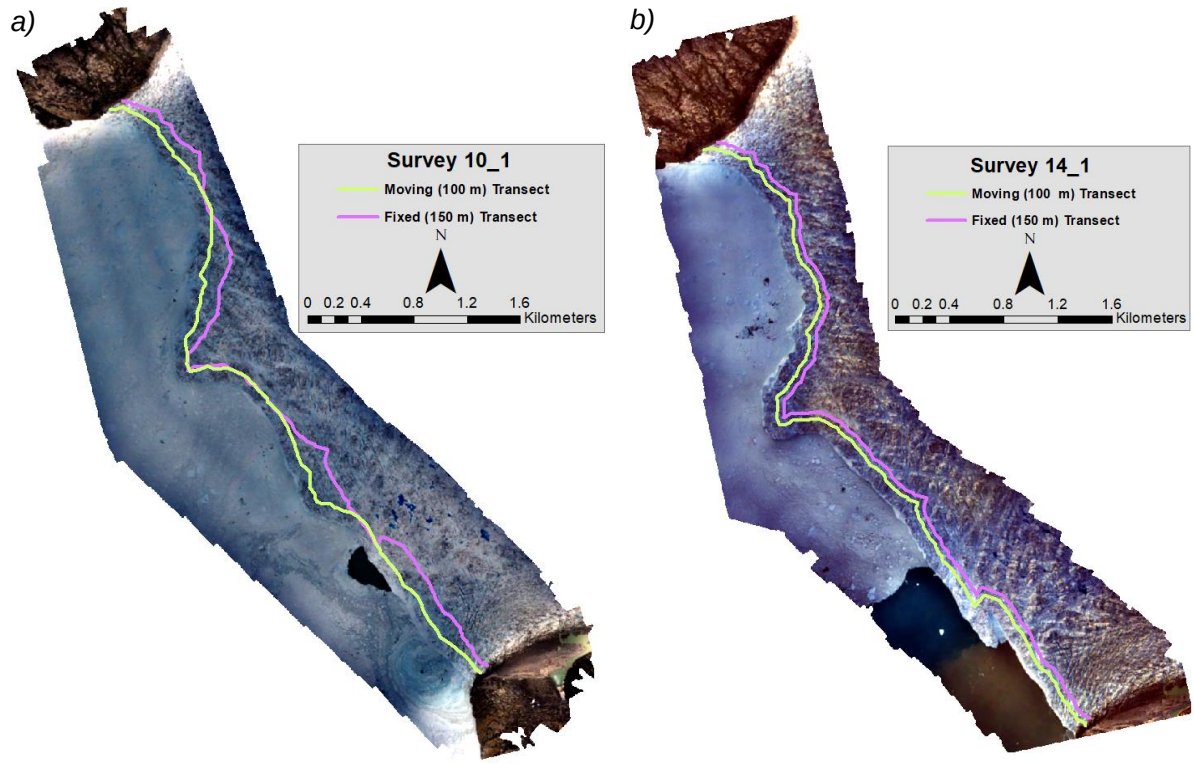

Figure 3.10: *Orthomosaics of survey a) 10_1 and b) 14_1, with the corresponding moving and fixed transects, 100 and 150 m from the glacier front respectively, overlain.*

study period and, therefore, too slow for any significant movement of crevasses past the transect line between individual surveys. After initially digitising the front of Store Glacier a fixed transect was drawn on the 14_1 survey 150 m upstream using the copy parallel feature in ArcMap. A distance of 150 m was chosen so that the transect was close enough to the front in order to pick up the development of crevasses that may influence calving, but also being far enough back that crevasses can still be measured for both the 10_1 and 14_1 surveys following the glacier's retreat after calving during the days in between. The crevasse characteristics were subsequently measured along the fixed transect for the 10_1 and 14_1 surveys.

As a comparison the same characteristics were then measured again along a moving transect. A transect was initially drawn 100 m upstream of the glacier's front position during the 10_1 survey. Another transect was then drawn using the 14_1 survey, again 100 m inland of frontal position. Due to two transects being used for this sampling technique this allowed them to be further towards the glacier's front than the fixed transect. Length, width, depth and orientation were once again noted for each crevasse that crossed the transects on the 10_1 and 14_1 surveys. For both sampling methods, if a long crevasse intersected a transect, the width and depth was recorded at the point at which this occurred, rather than halfway along or by average, in order that the characteristics at the calving front specifically

could be measured. The orientation of the crevasses were subsequently illustrated in rose diagrams created in Microsoft Excel 2016.

3.2.3 Statistical Analysis

The statistical significance of the differences between crevasse characteristics along the fixed and moving transects were subsequently determined. Tests were undertaken to compare between the length, width and depth of the measured crevasses along the two 10_1 and 14_1 fixed transects and then again for the moving transects, both regionally and across the entire calving front. Additional tests were also done to identify any statistical differences between the fixed and moving transects of each survey time slice in order to determine if the positioning of the transect substantially affected the outcome of the results.

The Welch's t-test was used for this statistical analysis. This involves a two-sample location test that can be used to examine the hypothesis that two samples of data have equal means. However, importantly, although it is a variation of the Student's t-test (Welch, 1947), the Welch's t-test is more reliable when the two populations in question have unequal sample sizes and unequal variances (Ruxton, 2006). It is, thus, the most appropriate statistical test for this study as the number of crevasses measured within each region and along the whole front was different for each of the four transects used. Therefore, the Welch's t-test provides a suitable way to statistically compare the obtained values despite the differences in sample size.

3.3 Additional Analysis

3.3.1 Depth Profiles

Four depth profiles were taken along transects running parallel to the flow direction of Store Glacier. The Stack tool was implemented in ArcMap using the elevation data of the DEMs produced through SfM and profiles for each of the ten surveys was obtained. The transects used for the profiles were located where the main calving events were observed along the front during the study period (Figure 3.9). This was done so that any development of surface crevasses leading up to the calving events could be captured and analysed further.

The data was then exported to Microsoft Excel, where each time slice along the profile was plotted up. Overall, the depth profiles provided accurate elevation data from the DEMs, with clear progression over time. Notably though, there are areas of the profiles across the fjord water and melange where the DEM inaccurately shows significant elevation change. This is

particularly seen in survey 10_1 of Transect 3 and survey 14_1 of Transect 4. In these locations, the significant peaks/troughs in elevation occur due to the lack of texture on the water's surface, which makes photogrammetric reconstruction, in particular tie point identification, problematic. Nevertheless, there are no signs of major inaccuracies across the glacier surface itself. Therefore, the data was deemed suitable for research into crevasse and calving dynamics specifically, and key areas of crevasse growth were identified and examined further. The problems with the DEM data across the water and melange were additionally noted and used to aid future UAV photogrammetry research.

3.3.2 Proportion of Crevasses

In addition to recording the individual characteristics of crevasses, the overall area of crevasses across the five regions of the calving front was recorded. The area of exposed ice was also calculated in order to compare and determine how dominant the frontal crevasses are across Store Glacier.

3.3.3 Ice Loss

Furthermore, the area of ice lost through calving events between each survey was calculated. The front of Store Glacier for each of the ten surveys was digitised in ArcMap. The area between each front position where the glacier retreated was then measured and summed up for a total loss. These were subsequently added together for a progressive cumulative loss over the five-day study period.

3.3.4 Velocity Fields

Velocity datasets produced by the RESPONDER team (Chudley *et al.*, 2018) were also provided in order to analyse any patterns between it and the crevasse patterns observed across Store Glacier. First, velocity fields for the periods between surveys 12_2 and 12_3 in addition to 12_3 and 13_1 were supplied. The RESPONDER team produced the dataset through initially constructing multidirectional hillshades using GDAL 2.2 and feature tracking in open-source Matlab package OpenPIV with a spacing of 32 pixels and interrogation window of 320 pixels. Measurements below a signal-to-noise (SNR) threshold of 0.9 were then filtered out, before the velocity fields were outputted as geotiffs. They were additionally displayed using the histogram equalise stretching technique in order to best show the differences in velocity patterns across the glacier.

The interlude between surveys 12_2 and 12_3, in addition to 12_3 and 13_1, were chosen for the velocity analysis within this study as they precede the main calving events observed over the study period (see section 4.1.1). Difficulties in processing didn't allow velocity data to additionally be determined for the 13_1 to 14_1 period after the calving events, as the surface of the glacier had changed too much for feature tracking to work. Nonetheless, the two periods selected still provide an opportunity to examine how the distribution of calving events may correlate with velocity across the calving front.

3.3.5 Principal Axis of Strain

Strain rates were also calculated from surface velocity U_s and V_s components provided by the RESPONDER team. The supplied dataset detailed the components between the 12_3 and 13_1 surveys for each x and y coordinate across the study area. A code was subsequently constructed in the Python programming language and used to calculate strain rates $\dot{\varepsilon}_{xx}$, $\dot{\varepsilon}_{yy}$ and $\dot{\varepsilon}_{xy}$ and subsequently the chief strain axis, θ, as outlined by Benn (2007). The resulting axes of strain were separated by the five specified regions so that the chief orientation of strain could be determined for each individual region as well as across the entire front. These were then plotted in rose diagrams in Microsoft Excel in order for easy comparison to the orientation of crevasses also measured across the front.

4. RESULTS

4.1 Crevasse Analysis

4.1.1 Crevasse Maps

The ten crevasse maps of Store Glacier are displayed in Figure 4.1. They clearly show the movement and development of crevasses over the five-day study period as well as the occurrence of significant calving events. The calving front appears predominantly stable for the first four days, with only the enlargement of a minor inlet on the north side of Region C (Figure 4.2). However, between survey 13_1 and 14_1, there is a significant loss of ice across the entire front. This loss occurs in three main regions: 1) at the north side of Region C (Figure 4.3); 2) at the intersection of Region D (Figure 4.4); and 3) the centre of Region D (Figure 4.5).

Calving event 1 (CE1) occurs following the growth of the minor inlet, which lengthens by 91.5 m over 2 days. The 'headlands' around the inlet collapse between survey 12_3 and 13_1, resulting in retreat of 116.5 m within 6 hours. The main calving event then occurs in two parts, with the calving front retreating a maximum of 173 m on the northern side and 97 m to the south. CE2 meanwhile transpires solely between the final two surveys, with a large chunk calving off during those 36 hours. The calving front of Store Glacier retreats 189 m at this location as a result of the calving event.

The third major calving event, CE3, can be seen to start ensuing between the 12_3 and 13_1 surveys. A notable chunk of the glacier calves off between the two surveys. Simultaneously, a rift/inlet begins to develop to the north, extending 51.6 m as the calving front retreats a maximum of 139 m. This rift then extends considerably to the north for the 14_1 survey, eventually measuring 277.8 m. Of the three calving events, CE3 is the only one where a change in the characteristics of a crevasse can clearly be seen preceding it from just examining the crevasse maps by eye. Figure 4.6 outlines the development of this crevasse between survey 10_1 and 12_3. Beginning with a width of 48.3 m, the crevasse widens throughout the study period, ultimately reaching a width of 76.2 m before being the location of the initial calving event observed between the 12_3 and 13_1 surveys.

Figure 4.1a: 10_1 Crevasse Map

Figure 4.1b: 10_2 Crevasse Map

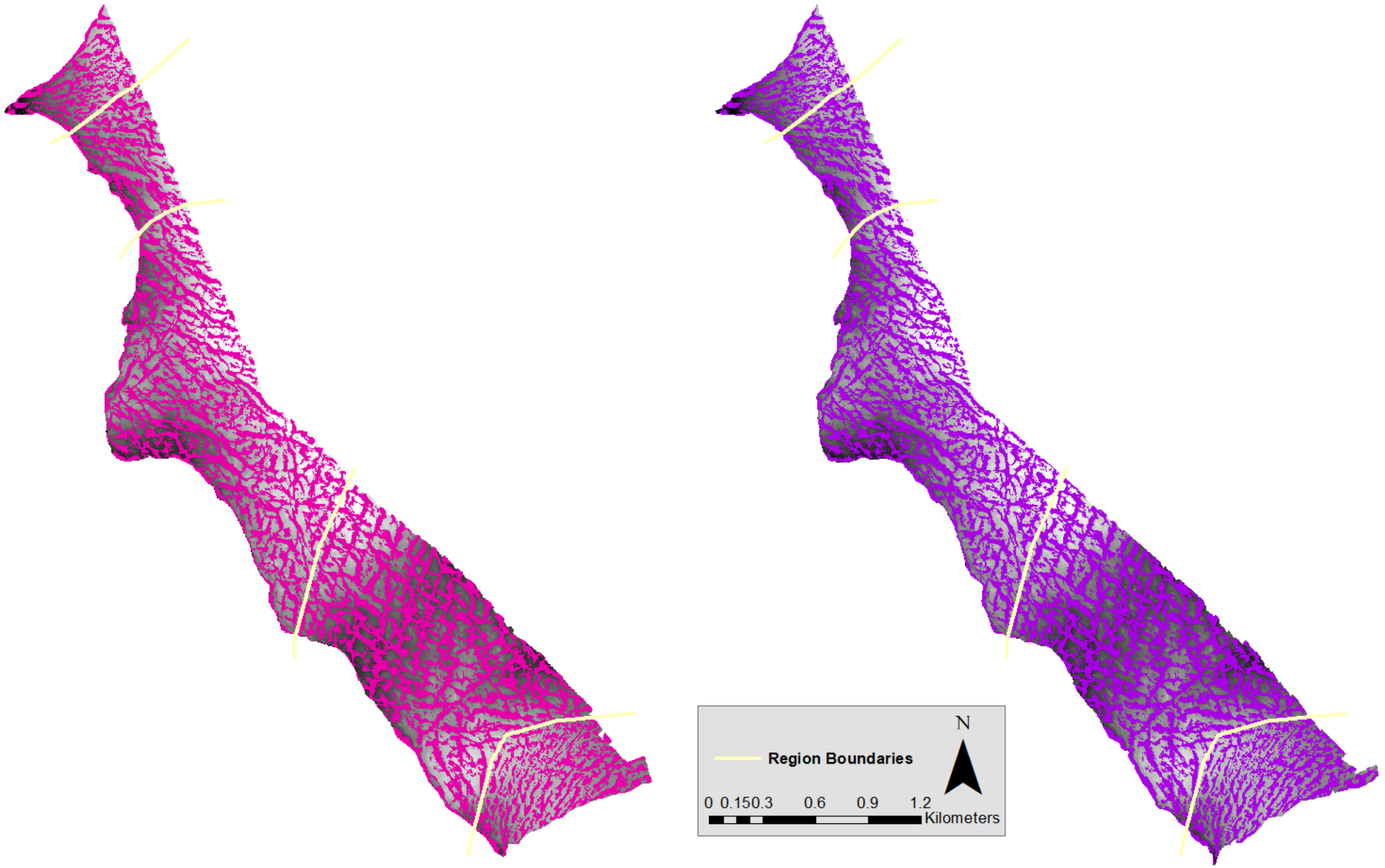

Figure 4.1c: 11_1 Crevasse Map

Figure 4.1d: 11_2 Crevasse Map

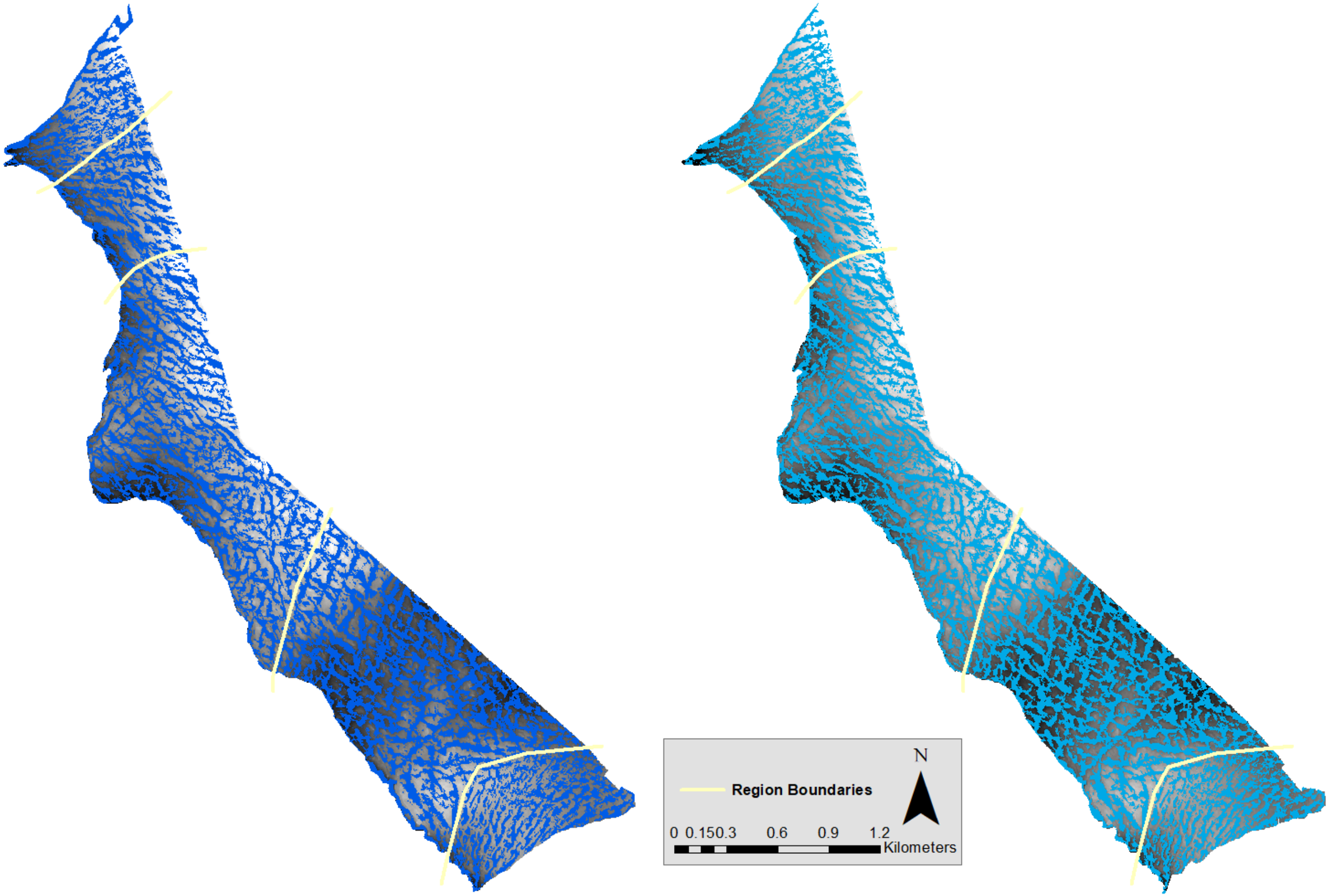

Figure 4.1e: 11_3 Crevasse Map

Figure 4.1f: 12_1 Crevasse Map

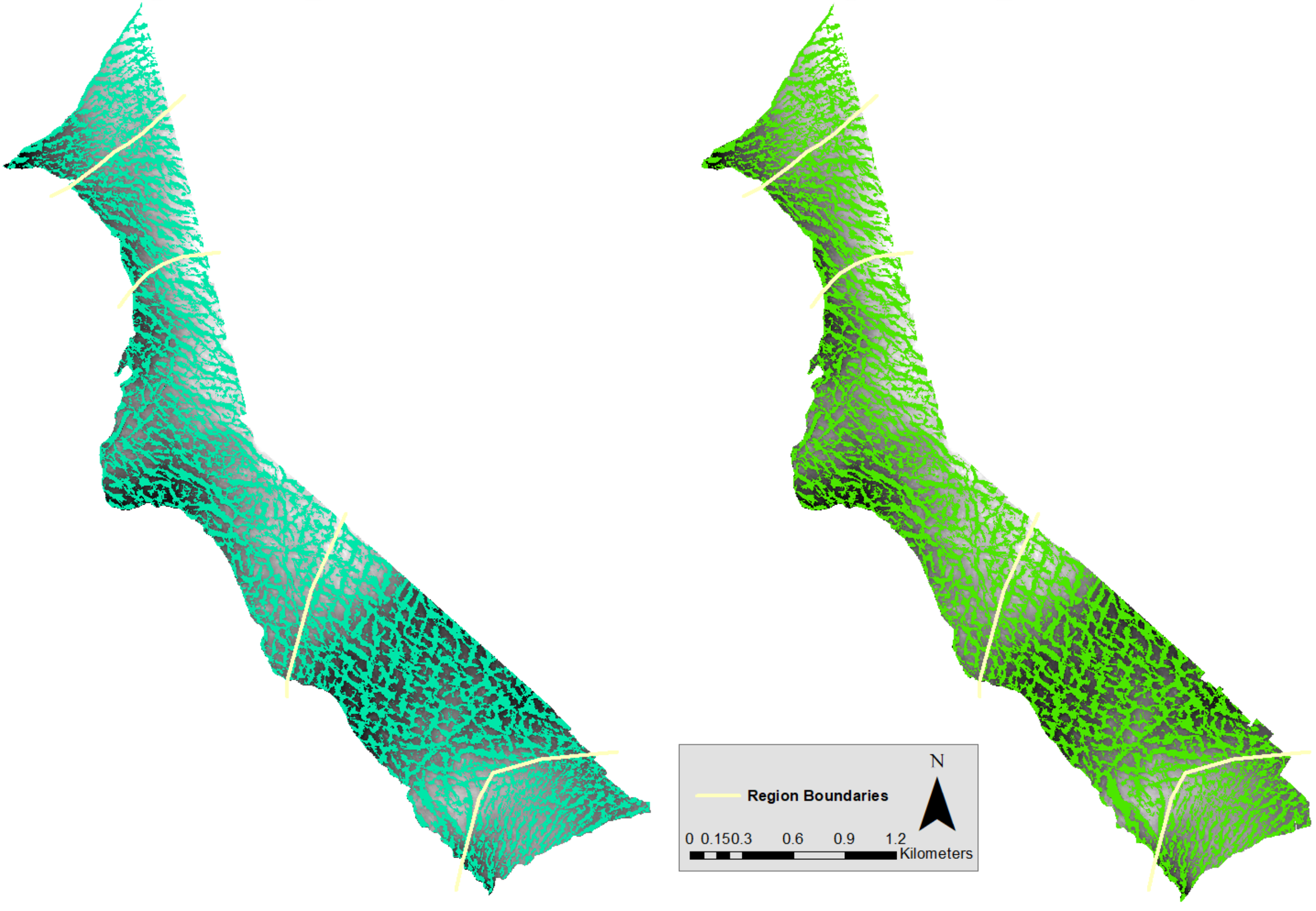

Figure 4.1g: 12_2 Crevasse Map

Figure 4.1h: 12_3 Crevasse Map

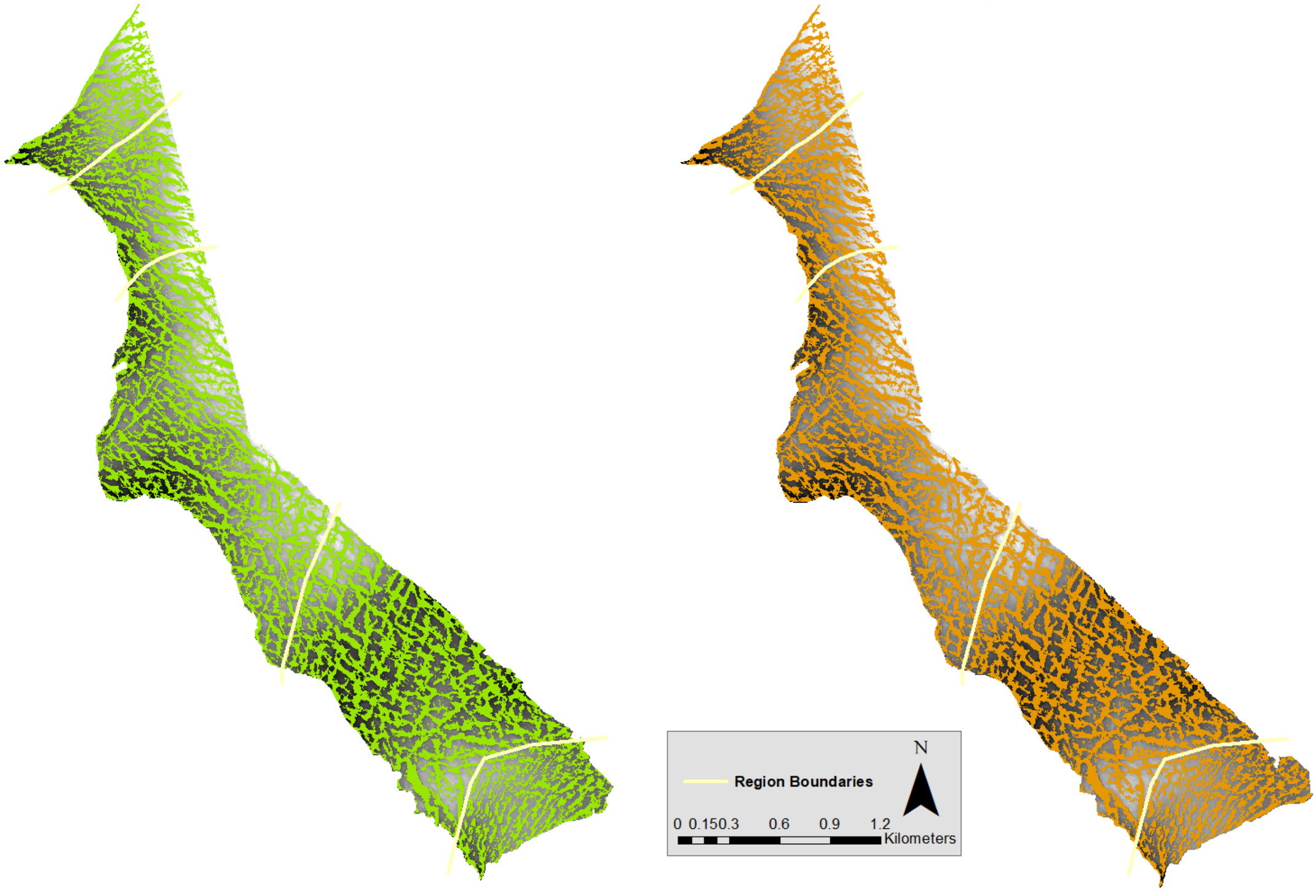

Figure 4.1i: 13_1 Crevasse Map

Figure 4.1j: 14_1 Crevasse Map

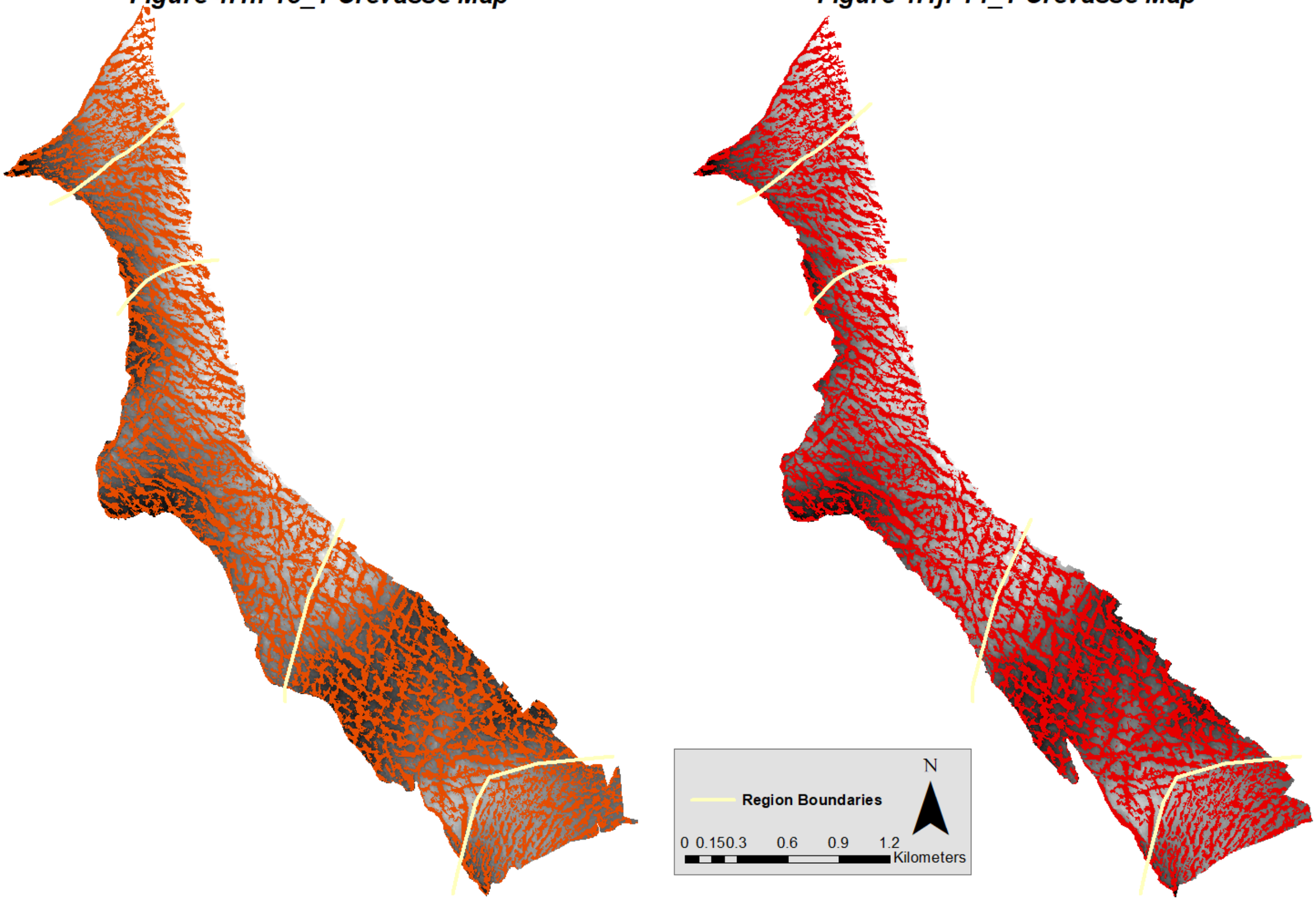

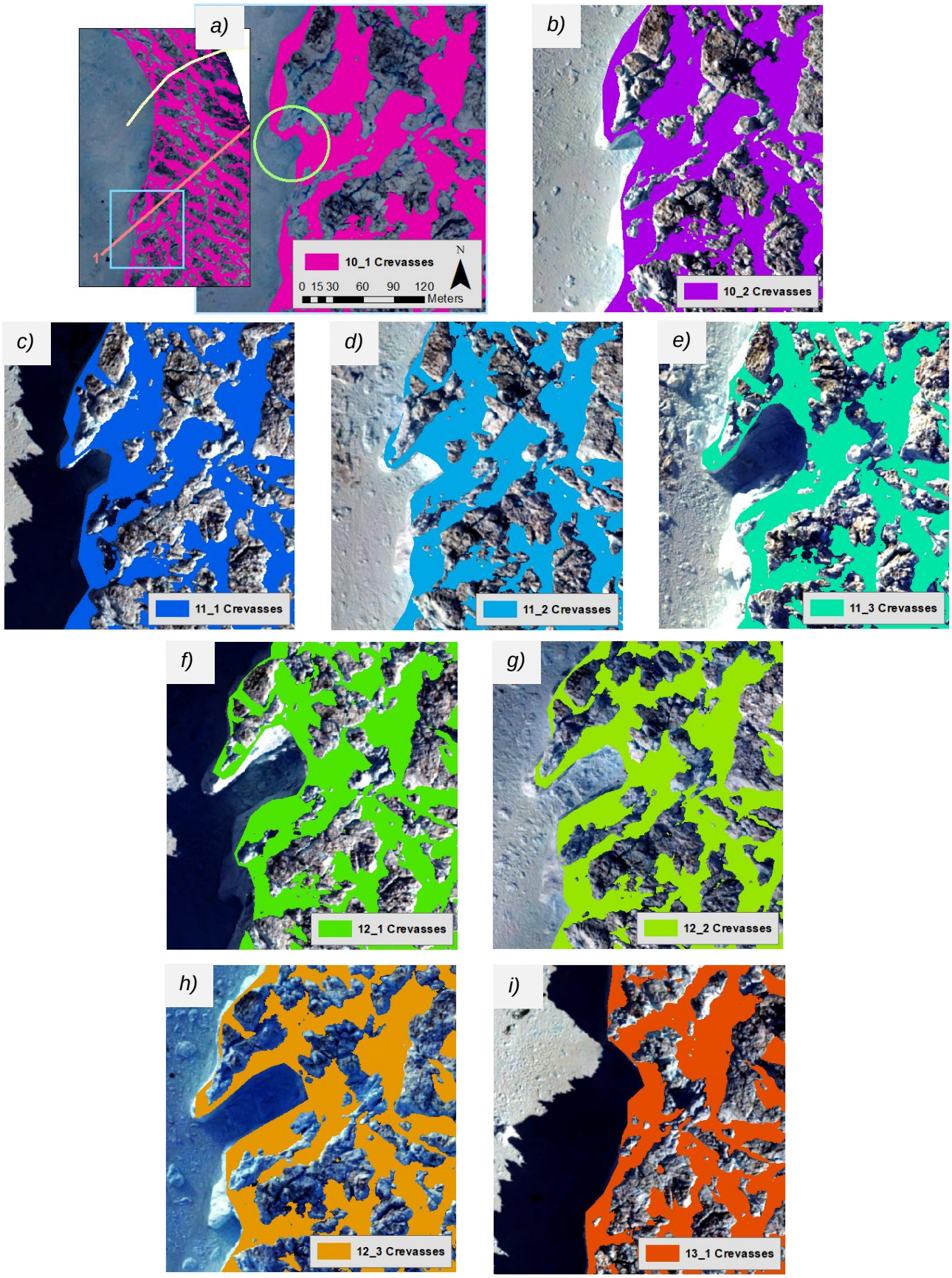

Figure 4.2: *Series of maps between surveys 10_1 and 14_1, with the orthomosaics underlying the crevasses, showing the development of the Region C inlet. The start of the inlet is outlined in green in a). The main maps are shown at the same scale; an inset detailing its regional location is given in a).*

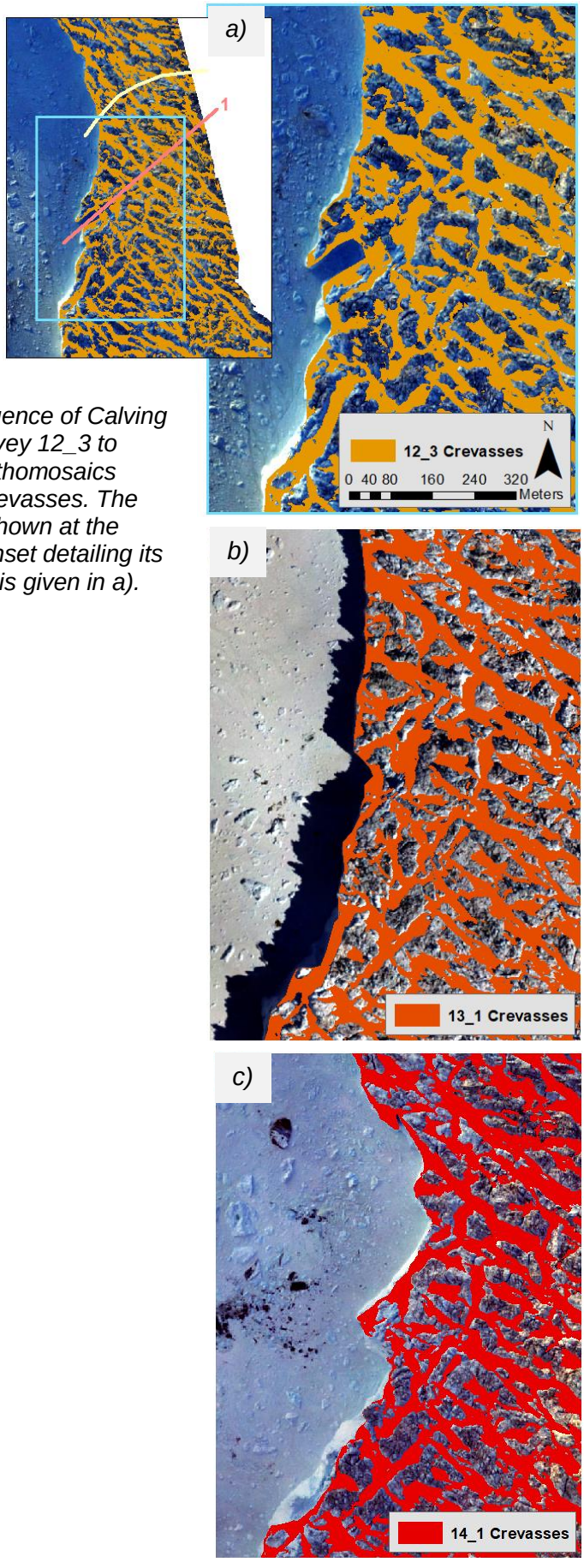

Figure 4.3: *Sequence of Calving Event 1 from survey 12_3 to 14_1, with the orthomosaics underlying the crevasses. The main maps are shown at the same scale; an inset detailing its regional location is given in a).*

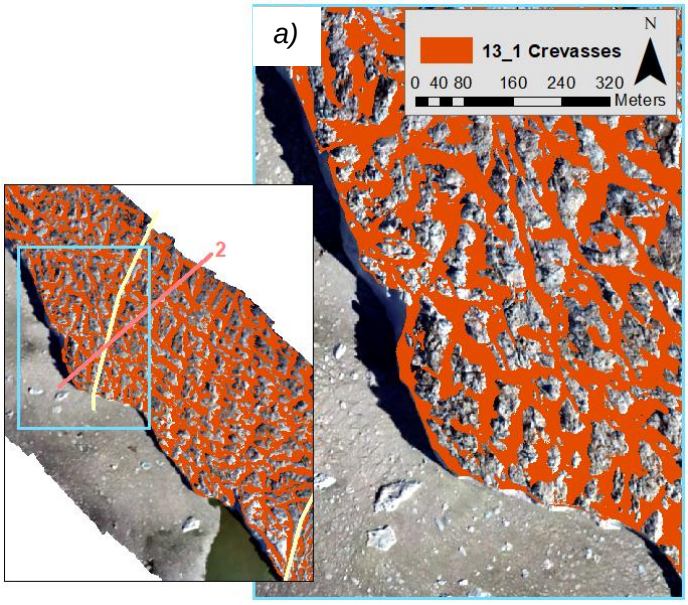

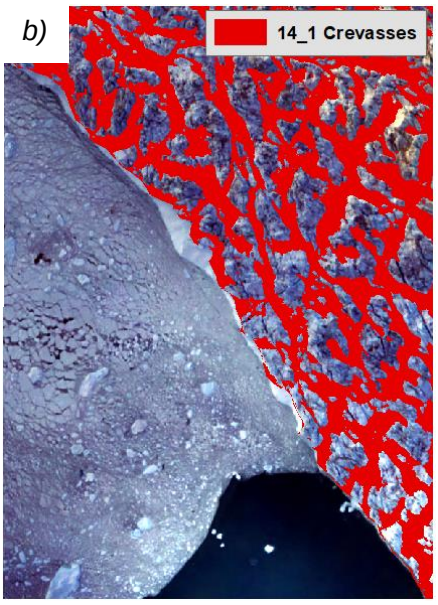

Figure 4.4: *Sequence of Calving Event 2 between surveys 13_1 and 14_1, with the orthomosaics underlying the crevasses. The main maps are shown at the same scale; an inset detailing its regional location is given in a).*

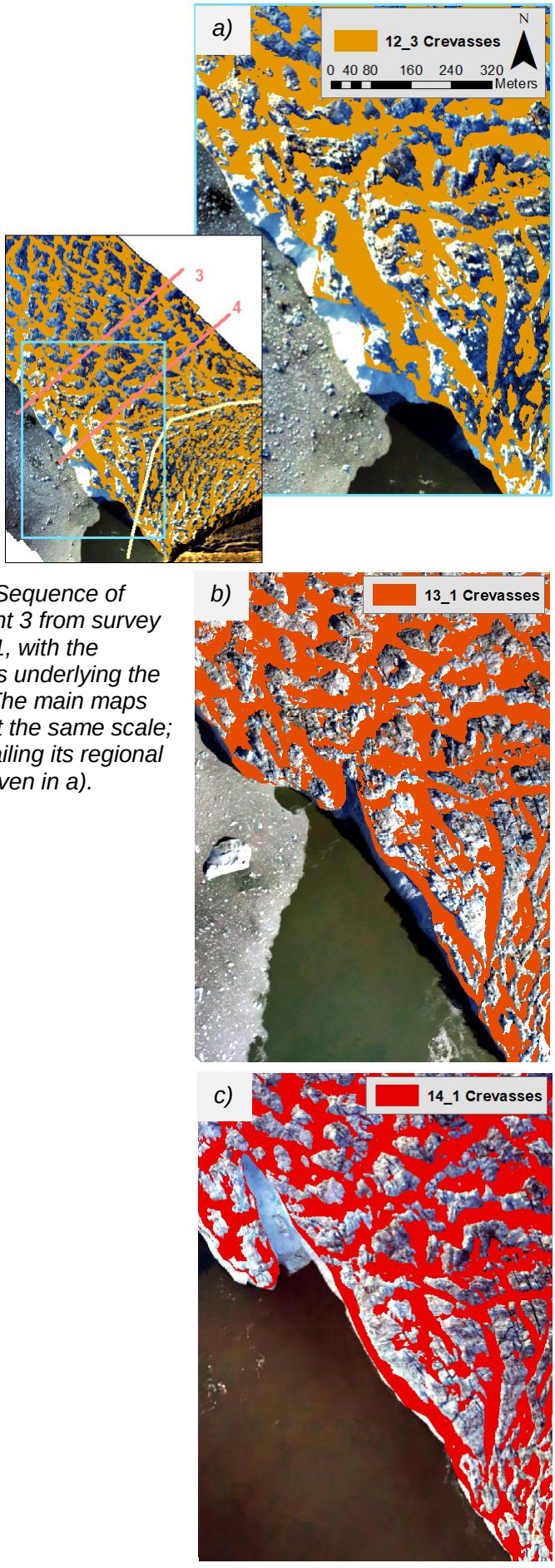

Figure 4.5: *Sequence of Calving Event 3 from survey 12_3 to 14_1, with the orthomosaics underlying the crevasses. The main maps are shown at the same scale; an inset detailing its regional location is given in a).*

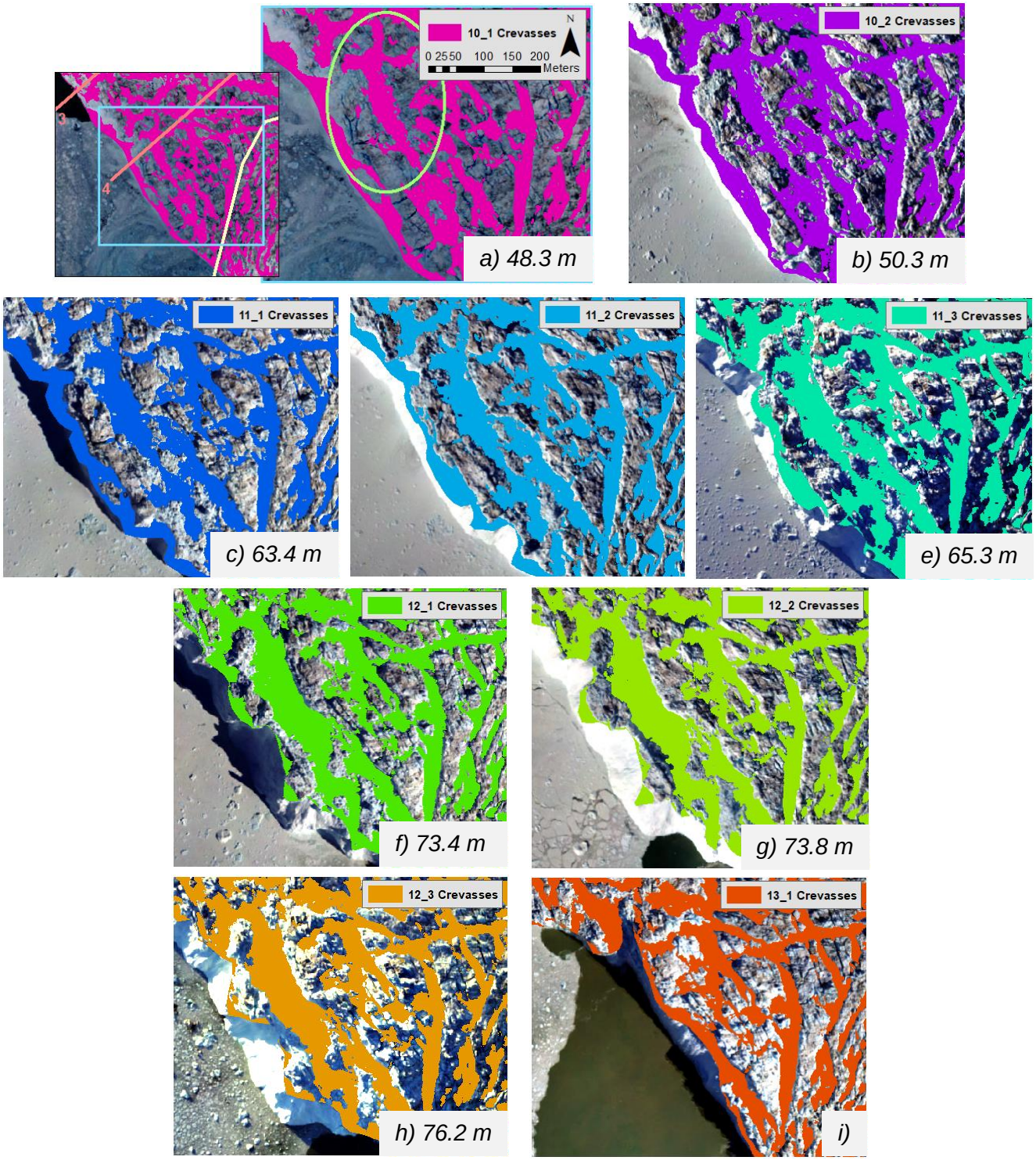

Figure 4.6: *Series of maps between surveys 10_1 and 14_1, with the orthomosaics underlying the crevasses, demonstrating the observed widening of a crevasse along Transect 4. The crevasse in question is outlined in green in a) and the width of the crevasse in each survey is given. The main maps are shown at the same scale; an inset detailing its regional location is given in a).*

4.1.2 Crevasse Characteristics

4.1.2.1 Fixed (150 m) Transect

The average length, width and depth of crevasses on the 10_1 and 14_1 surveys crossing the fixed transect is displayed in Table 4.1. Overall, the crevasses recorded along the 10_1 survey have average dimensions of 115.8 x 22.8 x 14.1 m. Regionally there is a trend of longer, wider and deeper crevasses being in the central areas of the glacier compared to the margins. This is predominantly observed on the southern side of the glacier, where the average length in Region E was 55.4 m, whereas in Region D the average length was 140.8 m. Although over double the length of those in Region E, the crevasses along the 150 m transect in Region A were still shorter on average than those in the centre.

The major differences with crevasses measured along the 14_1 survey is the average shortening within Region B and D of approximately 13.0 m, contrasted with lengthening of 27.0 and 21.5 m in Regions C and E respectively. However, the overall average length of crevasses across the entire calving front of Store Glacier remains principally the same between the first and last survey of the five-day study period. Additionally, apart from a decrease in the average width of crevasses in Region B and C of 8.8 and 5.1 m respectively, there are no other substantial changes in the width and depth of crevasses between the two surveys. Indeed, the statistical analysis undertaken and displayed in Table 4.2 indicates that there is no statistically significant change in the overall length, width or depth of crevasses across Store Glacier between the two surveys. The only statistically significant changes are between the average depth of Region B and width of Region C, which is significant to the 0.05 level (95%).

Table 4.1: *Average length, width and depth of crevasses measured across the fixed transect over the 10_1 and 14_1 surveys for each region and overall across the entire glacier front.*

Fixed Transect Survey	Dimension (Average)	Region A	Region B	Region C	Region D	Region E	Overall
10_1	Length (m)	117.1	133.5	119.9	140.8	55.4	115.8
	Width (m)	21.5	30.0	24.2	23.6	12.2	22.8
	Depth (m)	11.8	19.4	15.0	11.3	12.1	14.1
14_1	Length (m)	115.8	120.9	146.9	127.2	76.9	130.4
	Width (m)	21.8	21.2	19.1	27.8	18.4	21.0
	Depth (m)	8.0	14.0	13.4	14.3	12.8	13.1

Table 4.2: *P-Values of the statistical comparisons between the length, width and depth of crevasses measured across the fixed transect over the 10_1 and 14_1 surveys for each region and overall across the entire glacier front. Those values statistically significant to the 0.05 level (95%) are highlighted in green.*

Fixed Transect P-Values	Region A	Region B	Region C	Region D	Region E	Overall
Length	0.962	0.775	0.347	0.730	0.457	0.398
Width	0.968	0.0756	0.0107	0.344	0.0907	0.263
Depth	0.126	0.0216	0.433	0.321	0.847	0.420

The orientation of crevasses along the fixed transect of the 10_1 survey are shown in the rose diagrams of Appendix 1. The overall orientation of crevasses also varies by region. Region C has the most dominant singular orientation, with crevasses clearly centred around the NW-SE axis despite some spread across most other directions. Crevasses in the next largest region, D, while also being chiefly orientated in a NW-SE direction, additionally have a larger proportion positioned in a more N-S and NE-NW direction. This corresponds with the criss-cross nature of the crevasses seen in Figure 4.1. The margins of the glacier, however, both have crevasses orientated in one specific direction. In the north (Regions A and B) crevasses centre around the ENE-WSW and E-W axes, while in the south crevasses are evidently focused in a NNE-SSW direction.

There is little change in the overall orientation of crevasses within each region along the fixed transect from the 14_1 survey (Appendix 2), with any changes in the dominant direction only involving one step of the compass. If anything, the NW-SE and WNW-ESE axes become even more dominant in regards to the overall orientation of crevasses across the entire front.

4.1.2.2 Moving (100 m) Transect

The characteristics of crevasses recorded along the 10_1 moving transect are shown in Table 4.3, with fractures having average dimensions of 121.0 x 19.0 x 13.7 m. The pattern of longer, wider and deeper crevasses being found within the central regions of the glacier roughly remains, with a slight reduction in the lengths observed in Region C (121.1 m) compared to Regions B (223.9 m) and D (127.3 m). There is a general decrease in the length, width and depth of crevasses between the 10_1 and 14_1 surveys across all five regions. The main exception to this is the increase in average length of crevasses within Region A, which is one of only two statistically significant changes between the two moving transects, with a p-value of 0.0454 making it significant at the 0.05 level (Table 4.4). The other statistically significant change is that of the depth of crevasses from Region B,

obtaining a p-value of 0.0309. None of the changes in length, width or orientation across the entire front of Store Glacier were statistically significant.

Again, most of the regions along the 10_1 moving transect have a dominant crevasse orientation (Appendix 3). There is a clear NW-SE and WNW-ESE tendency of crevasses in Region C despite a few in a perpendicular direction. Regions A and B also have crevasses in a similar orientation, while the dominant direction in Region E is NNE-SSW. The crevasses in Region D once again have the most spread in terms of orientation, with the criss-cross pattern of crevasses remaining even with the moving transect being 50 m closer to Store Glacier's calving front. As with the fixed transect there is little change when comparing the crevasse orientation along the moving transects of the 10_1 and 14_1 surveys (Appendix 4). Any changes in the dominant direction are once more only by one compass position, with no sudden perpendicular changes.

Table 4.3: *Average length, width and depth of crevasses measured across the moving transects over the 10_1 and 14_1 surveys for each region and overall across the entire glacier front.*

Moving Transect Survey	Dimension (Average)	Region A	Region B	Region C	Region D	Region E	Overall
10_1	Length (m)	44.1	223.9	121.1	127.3	73.1	121.0
	Width (m)	9.3	20.4	19.5	22.9	10.9	19.0
	Depth (m)	9.3	23.8	13.6	11.6	16.0	13.7
14_1	Length (m)	98.9	112.4	95.9	113.2	70.4	99.6
	Width (m)	15.7	19.1	17.7	24.5	14.1	19.0
	Depth (m)	8.3	14.9	12.3	10.8	12.6	12.1

Table 4.4: *P-Values of the statistical comparisons between the length, width and depth of crevasses measured across the moving transects over the 10_1 and 14_1 surveys for each region and overall across the entire glacier front. Those values statistically significant to the 0.05 level (95%) are highlighted in green.*

Moving Transect P-Values	Region A	Region B	Region C	Region D	Region E	Overall
Length	0.0454	0.159	0.193	0.631	0.917	0.125
Width	0.0834	0.739	0.341	0.652	0.143	0.955
Depth	0.526	0.0309	0.453	0.697	0.450	0.169

4.1.2.3 Fixed vs Moving Transect

The overall average length, width and depth of crevasses across the entire front during the 10_1 survey is relatively similar between the fixed and moving transects. Regionally, there are notable differences in all areas except Region C. Having the transect 50 m closer to the calving front results in a pronounced reduction in the average length of crevasses in Regions A and D of 73.0 and 13.5 m respectively. Conversely, there is an increase in the average crevasse length of 90.4 m in Region B and 17.7 m in Region E. Nonetheless, the average

depth remains fairly similar between the fixed and moving transect measurements. Table 4.5 lists the p-values of statistical tests comparing the fixed and moving transects. This identifies that for the 10_1 survey the only statistically significant difference between the crevasses recorded along these transects is their width, with a p-value of 0.017 being significant to the 0.05 level.

The overall orientation of crevasses is also consistent between the two 10_1 surveys (Appendix 1 and 3). The NW-SE direction is visibly the dominant direction across the entire front for the fixed transect. While the WNW-ESE direction is increasingly prevailing on the moving transect, there is no dramatic change in chief direction. Nevertheless, regionally there are slight differences. In region D the moving transect 50 m closer to the calving front has an increased proportion of crevasses in N-S direction, but the criss-cross pattern of crevasses within this region still remains with a reasonable spread of orientations. The chief orientation of crevasses within regions A and B also shifts, but further south.

Comparing the 14_1 transects reveals that there is an overall fall in the length, width and depth of crevasses along the moving transect versus the fixed transect (Table 4.1 and 4.3). This is seen for the vast majority of variables within each region as well. Nonetheless, Table 4.5 outlines that only the difference in length between the two 14_1 transects was statistically significant, with a p-value of 0.036.

Similarly to the 10_1 transects, the overall orientation of crevasses across Store Glacier along the 14_1 fixed and moving transects remains analogous, with the WNW-ESE and NW-SE axes being the prevailing orientation for crevasses despite a spread across all directions. Conversely to the 10_1 transects however, there is very little change regionally between the two transects; the dominant orientation within each region remains constant or only moves by one compass mark.

Table 4.5: *P-Values of the statistical comparisons between the length, width and depth of crevasses measured across the moving and fixed transects over the 10_1 and 14_1 surveys across the entire glacier front. Those values statistically significant to the 0.05 level (95%) are highlighted in green.*

Survey	Dimension	P-Value
10_1	Length	0.752
	Width	0.0170
	Depth	0.747
14_1	Length	0.0359
	Width	0.203
	Depth	0.037

4.2 Depth Profiles

The four sets of depth profiles taken across Store Glacier are displayed in Appendices 5, 6, 7, and 8. The depth profile along Transect 1 displays the initial development of the inlet in Region C before CE1 seen in Figure 4.1. While the front position stays relatively stable between surveys 10_1 and 11_2, the inlet predominantly develops following 51.9 m of retreat between 11_2 and 11_3 (Figure 4.7a). It is visible in the 11_2 profile that an 18 m deep crevasse develops close to the glacier's snout; however, there is no evidence for a similar surface crevasse near the location of the new terminus position at 11_3. The frontal position and glacier surface topography then remains comparatively unchanged between 11_3 and 12_3. As the inlet headland breaks off overnight (Figure 4.1) a surface crevasse grows approximately 245 m along the transect, reaching a maximum depth of 25 m (Figure 4.7b). Store Glacier then retreats to the position of this crevasse between 13_1 and 14_1 following CE1.

Transect 2's depth profile portrays the changes observed before CE2 at the boundary between Region C and D (Figure 4.1). Little change in the surface topography is observed between surveys 10_1 and 12_3, as the calving front slowly advances by 44.6 m (Figure 4.8a). Nonetheless, CE2 takes place between 13_1 and 14_1, during which Store Glacier retreats 184.6 m (Figure 4.8b). However, there is no obvious surface crevasse that enlarges before the calving event at the new position to which the snout retreats. Indeed, the fall in topography around 225 m along the transect is observed in the depth profiles of each previous nine surveys, with no increase in depth observed over the four days.

Transects 3 and 4 provide depth profiles at the south side of Region D at the location of CE3. Transect 4 reveals the development of the crevasse that is observed to be widening in Figure

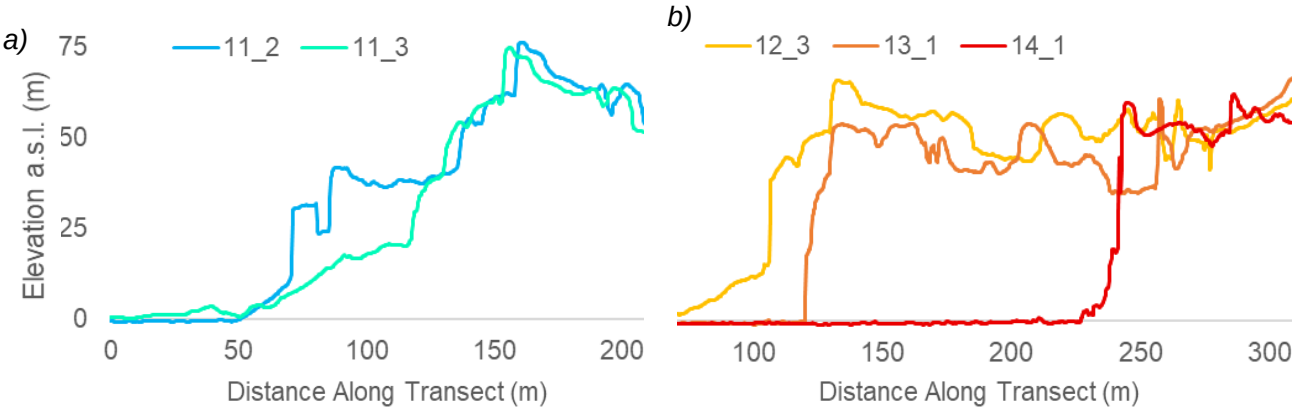

Figure 4.7: *Detailed sections of the depth profiles along Transect 1 showing: a) retreat of the ice front between surveys 11_2 and 11_3 as the inlet develops; b) development of a surface crevasse between 12_3 and 13_1 followed by retreat to this position after CE1 in survey 14_1.*

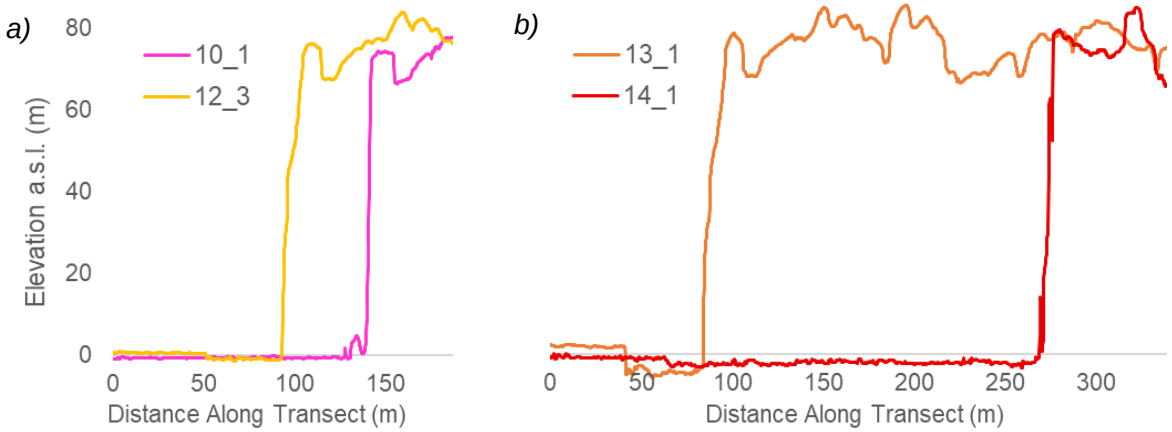

Figure 4.8: *Detailed sections of the depth profiles along Transect 2 showing: a) advance of the glacier between surveys 10_1 and 12_3; b) development of a surface crevasse between 12_3 and 13_1 followed by retreat to this position after CE1 in survey 14_1.*

4.6. An initial depth of 12.7 m, the crevasse first deepens between survey 10_2 and 11_1 by 12.2 m to 24.9 m (Figure 4.9a). Staying a similar depth throughout the next day, the crevasse then propagates 20.6 m further overnight between the 11_3 and 12_1 survey to a depth of 45.5 m (Figure 4.9b). The crevasse then again stays fairly stable during the 12th July (Figure 4.9c). However, at the onset of CE3 between survey 12_3 and 13_1 the glacial snout retreats 122.2 m to the back edge of the where the deepening crevasse was previously

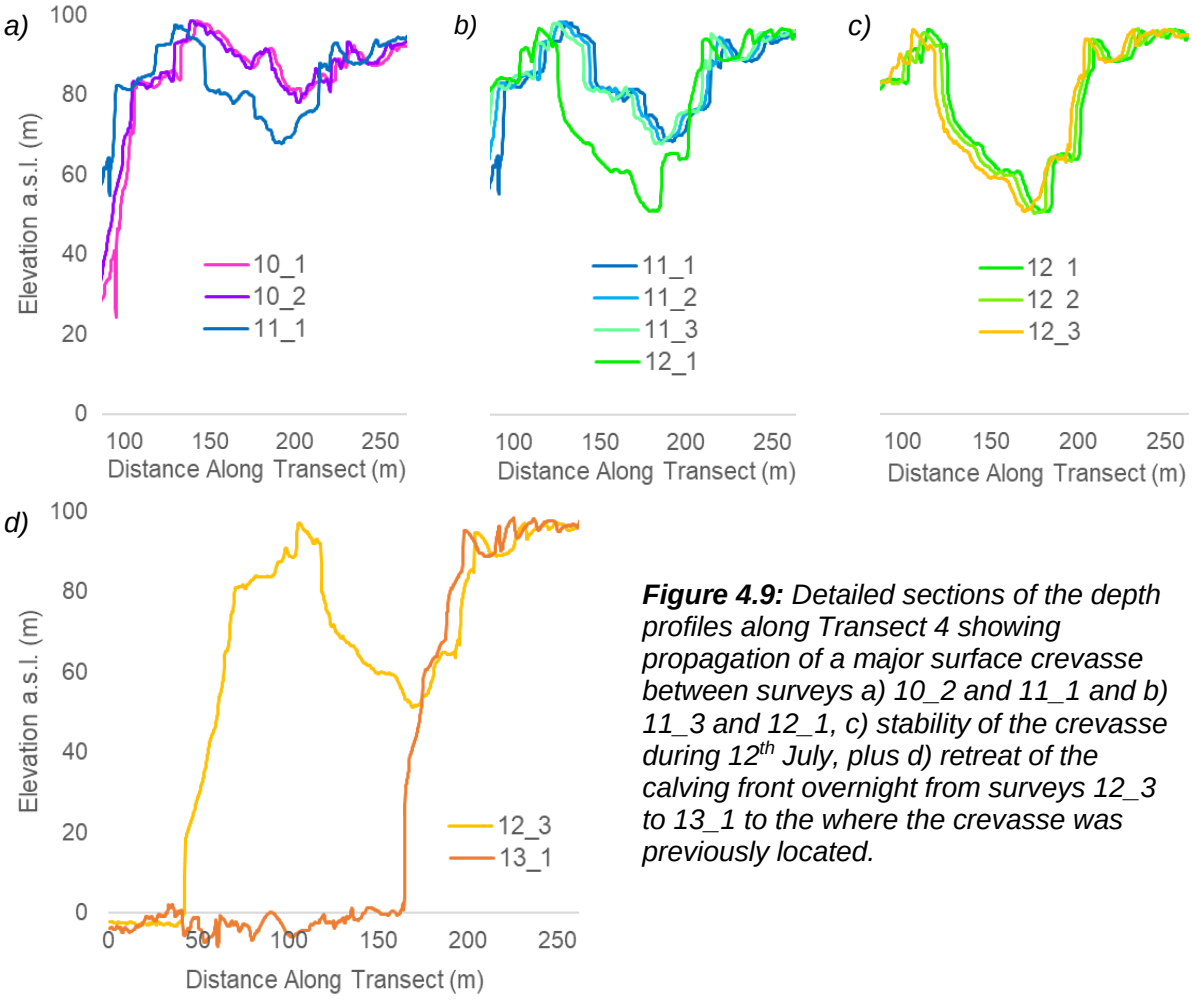

Figure 4.9: *Detailed sections of the depth profiles along Transect 4 showing propagation of a major surface crevasse between surveys a) 10_2 and 11_1 and b) 11_3 and 12_1, c) stability of the crevasse during 12th July, plus d) retreat of the calving front overnight from surveys 12_3 to 13_1 to the where the crevasse was previously located.*

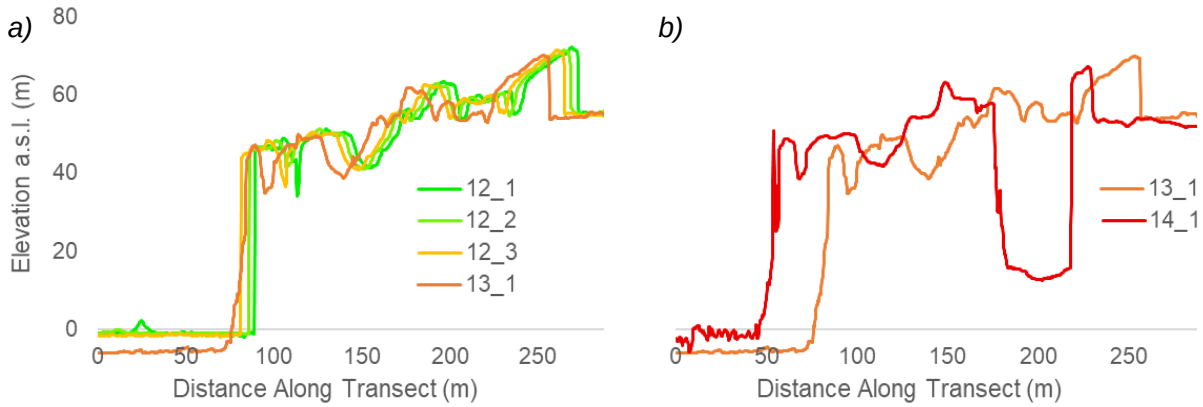

Figure 4.10: *Detailed sections of the depth profiles along Transect 3 showing: a) advance of the glacier between surveys 12_1 and 13_1, and particularly the more significant advance at the onset of CE3 between 12_3 and 13_1; b) the continuation of CE3 and the development of the rift seen Region D from survey 13_1 to 14_1.*

located (Figure 4.9d). The calving front then only advances slightly from survey 13_1 to 14_1, despite the erroneous peak in DEM elevation seen approximately 80 m along the transect over open water (c.f. Figure 4.5).

Transect 3 displays the continued development of CE3. The surface topography along Transect 3 remains fairly stable throughout the majority of the study period. At the same time as the calving event along Transect 4 between survey 12_3 and 13_1 occurs though, there is a larger advance of the ice compared to that between previous surveys (Figure 4.10a). However, between survey 13_1 and 14_1 the glacier breaks in two and a rift is formed 200 m along the transect (Figure 4.10b), as also observed in Figure 4.5. At the point which this rift crosses Transect 3 it is 53.9 m deep.

Table 4.6: *Average proportion of crevasses mapped compared to the total area and area of bare surface ice over the ten surveys.*

Region	Surface	km²	%
Entire Glacier	Total Area	4.06	-
	Crevasse Area	2.00	49.2
	Surface Ice Area	2.06	50.8
A	Total Area	0.342	-
	Crevasse Area	0.169	49.4
	Surface Ice Area	0.173	50.6
B	Total Area	0.384	-
	Crevasse Area	0.190	49.5
	Surface Ice Area	0.194	50.5
C	Total Area	1.47	-
	Crevasse Area	0.701	47.8
	Surface Ice Area	0.767	52.2
D	Total Area	1.41	-
	Crevasse Area	0.723	51.3
	Surface Ice Area	0.687	48.7
E	Total Area	0.464	-
	Crevasse Area	0.219	47.2
	Surface Ice Area	0.245	52.8

4.3 Proportion of Crevasses

The average total mapped area, crevasse area and ice area for each of the five regions and entire front are displayed in Table 4.6. Overall, the surveyed area of Store Glacier covers 4.06 km^2, with 2.00 km^2 of that being crevasses and 2.06 km^2 surface ice. Indeed, even on a regional level it is clear that there is a 50:50 split between the area of crevasses and ice across the full extent of Store

Glacier's calving front. Region D, however, is the only one to have greater than 50% of its surface area covered by crevasses. The remaining four regions all have crevasses covering slightly less than 50% of their surface.

4.4 Ice Loss

Figure 4.11 shows the ice front of Store Glacier at the time of each of the ten surveys. It details that Store Glacier was predominantly advancing for most of the study period with any calving events too small to be picked out by human eye. Then, as outlined in section 4.1.1, between survey 12_3 and 14_1 the main significant calving events occurred, resulting in the calving front of Store Glacier retreating in a number of locations.

The area of ice lost through calving between each survey, as well as the cumulative total loss up until that point in the study period, is noted in Table 4.7. While there is some ice loss between the 11_1 and 11_3 of the order of 20-30,000 m^2, this confirms that the majority of ice lost through calving occurs at the end of the study period. Indeed, the 170,524 m^2 lost between the 13_1 and 14_1 surveys is greater than the 145,407 m^2 of ice lost from the previous four days combined.

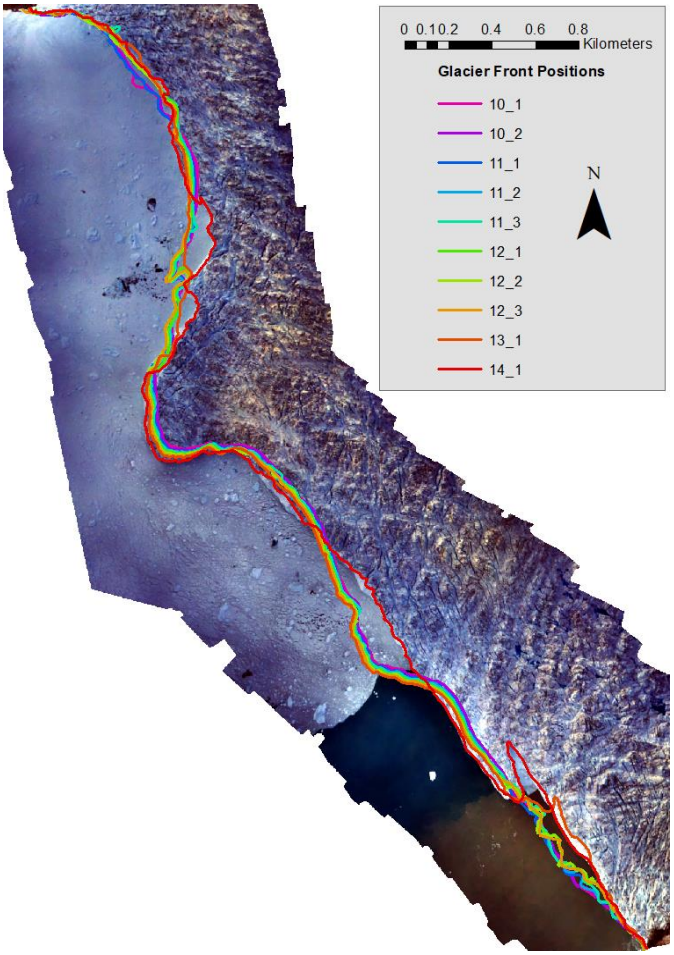

Figure 4.11: *Digitised frontal positions of Store Glacier for each of the ten surveys throughout the study period. The colour of each line corresponds with those seen in the crevasse maps and depth profiles.*

Table 4.7: *Total and cumulative ice loss between each survey.*

Start Survey	End Survey	Total Ice Loss (m^2)	Cumulative Ice Loss (m^2)
10_1	10_2	3099	3099
10_2	11_1	3635	6734
11_1	11_2	30286	37020
11_2	11_3	22860	59880
11_3	12_1	10152	70032
12_1	12_2	1038	71070
12_2	12_3	7460	78530
12_3	13_1	66877	145407
13_1	14_1	170524	315931

4.5 Velocity Fields

The velocity fields for the periods between surveys 12_2 and 12_3 as well as 12_3 and 13_1 are displayed in Figure 4.12. As would be expected, there is a clear transition from slow-flowing ice at the margins to fast-flowing ice at the centre. The pattern of velocity also matches well with the pre-chosen regions, with Regions A and E corresponding to the lowest velocity values, Regions B and D covering the transition areas, while the glacier moves fastest in the central Region C. The biggest anomaly, however, is located at the southern side of Region D, where there is an area of considerably fast-flowing ice at the calving front of Figure 4.12a, despite much slower velocities observed inland. This area corresponds with the development of the crevasse that is seen in both the initial crevasse maps (Figure 4.6) and the depth profile along Transect 4 (Figure 4.9). Thus, this area subsequently disappears in Figure 4.12b as CE3 ensues between surveys 12_3 and 13_1. A similar, smaller area of fast-flowing ice is seen at the north side of Region B, again down-flow of a region of lower velocity.

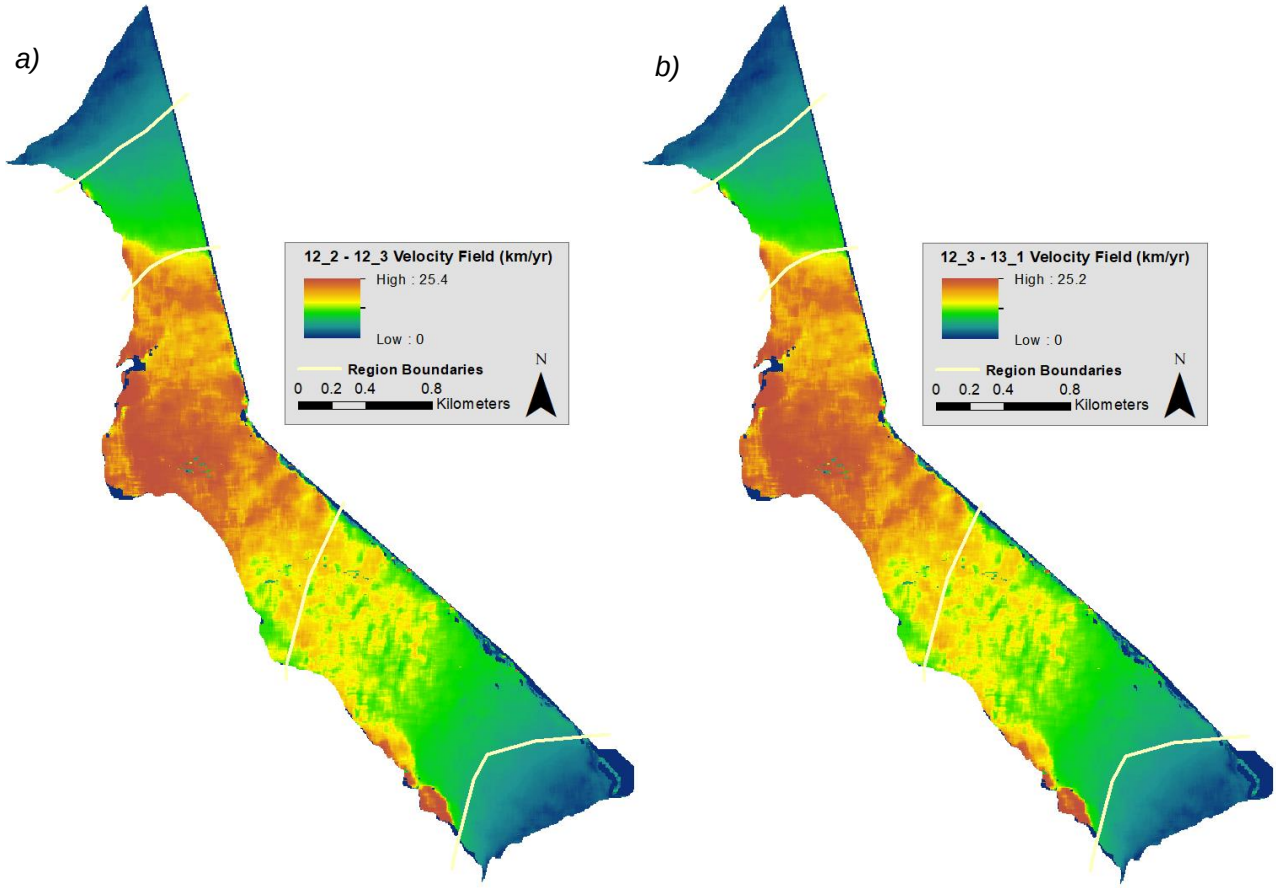

Figure 4.12: *Velocity fields of Store Glacier for the periods between surveys a) 12_2 and 12_3, plus b) 12_3 and 13_1.*

4.6 Principal Axis of Strain

The principal axis of strain calculated for each of the five regions as well as across the entire glacier between surveys 12_3 and 13_1 are displayed in the rose diagrams of Figure 4.13. Overall there is a clear tendency for strain to be applied in an east-west direction, with a lean towards a ENE-WSW orientation. This is roughly in line with the direction of glacier flow, which generally travels from north east to south west. A similar pattern is found on a regional level, with Region D having an analogous pattern in strain angle. Region C again additionally has a comparable spread in the angle of strain, even if more centralised around a E-W orientation. Strain in both Regions A and E is applied in the strongest ENE-WSW direction and the closest to reaching a NE-SW alignment. The pattern of strain axes in Region B strays the furthest from the overall trend though. Here, while still not having any strain applied in a north-south direction, there is no dominant orientation, with strain being applied evenly between a NE-SW and NW-SE angle.

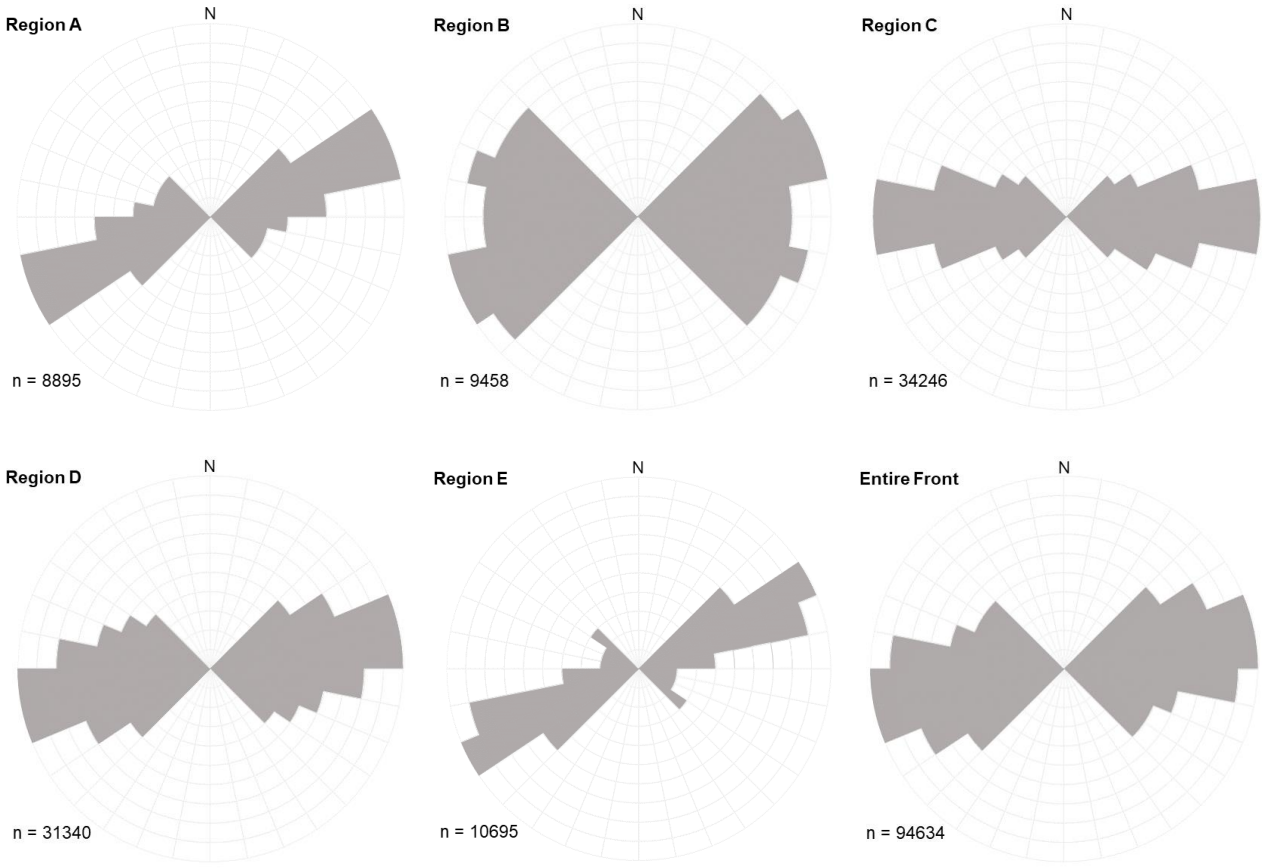

Figure 4.13: *Rose diagrams displaying the principal axes of strain applied to the ice in each of the five region, plus across the entire calving front, between the 12_3 and 13_1 surveys.*

5. DISCUSSION

The objectives of this investigation were to identify the changes in crevasses across Store Glacier over sub-daily time scales, and assess the overall influence of their development on calving events observed over the same study period. This chapter aims to analyse the results outlined above in order to evaluate these objectives and provide ideas on the likely progression of other similar glaciers in the future.

5.1 Relationship Between Crevasse Patterns and Occurrence of Calving Events

The 50:50 split between crevasses and surface ice across all regions (Table 4.6) confirms that the glacier's snout is covered in a crevasse field, rather than a few random fractures, and therefore an appropriate field site to undertake this research. In addition, it demonstrates that an effective smoothing process was implemented while creating the maps. The Gaussian blurring, and subsequent processing, involves smoothing the DEM in order that a consistent level is used for the boundary between those areas of the glacier classed with 'positive' and those with 'negative' topography values. Therefore, the uniformity of the 50:50 split across an average of all ten surveys demonstrates the data produced here is reliable for further analysis.

In general, there is very little change in the overall pattern of crevasses over the five-day study period. Rather the ten maps of Figure 4.1 show a clear and steady movement of the crevasses along Store Glacier's flow line in a south easterly direction. Those crevasses at the margins are observed to move less than those in the centre and often undergo a rotated movement as the side of the crevasse closer to the centre travels faster than that at the side. This matches the velocity profile calculated here for Store Glacier (Figure 4.12) and the traditional view of glacier flow as a result of drag by the valley sides (Raymond, 1971).

Before the three main calving events between surveys 12_3 and 14_1 much of the front calves in small chunks that are often difficult to pick out by eye. The calving front digitising in Figure 4.11 helps visualise where calving does occur, although also shows that the snout of Store Glacier was advancing for much of the study. Nevertheless, much of the calving occurs perpendicular to the flow direction and planar along the front, instead of cutting into the snout. There is, however, one main exception to this: the development of the inlet at the north of Region C (Figure 4.2). The calving associated with its enlargement cuts into the snout of the glacier, resulting in more retreat than in many other locations along the front.

Such inlets are often seen as a result of calving induced by concentrated meltwater plumes, as noted previously along Store Glacier by Chauché *et al.* (2014). Moreover, Todd *et al.* (2018) noted the location of where the two enduring concentrated conical plumes at Store Glacier are believed to be located and their size (Figure 5.1). Comparing these positions to the maps produced here in Figure 4.1 the northern plume appears to correspond with the site of the Region C inlet. While there is no obvious embayment at the south end of the glacier in correlation with the southern meltwater plume, it is possible that this second plume had some form of influence in the development of the rift following the initiation of CE3 (Figure 4.5). However, it is noteworthy that the gap between surveys 13_1 and 14_1 is the largest between all surveys, at 35.8 hours (Figure 3.1). Thus, the reduction of survey frequency across this period prevents the same amount of analysis of the ongoing processes behind certain changes than earlier in the study period. Nonetheless, meltwater plumes likely still play a role in controlling the calving dynamics along the front of Store Glacier.

The ice loss statistics in Table 4.7 reveal further information about the pattern of calving over the study period. There is a clear peak in the area of ice lost at the end of the research period from 12_3 onwards, but particularly between surveys 13_1 and 14_1 in correspondence with CE1, 2 and 3. There is an additional far smaller increase in ice loss around survey 11_2, most possibly relating to the large expansion in the Region C inlet at

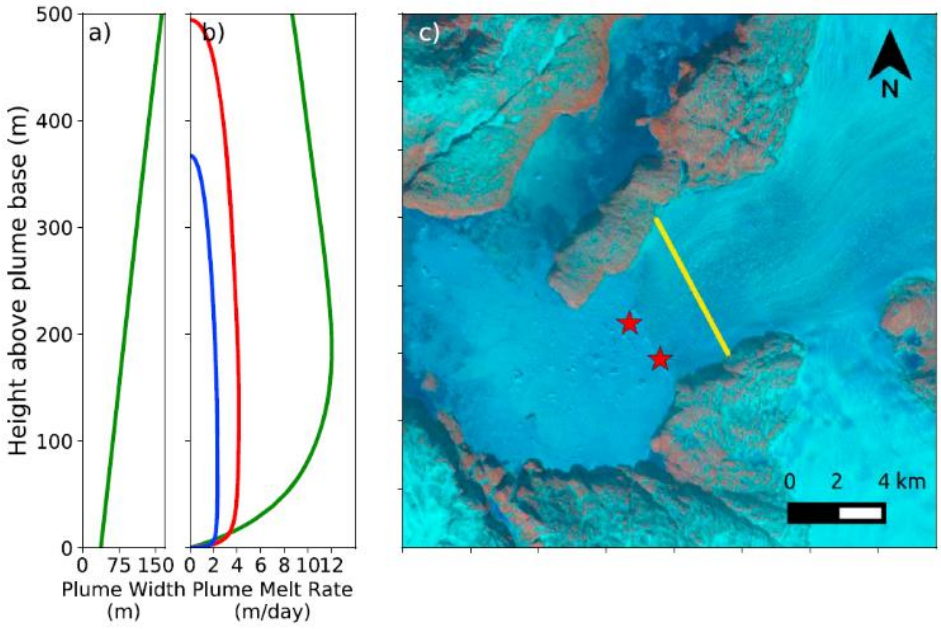

Figure 5.1: *Characteristics and location of the two meltwater plumes observed at Store Glacier: a) profile of plume width; b) melt rate of distributed plumes in winter (blue) and summer (red), plus concentrated plums (green); c) position of the concentrated conical plumes. Taken from Todd et al. (2018)*

this time. However, overall there is no clear pattern in the calving events at this five-day timescale. The lack of change in the crevasse arrangement, combined with the absence of a regular calving pattern, demonstrates that producing crevasse maps and analysing such two dimensional bird's eye views alone is not sufficient to determine any clear links between the two processes. Further analysis of crevasse characteristics is needed to identify how crevasse development may impact upon the calving dynamics of a glacier.

5.2 Impact of Ice Dynamics on the Types of Surface Crevasses

The absence of any substantial changes in the orientation of crevasses, both along the fixed and moving transects (Appendix 1 to 4), corresponds with the observed non-existence of variances in the overall pattern of crevasses across the ten survey maps of Figure 4.1. However, the constant orientation of crevasses helps identify the types of fractures forming across the glacier. Comparing with the principal angle of strain being applied to the ice at that location (Figure 4.13) also aids in determining how the forces within the ice are acting and impacting crevasse formation.

The dominant angle of strain in both Regions A and E is in a ENE-WSW direction. This contrasts slightly with the chief orientation of crevasses in these regions, which are generally orientated along E-W and NNE-SSW transects in Region A and E respectively. Despite the alternative directions of crevasse orientation in these two regions, they are all still often at a 45° angle to the primary angle of strain. Based on the strain equations outlined by Benn (2007) this shows that deformation in Regions A and E is dominated by simple shear. Crevasses in these regions are therefore predominantly Mode III fractures (Figure 2.4). In addition, due to the slow nature of glacier flow in these two regions (Figure 4.12), as a result of drag from the valley sides, it would be understandable that compressive flow is occurring here. Thus, this compressive flow combined with shear strain means the crevasses in Regions A and E can be termed as splaying crevasses (Figures 2.6 and 2.7b) and this matches the style of crevasses observed in the produced maps (Figure 4.1).

Meanwhile, Appendices 1 to 4 demonstrate that the dominant orientation of crevasses in Regions B and C generally falls along a NW-SE and WNW-ESE direction. This is perpendicular to the NE-SW flow of Store Glacier, demonstrating that these crevasses are Mode I fractures, formed through extensional forces and flow (Figure 2.4). These crevasses can therefore be classed as transverse crevasses (Figure 2.7a), which Benn (2007) proposes are formed through pure shear. But, it is noteworthy that the principal strain angle in Region C is in a E-W direction (Figure 4.13), and not completely parallel to the flow

direction. Thus, there is likely a combination of pure and simple shear acting upon the ice and crevasses in this region, but with a majority of pure shear in order to form the transverse crevasses.

A combination of pure and simple shear is also found in Region B. However, Figure 4.13 shows that there is no dominant angle of strain in this region, with strain being applied relatively equally between a NW-SE and NE-SW direction. This is probably due to Region B being a transitionary zone in terms of glacier velocity between the margin and centre of the glacier (Figure 4.12). Therefore, there will also be a transition in regards to both the type of strain being applied and the category of crevasses present, with an increase in the dominance of pure shear towards the south of the region.

Region D is perhaps the most complex in terms of crevasse orientation, with Appendices 1 to 4 showing that a number of crevasses are orientated in a NW-SE/WNW-ESE direction, while others are rotated at approximately 45° and are at a N-S angle. This is displayed further in Figure 4.1 where a criss-cross pattern of crevasses is observed across the region in each survey. Despite the chief axis of strain in Region D orientated in a ENE-WSW direction (Figure 4.13), and therefore roughly parallel to the direction of glacier flow, the criss-cross fractures hint that both Mode I transverse and Mode III shear fractures are found in Region D and forming the observed crevasse pattern through mixed mode failure.

While Region D is also a transitionary zone between the slow velocity of the margins and higher flow speeds found in Region C, akin to Region B (Figure 4.12), the criss-cross pattern is observed across much of the region, suggesting that the forces producing this distribution of crevasse are fairly consistent across the region instead of gradually switching. It is important to note that Region D is the part of Store Glacier that is positioned over the basal overdeepening, and thus the ice is understood to be floating at this location (Todd *et al.*, 2018). McGrath *et al.* (2012) observed that surface troughs on the floating Larsen C ice shelf in Antarctica were located above radar-detected basal crevasses and surface crevasses subsequently appear along the peaks and sides of these undulations. A similar situation may occur in Region D of Store Glacier, with the basal crevasses modelled by Todd *et al.* (2018) in this area of the snout being an additional factor influencing the patterns and spread of observed surface crevasses. Thus, it may not always be possible to explain the surface pattern and orientation of crevasses through analysing the direction of glacier flow and primary strain angle alone.

5.3 Link Between the Growth of Crevasses and the Incidence of Calving Events

5.3.1 Transect Analysis

The very little significant change in overall and regional observations of crevasse characteristics along the fixed and moving transects (Tables 4.1 and 4.2) suggests that their mass-measurement cannot always be relied upon to determine the location of calving events. Although there are a few statistically significant variations, such as between the widths of Region C along the fixed transect and the depths of Region B on the moving transect, these are suitably random that they do not appear to provide any solid evidence of consistent and noteworthy change.

This may initially be surprising, as theory suggests that calving occurs once crevasses propagate through a glacier (Nick *et al.*, 2010), thus a difference in depth between the first and last survey may at least be expected. If crevasses did also continue to open as a wedge while they grew in depth (Meier, 1958; Meier *et al.*, 1957), a change in width may also be anticipated to occur. However, despite this, it is important to note that not all crevasses will ultimately relate to the location of a calving event and only lengthen/widen/deepen a small amount over their lifetime. Additionally, even if certain crevasses do lead to calving, the events in question may be small, with just a fraction of the front falling off, if for instance a propagating crevasse meets a joint or fracture within the ice. For such small events very little deepening or widening would occur before the calving took place. Therefore, by measuring all crevasses across the calving front it is likely that many of these were also picked up and influenced the averages used for statistical analysis.

Furthermore, the lack of statistically significant differences between the measurements taken across the fixed and moving transects (Table 4.5) insinuates that either method is a suitable way for sampling the measurements of crevasse characteristics. Nevertheless, two values did come out statistically significant: the difference in noted widths between the fixed and moving transects of the 10_1 survey, in addition to the variation in length of the two transects drawn along the 14_1 survey. Due to the moving transect being 50 m closer to the calving front than the fixed transect these differences may be expected, as the crevasses will have had a longer time to develop and grow before they hit the 100 m moving transect compared to the 150 m fixed transect. However, the variables that are significantly different are not consistent between the 10_1 and 14_1 comparisons, plus there is still a lack of statistically significant variation between all / a majority of variables. Therefore, there is deemed to be no serious case for choosing one form of transect over the other when

sampling crevasses across a glacier front. Ultimately though, regardless of the chosen transect, the overall characteristics of crevasses over short-timescales do not appear to demonstrate any correlation with calving events.

5.3.2 Depth Profiles

While the overall characteristics of crevasses may not show an influence on calving, the depth profiles taken across Store Glacier demonstrate that looking at the development of individual crevasses may be more beneficial.

5.3.2.1 Transect 4

This is observed particularly along Transect 4 (Figure 4.9; Appendix 8), where one singular crevasse is seen to enlarge throughout the first three days of the study period. The crevasse deepens by 45.5 m between survey 10_1 and 12_3 and is also noted to widen by 27.9 m over the same time period (Figure 4.6). Following this though, the crevasse becomes the exact location of the onset of CE3, suggesting that within the twelve hours between survey 12_3 and 13_1 this crevasse propagated through the entirety of the ice or connected to an upcoming basal crevasse.

Perhaps noteworthy is that this propagation and calving event occurred overnight. In fact, each of the periods within which the crevasse deepened were also overnight (between 10_2 and 11_1, plus 11_3 and 12_1), while the crevasse remains fairly stable during the day. The development of crevasses is mostly related to the flow of glaciers and the tensile stresses resulting from expansion (Nye, 1952; Paterson, 1994). Thus, if this were to be the main factor influencing the expansion of this particular crevasse it would suggest that Store Glacier's velocity peaks overnight. However, this would initially seem unlikely and contradictory to the numerous previous studies that have clearly demonstrated the diurnal velocity cycle of glaciers across the GIS, with a peak often cited around 4 to 5 pm local time (Figure 5.2) (Bartholomaus *et al.*, 2007; Shepherd *et al.*, 2009; van de Wal *et al.*, 2015). Indeed, Doyle *et al.* (2018) found a similar diurnal cycle takes place at Store Glacier. This velocity peak of glaciers has been linked to the meltwater influx that increases throughout the day as daily temperatures climb and maxes out at approximately 1 pm (Figure 5.2). Once this meltwater makes its way to the base of a glacier it acts as a lubricant and increases the ability of the ice to move forward via basal sliding (Bartholomew *et al.*, 2010; Joughin *et al.*, 2008b; Zwally *et al.*, 2002a).

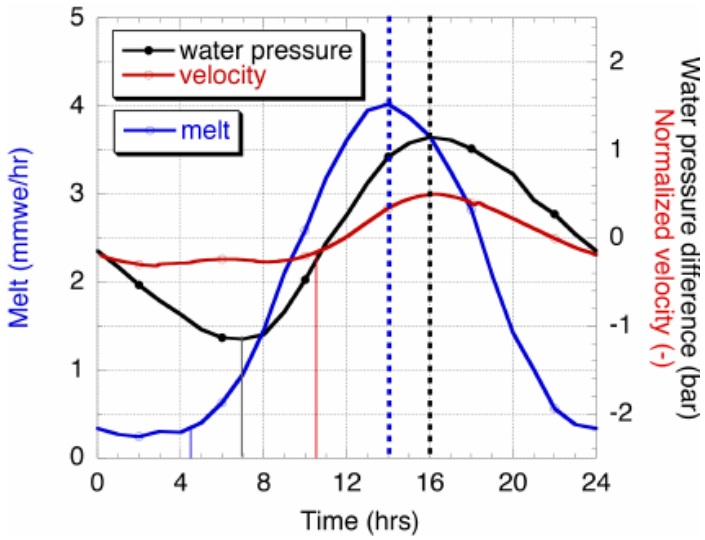

Figure 5.2: *Average daily cycle of meltwater, velocity and water pressure of glaciers in South-West Greenland. Vertical solid lines signify the start of acceleration in the morning, and vertical dashed lines denote the peak values. Taken from van de Wal et al. (2015).*

Nevertheless, despite this late afternoon peak in velocity, the majority of deepening and widening that this crevasse undergoes, in addition to the onset of CE3, happens in the twelve hours between 10 pm and 10 am, based on the flight times of the UAV surveys undertaken in this study (Figure 3.1). In the end, however, it is possible that, due to the slow nature of glacier flow (average of 0.695 m hr^{-1} over the study period at Store Glacier), it takes this amount of time for the increase in tensile stresses as a result of the peak velocity to spread through the ice and influence the development of a crevasse.

There are a limited number of other factors that operate on a diurnal cycle that could result in such a pattern. For instance, although the development of many fractures in rocks can occur at night through freeze-thaw weathering (Matsuoka and Murton, 2008), it is doubtful that changes in air temperature would be able to impact ice in the same way as rock structures due to its physical properties. It could be possible, however, that due to the flow of meltwater into crevasses during the day that hydrofracturing occurs more intensely during the evening and overnight as a result. Unfortunately, there are a very limited number of water-filled crevasses observed over Store Glacier during the study period, with the majority not being located at the calving front. Therefore, it is difficult to comprehensively determine the impact of meltwater hydrofracturing on the observed changes in crevasse characteristics. Nonetheless, the small temporal scale of this study has provided an insight into a diurnal nature of crevasse propagation not thoroughly recorded before and confirms that our understanding of crevasse development is not yet fully realised.

5.3.2.2 Transect 3

The depth profiles also show that calving events across Store Glacier don't just have an immediate impact on the calving front, but can also influence crevasse formation in other nearby locations. This is observed along Transect 3 (Figure 4.10; Appendix 7). Here the glacier surface remains stable throughout the majority of the study period, with the flow of the glacier moving forward the only obvious change between surveys 10_1 and 12_3. However, as outlined in section 4.2, a rift suddenly develops between survey 13_1 and 14_1. Although the elevation at Transect 3 does not reach sea level within this rift (Figure 4.10), analysis of the DEM and orthmosaic at this location suggest that the ice calved during the creation of the rift is floating/stuck in this area. This shows that the calving event is still relatively fresh and the ice has not had a chance to break free from its confines and float out into the fjord. Thus, the depth profile only reaches a minimum elevation of 12.8 m a.s.l., where the calved ice is still located.

This rift is first witnessed though in survey 13_1 as a small inlet before it extends fairly rapidly further north west by the time of the 14_1 survey. It is believed that the initial expansion of the inlet is related to CE3 as it is located exactly at the northern edge of where the propagating crevasse was in survey 12_3. Figure 4.5 also shows that as the rift grows it does so along a crevasse that predominantly appears and/or widens between surveys 12_3 and 13_1, i.e. at the same time as CE3 occurs and as seen in Figure 4.10. Therefore, not only does CE3 contribute directly to Store Glacier's calving flux over the five days, but also indirectly leads to further calving by causing further crevasses to enlarge and propagate through the glacier's entire thickness. Such processes would not have been observed if the 4D data collected here had been done so over a larger frequency.

5.3.2.3 Transect 1

Another example of a likely calving-inducing crevasse that appears suddenly instead of enlarging gradually throughout the study period is seen to the north end of Store Glacier across Transect 1 (Figure 4.7; Appendix 5). Despite the development of the inlet in the glacier front at this location, through the probable influence of a meltwater plume (Figure 4.2), the surface topography of Store Glacier remains fairly constant until survey 12_2. Minor changes in surface height are then observed before the 25 m deep crevasse develops in survey 13_1 as outlined in Figure 4.7b. The position of the new glacier front in survey 14_1 suggests that CE1 occurred following the propagation of this identified crevasse through the full height of the glacier, or to a basal crevasse below. Again, it is possible that the sudden

development of this crevasse occurred in a similar manner to that along Transect 3, with a prior calving event leading to transfer of tensile stresses through the ice.

This prior calving event is the calving of the headlands around the meltwater plume inlet between the 12_2 and 12_3 surveys (Figure 4.4). Further analysis of the crevasse maps and an additional depth profile demonstrates this theory further. An additional crevasse, about 25 m to the north of Transect 1 and directly upflow of the inlet's headland, is observed to notably deepen by 6.8 m between surveys 12_3 and 13_1 (Figure 5.3). Relatively insignificant in surveys before this, the calving of the headlands may have allowed this crevasse to expand through a loss in buttressing from ice in front of it. Connecting to the crevasse observed in the depth profiles along Transect 1 (Figure 4.7b), this second crevasse may have helped initiate CE1 if continued propagation occurred in the run up to survey 14_1. The observations across Transects 1 and 3 therefore signify that while it is important to monitor the development and propagation of individual crevasses to understand a glacier's calving activity, it is also valuable to have an understanding of where previous calving events have occurred, and thus where tensile stresses could consequently be allowed to increase leading to further calving events.

A comparable situation has been observed at Jakobshavn Isbræ, where rises in velocity following a reduction in buttressing from its ice tongue has been suggested as a contributor to increases in discharge over recent decades (Joughin *et al.*, 2012; Vieli and Nick, 2011).

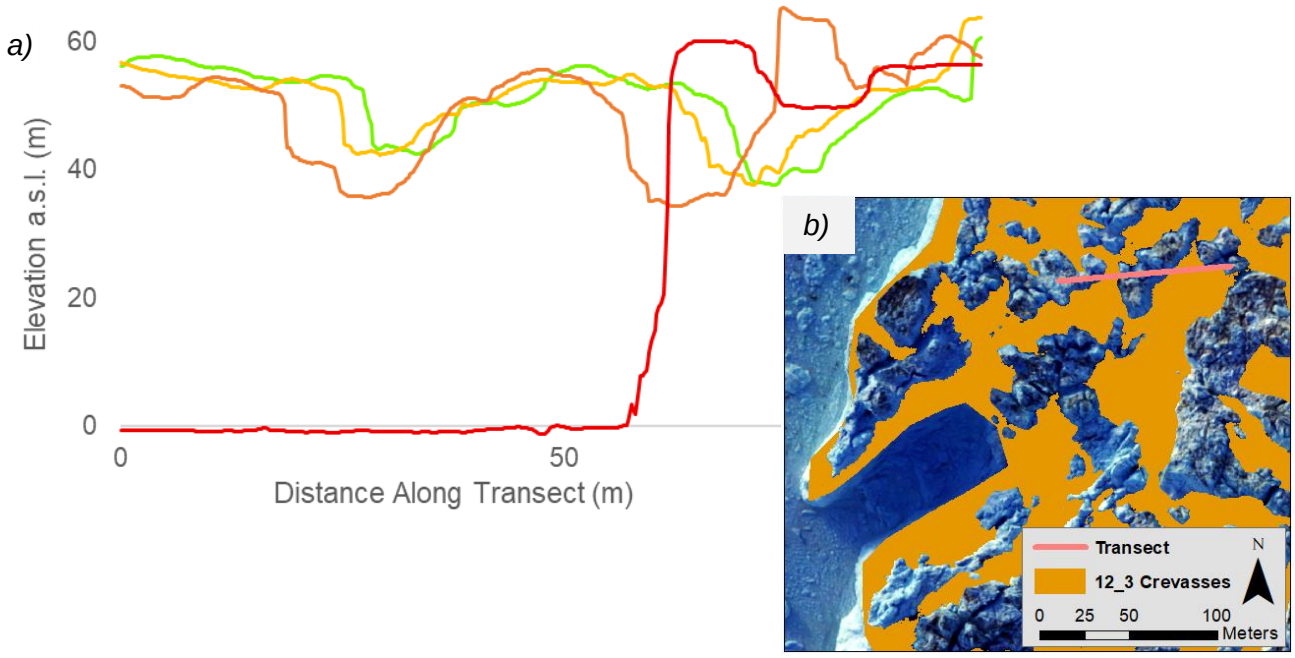

Figure 5.3: *Depth profile near the Region C inlet showing a) the propagation of a crevasse directly inland of the inlet's headland, which is connected to the crevasse where Store Glacier retreats to following CE1. An inset detailing the location of the transect and crevasses in relation to the headland and inlet is shown in b).*

While Store Glacier is buttressed by seasonal melange rather than a floating ice tongue, the same principal may be applicable to the development of crevasses following calving events detected in this study. It may, therefore, be expected that other large calving events would result in the destabilisation of nearby ice and increased glacier velocity and discharge through the spread of longitudinal stress into the surrounding ice. Unfortunately, due to the problems processing velocity data for the period between the 13_1 and 14_1 surveys it is difficult to properly judge if a speed-up was observed at Store Glacier following CE1, 2 and/or 3. However, it is notable that Nick *et al.* (2012) observed no acceleration in glacier flow following the break-up of 25% of the ice tongue of Petermnann Glacier, North West Greenland. Indeed, there is no obvious large speed-up between the two velocity fields of Figure 4.12 succeeding the calving of the inlet headlands in Region C and onset of CE3 at Transect 4 in Region D. Thus, while such calving events may not lead to large changes in velocity and discharge, the identification of stress propagation and resulting crevasses here suggests there is at least some small local influence.

5.3.2.4 Transect 2

However, measuring and monitoring surface crevasses does not always allow the identification and prediction of calving events. This is the case for Transect 2 and the lead up to CE2. Figure 4.8 and Appendix 6 demonstrate that surface topography of Store Glacier remains almost completely unchanged throughout the entire study period. The only major change in profile is the 187 m retreat between survey 13_1 and 14_1 as a result of CE2, with no obvious propagation of a surface crevasse to signal the possibility that a calving event may take place. However, since a calving event does take place the glacier must still have been ‘cut through’ in some way. The DEMs produced through SfM in this study can only show the surface topography of Store Glacier and not the basal characteristics underneath. Therefore, the lack of surface crevasse development indicates that CE2 may have been brought about through the propagation of basal crevasses upwards instead.

Transect 2 is located at the intersection of Region C and D. This is notably the same location where Store Glacier is believed to be floating due to the presence of the overdeepening at its base (Todd *et al.*, 2018). The snout at this location may therefore be capable of undergoing buoyancy-driven calving as a result of the upward torque forces of the water underneath pushing and rotating the calving front, allowing basal crevasses to propagate up (Figure 2.9; Benn *et al.*, 2017a, b; Murray *et al.*, 2015b; Wagner *et al.*, 2016). This type of calving would also correlate with the size of CE2; buoyancy-driven calving produces large

tabular icebergs and CE2 measures at 98,835 m^2, the largest of all calving events observed during the study period. Furthermore, the location of CE2 also corresponds with the position of the highest basal crevasses modelled across Store Glacier by Todd *et al.* (2018) (Figure 2.8b). Thus, it is proposed that basal crevasses were the sole contributor to the calving of CE2 and play just as an important role in controlling the dynamics of Store Glacier as surface crevasses.

5.4 Limitations of the Research Project

This research has shown that SfM products produced from UAV photography can provide a key way to understand the development of crevasses at a glacier snout and their subsequent impact on calving events. However, the project also had some limitations, for instance:

i) Gaps in the dense point cloud

Although SfM was able to produce a high resolution, precise reconstruction of Store Glacier, Figure 3.4 shows a number of gaps and areas where the UAV imagery was not incorporated into the dense point cloud picked up, especially along the snout. Hole filling during the creation of the orthomosaic was therefore an important decision to make. To partially resolve this issue, imagery from terrestrial/time-lapse photography could be used to expand this study further by picking up these frontal areas of the snout (Mallalieu *et al.*, 2017; Petlicki *et al.*, 2015).

ii) Size of datasets

The size of SfM datasets can lead to large problems with their handling and management (Passalacqua *et al.*, 2015; Rychkov *et al.*, 2012). Due to the high-resolution nature of the DEM and dense point cloud produced in this study, these limitations were initially felt at the start of this research, with the available computer's processing speed slowing down significantly when trying to open specific files. Fortunately, an alternative station was found upon which to undertake the research. Indeed, methods have been developed for reducing the computational size of such data when needed but maintaining the sub-grid variability of the information. However, the complexity of the topographic data may then be diminished (Westoby *et al.*, 2012). Equally, improvements of open-source software, such as CloudCompare and MeshLab, which can effortlessly analyse dense clouds will continue to help improve ease of access of structure from motion photogrammetry (Mallalieu *et al.*, 2017; Westoby *et al.*, 2012).

iii) Survey frequency

While this study has provided analysis of crevasse patterns and calving dynamics at a temporal resolution not seen before, it could be said that there are still issues in regards to the consistency of time between each survey was taken. Although there was a gap of approximately six hours between the surveys taken throughout the day (Figure 3.1), this doubled to at least twelve hours between the last survey of one day and the first of the next day. The collection of UAV photographs is obviously restricted by the availability of daylight. However, following the identification of surface crevasse propagation at night, it may have been advantageous to have attempted to reduce the amount of time between these surveys in order to better capture how crevasses evolve overnight.

Additionally, the majority of calving that took place over the course of the study period was between surveys 13_1 and 14_1. However, there is also the largest amount of time between these surveys, roughly 1 ½ days. Considering the importance of this period in the analysis it would have no doubt been advantageous to have had more repeated surveys over this day in order to better examine how the observed crevasses changed in the lead up to the three large calving events. Future researchers may therefore gain from keeping a consistent short interval between all surveys across the study period.

5.5 Priorities for Future Research

The outcomes of this study have additionally exposed other opportunities for future research that should be explored. These include:

i) Diurnal crevasse propagation

Interesting patterns emerged showing the diurnal development of a crevasse along Transect 4, with propagation occurring over night while the crevasse remained fairly stable throughout the day. However, it is unclear at the moment exactly why this occurs and how it relates to the diurnal pattern of meltwater production and ice velocity. Identification and detailed monitoring of such crevasses over their lifetime, and comparison to a high frequency record of meltwater flux and glacier velocity could provide an important insight into a process not properly recorded before.

ii) Influence of basal crevasses

Despite the high resolution DEMs produced through SfM, analysis is still only permitted at a surface level. However, it has been demonstrated that the subglacial topography and

development of basal crevasses can play a crucial role both in the occurrence of calving events as well as the pattern of surface crevasses. Although numerical models of basal conditions are useful for developing our understanding (e.g. Todd *et al.*, 2018), the importance of field data in such areas cannot be understated. Therefore, further surveys of Store Glacier using UAVs equipped with ground penetrating radar (GPR) could be a beneficial supplement to the surface data acquired here. Once technological advances allow for such a method to be affordable for regular research, this could provide an accurate way to examine the extent of basal crevasses (Luckman *et al.*, 2012) and allow the monitoring of how they impact on calving dynamics.

iii) Volume of ice lost

This study was able to analyse the area of ice lost between each of the ten surveys. However, additional work using the point clouds created through photogrammetry could have allowed the volume of ice lost to also be calculated. Although time restrictions did not permit this to be done in this study, further studies may profit from determining this and gaining a full 3D perspective of ice loss. This could prove particularly valuable due to the impact of basal conditions on calving and ice loss that has been identified here.

6. CONCLUSIONS

Using UAV-sourced photographs for SfM photogrammetry provides an accessible method for monitoring glaciers at a high resolution. Using frequent repeated UAV surveys to produce a series of DEMs and orthomosaics allows a 4D data set to be constructed that allows the examination of glacier dynamics over time. This includes the growth and propagation of crevasses along glacier fronts, plus their influence on the occurrence of varyingly sized calving events. This study used such an approach at Store Glacier, West Greenland, over the course of a five-day study period in July 2017.

In regards to the research objectives outlined at the start of this project, the crevasse maps generated here through Gaussian blurring show a clear progression over time and highlight the consistency of many crevasses over this short time period. From this aerial view, however, there is no strong connection between the pattern of crevasses and the occurrence of calving events along the front. Therefore, the analysis of 2D crevasse maps alone does not provide sufficient evidence to understand processes occurring at the calving front of glaciers. Rather the measurement of crevasse characteristics and dimensions is required to gain a full understanding of the dynamics at play.

This was seen during analysis of the second research question, as comparing the orientation of crevasses across a glacier front with the principal axis of strain can reveal additional information about the forces operating within the ice of a glacier. Due to this relation, Mode III splaying crevasses are dominant at the margins of Store Glacier (Regions A and E) forming through compressive flow, while Mode I transverse crevasses are found in the centre (Regions B and C) as a result of extensional forces in this higher velocity area. The main type of shear is also region dependant, with simple shear helping create the splaying crevasses in Regions A and E, whereas varying combinations of pure, as well as simple shear, are found in the central regions.

This is particularly the case for Region D, where a criss-cross pattern of crevasses is observed, showing that mixed mode fracturing is occurring. However, in addition to the patterns of strain and shear, this criss-cross configuration may also have connections to the subglacial overdeepening located beneath Store Glacier at this location, with basal crevasses potentially influencing the arrangement of crevasses observed on the glacier surface. Thus, further study of Store Glacier's bed topography may be needed first before a full understanding of crevasse orientation and pattern can be obtained.

Additionally, statistical analysis during investigations into research question three shows that the mass-measurement of crevasses along a calving front, even regionally, does not necessarily reveal any significant changes over time that can be used to explain the timing of calving events. On the other hand, the monitoring of individual crevasses, particularly using recurring depth profiles to examine their propagation through the ice, can help identify key areas where relationships between crevasse growth and calving events do occur. The expansion of a crevasse along Transect 4 has revealed a new insight, with a diurnal cycle of growth identified. The probable cause of this is to the time lag between peak daily meltwater/velocity and stress propagation through the ice. However, further research may be able to shed more light on why such a cycle exists.

Comparing the depth profiles with the crevasse maps has also exposed how the relationship between crevasses and calving is not a one-way connection. Instead, calving events can have an impact on the localised development of other crevasses, as seen along Transect 1 and 3. Here the debuttressing of the front following a calving event probably resulted in the speed-up of the nearby area and the spread of tensile stresses through the local ice, allowing crevasse and rift growth to occur. Thus, progression of our knowledge of crevassing and calving, and the implementation of this understanding into glacier models, will not come through explaining one principle before the other, but rather the advancement of both together.

Finally, the depth profiles have also shown that calving can occur without the propagation of surface crevasses through the glacier. This was witnessed along Transect 2, where no surface crevasses were observed to develop during the entire study period, despite the occurrence of CE2 between surveys 13_1 and 14_1. It is suggested that, due to the location of this calving event at the floating region of Store Glacier, basal crevasses instead propagated upwards and resulted in buoyancy-driven calving. Therefore, this once again demonstrates the importance of not only using surface-deep methods to analyse the crevasse-calving relationship, but for subglacial details and how the development of basal crevasses unfolds to also be taken into account.

In conclusion, the use of UAV remote sensing techniques and SfM software has allowed new and key details of the relationship between crevasse formation and the occurrence of calving events to be identified. In particular, the use of a sub-daily UAV surveys has shown the importance of understanding these processes on such a high temporal frequency. Further research should therefore be undertaken at this scale where possible, so that

crevassing and calving can be fully constrained in geographic models that aim to improve our understanding of their influence on rising sea levels and future climate change.

7. REFERENCES

Ahn, Y. and Box, J.E. (201) Glacier velocities from time-lapse photos: technique development and first results from the Extreme Ice Survey (EIS) in Greenland. *Journal of Glaciology*, 56(198): pp.723-734.

Åmark, M. (1980) Glacial flutes at Isfallsglaciären, Tarfala, Swedish Lapland. *Journal of the Geological Society of Sweden*, 102(3): pp.251-259.

Amundson, J.M.; Fahnestock, M.; Truffer, M.; Brown, J.; Lüthi, M.P. and Motyka, R.J. (2010) Ice mélange dynamics and implications for terminus stability, Jakobshavn Isbræ, Greenland. *Journal of Geophysical Research: Earth Surface*, 115(F1), 12pp.

Arnold, N. S.; Rees, W. G.; Devereux, B. J. and Amable, G. S. (2006) Evaluating the potential of high resolution airborne LiDAR data in glaciology. *International Journal of Remote Sensing*, 27(6): pp.1233-1251.

Ayala, A.; Pellicciotti, F.; MacDonell, S.; McPhee, J.; Vivero, S.; Campos, C. and Egli, P. (2016) Modelling the hydrological response of debris-free and debris-covered glaciers to present climatic conditions in the semiarid Andes of central Chile. *Hydrological Processes*, 30(22): pp.4036-4058.

Bartholomaus, T.C.; Anderson, R.S. and Anderson, S.P. (2007) Response of glacier basal motion to transient water storage. *Nature Geoscience*, 1(1): pp.33-37.

Bartholomew, I.; Nienow, P.; Mair, D.; Hubbard, A.; King, M.A. and Sole, A. (2010) Seasonal evolution of subglacial drainage and acceleration in a Greenland outlet glacier. *Nature Geoscience*, 3(6): pp.408-411.

Bassis, J.N. and Walker, C.C. (2012) Upper and lower limits on the stability of calving glaciers from the yield strength envelope of ice. *Proceedings of the Royal Society A: Mathematical, Physical and Engineering Sciences*, 468(2140): pp.913-931.

Benassi, F.; Dall'Asta, E.; Diorti, F.; Forlani, G.; Morra di Cella, U.; Roncella, R. and Santise, M. (2017) Testing accuracy and repeatability of UAV blocks oriented with GNSS-supported aerial triangulation. *Remote Sensing*, 9(2): 23pp.

Bendtsen, J.; Mortensen, J.; Lennert, K. and Rysgaard, S. (2015) Heat sources for glacial ice melt in a west Greenland tidewater outlet glacier fjord: the role of subglacial freshwater discharge. *Geophysical Research Letters*, 42(10): pp.4089-4095.

Benn, D.I. and Evans, D.J.A. (2010) *Glaciers and Glaciation*, 2nd edition. Abingdon, United Kingdom: Routledge, 816pp.

Benn, D.I.; Åström, J.; Zwinger, T.; Todd, J.; Nick, F.M.; Hulton, N.R.J. and Luckman, A. (2017b) Melt-undercutting and buoyancy-driven calving from tidewater glaciers: new insights from discrete element and continuum model simulations. *Journal of Glaciology*, 63(240): pp.691-702.

Benn, D.I.; Cowton, J.; Todd, J. and Luckman, A. (2017a) Glacier calving in Greenland. *Current Climate Change Reports*, 3(4): pp.282-290.

Benn, D.I.; Warren, C.R. and Mottram, R.H. (2007) Calving processes and the dynamics of calving glaciers. *Earth-Science Reviews*, 82(3-4): pp.143-179.

Benn, D.I.; Wiseman, S. and Hands, K. (2001) Growth and drainage of supraglacial lakes on the debris-mantled Ngozumpa Glacier, Khumbu Himal. *Journal of Glaciology*, 47(159): pp.626-638.

Bennett, M.R.; Hambrey, M.J.; Huddart, D. and Ghienne, J.F. (1996) The formation of a geometrical ridge network by the surge-type glacier Kongsvegen, Svalbard. *Journal of Quaternary Science*, 11(6): pp.437-449.

Berni, J.A.J.; Zarco-Tejada, P.J.; Suárez, L. and Fereres, E. (2009) Thermal and Narrowband Multispectral Remote Sensing for Vegetation Monitoring from an Unmanned Aerial Vehicle. *IEEE Transactions on Geoscience and Remote Sensing*, 47(3): pp.722-738.

Boufama, B.; Mohr, R. and Veillon, F. (1993) Euclidean constraints on uncalibrated reconstruction. *Proceedings of the Fourth International Conference on Computer Vision, Berlin, Germany*, pp.466-470.

Bhardwaj, A.; Joshi, P.K. and Snehmani, L.S. (2015) Remote sensing of alpine glaciers in visible and infrared wavelengths: A survey of advances and prospects. *Geocarto International*, 31(5): pp.557-574.

Bhardwaj, A.; Sam, L.; Akanksha, Martín-Torres, F.J. and Kumar, R. (2016) UAVs as remote sensing platform in glaciology: Present applications and future prospects. *Remote Sensing of Environment*, 175(1): pp.196-204.

Carr, J.R.; Vieli, A. and Stokes, C. (2013) Influence of sea ice decline, atmospheric warming, and glacier width on marine-terminating outlet glacier behaviour in northwest Greenland at

seasonal to interannual timescales. *Journal of Geophysical Research: Earth Surface*, 118(3): pp.1210-1226.

Castillo, C.; James, M. R.; Redel-Macías, M. D.; Pérez, R. and Gómez, J. A. (2015) SF3M software: 3-D photo-reconstruction for nonexpert users and its application to a gully network. *SOIL*, 1(2): pp.583-594.

Cathles, M.; Abbot, D.; Bassis, J. and MacAyeal, D. (2011) Modelling surface-roughness/solar-ablation feedback: Application to small-scale surface channels and crevasses of the Greenland ice sheet. *Annals of Glaciology*, 52(59); pp.99-108.

Chandler, J.H. (1999) Effective application of automated digital photogrammetry for geomorphological research. *Earth Surface Processes and Landforms*, 24(1): pp.51-63.

Chandler, J.H.; Fryer, J.G. and Jack, A. (2005) Metric capabilities of low cost digital cameras for close range surface measurement. *The Photogrammetric Record*, 20(109): pp.12-26.

Chauché, N. (2016) *Glacier-Ocean interaction at Store Glacier (West Greenland)*. Doctoral thesis, Aberystwyth University: 226pp.

Chauché, N.; Hubbard, A.; Gascard, J.C.; Box, J.E.; Bates, R.; Koppes, M.; Sole, A.; Christoffersen, P. and Patton, H. (2014) Ice-ocean interaction and calving front morphology at two west Greenland tidewater outlet glaciers. *The Cryosphere*, 8(): pp.1457-1468.

Christoffersen, P.; Mugford, R.I.; Heywood, K.J.; Joughin, I.; Dowdeswell, J.A.; Syvitski, J.P.M.; Luckman, A. and Benham, T.J. (2011) Warming of waters in an East Greenland fjord prior to glacier retreat: mechanisms and connection to large-scale atmospheric conditions. *The Cryosphere*, 5(3): pp.701-714.

Chudley, T.; Christoffersen, P.; Abellan, A.; Doyle, S. and Snooke, N (2018) Reducing GCP dependency in UAV Structure from Motion photogrammetry using differential carrier-phase GPS: applications for studying Greenland Ice Sheet dynamics. *EGU General Assembly Conference Abstracts*, vol. 20, no. EGU2018-638.

Colgan, W.; Rajaram, H.; Abdalati, W.; McCutchan, C.; Mottram, R.; Moussavi, M.S. and Grigsby, S. (2016) Glacier crevasses: Observations, models, and mass balance implications. *Reviews of Geophysics*, 54(1): pp.119-161.

Colgan, W.; Steffen, K.; McLamb, W.; Abdalati, W.; Rajaram, H.; Motyka, R.; Phillips, T. and Anderson, R. (2011) An increase in crevasse extent, West Greenland: Hydrologic implications. *Geophysical Research Letters*, 38(18): 7pp.

Cook, J. (1956) Some observations in a Northwest Greenland Crevasse. *Transactions, American Geophysical Union*, 37(6): pp.715-718.

Cook, S.; Zwinger, T.; Rutt, I.C.; O'Neel, S. and Murray, T. (2012) Testing the effect of water in crevasses on a physically based calving model. *Annals of Glaciology*, 53(60): pp.90-96.

Cook, S.; Rutt, I.C.; Murray, T.; Luckman, A.; Zwinger, T.; Selmes, N. and James, T. D. (2014) Modelling environmental influences on calving at Helheim Glacier in eastern Greenland. *The Cryosphere*, 8(3): pp.827-841.

Corripio, J. G. (2004) Snow surface albedo estimation using terrestrial photography. *International Journal of Remote Sensing*, 25(24): pp.5705-5729.

Crocker, R.I.; Maslanik, J.A.; Adler, J.J.; Palo, S.E.; Herzfeld, U.C. and Emery, W.J. (2012) A Sensor Package for Ice Surface Observations Using Small Unmanned Aircraft Systems. *IEEE Transactions on Geoscience and Remote Sensing*. 50(4): pp.1033-1047.

Crocker, R.I.; Maslanik, J.A.; Palo, S.E.; Fowler, C.; Adler, J.; Herzfeld, U.C.; Fladeland, M.M.; Weatherhead, E.C. and Angier, M. (2009) Performance assessment of a small LIDAR altimeter deployed on unmanned aircraft for glacier and sea ice surface topography profiling. *Proceedings of the AGU Fall Meeting 2009*, Abstract No.C33C-0511.

Curry, J.; Maslanik, J.; Holland, G. and Pinto, J. (2004) Applications of aerosondes in the Arctic. *Bulletin of the American Meteorological Society*, 85(12), pp.1855-1861.

Dall'Asta, E.; Delaloye, R.; Diotri, F.; Forlani, G.; Fornari, Morro di Cella, U. M.; Pogliotti, P.; Roncella, R. and Santise, M. (2015) Use of UAS in a High Mountain Landscape: the Case of Gran Sommetta Rock Glacier (AO). *ISPRS – International Archives of the Photogrammetry, Remote Sensing and Spatial Information Sciences*, XL-3(W3), pp.391-397.

Danielson, B. and Sharp, M. (2013) Development and application of a time-lapse photograph analysis method to investigate the link between tidewater glacier flow variations and supraglacial lake drainage events. *Journal of Glaciology*, 59(214): pp.287-302.

d'Oleire-Oltmanns, S.; Marzolff, I.; Peter, K.D. and Ries, J.B. (2012) Unmannedaerial vehicle (UAV) for monitoring soil erosion in Morocco. *Remote Sensing*, 4(11): pp.3390-3416.

Donner, J. and Jungner, H. (1975) Radiocarbon dating of shells from marine Holocene deposits in the Disko Bugt area, West Greenland. *Boreas*, 4(1), pp.25-45.

Doyle, F. (1964) The Historical Development of Analytical Photogrammetry. *Photogrammetric Engineering*, 15: pp.259-265.

Doyle, S.H.; Hubbard, B.; Christoffersen, P.; Young, T.J.; Hofstede, C.; Bougamont, M.; Box, J.E. and Hubbard, A. (2018) Physical conditions of fast glacier flow: 1. Measurements from boreholes drilled to the bed of Store Glacier, West Greenland. *Journal of Geophysical Research: Earth Surface*, 123(2): pp.324-348.

Dumont, M.; Sirguey, P.; Arnaud, Y. and Six, D. (2011) Monitoring spatial and temporal variations of surface albedo on Saint Sorlin Glacier (French Alps) using terrestrial photography. *The Cryosphere*, 5(3): pp.759-771.

Echelmeyer, K.; Clarke, T.S. and Harrison, W.D. (1991) Surficial glaciology of Jakobshavns Isbræ, West Greenland: Part I. Surface morphology. *Journal of Glaciology*, 37(127): pp.368-382.

Edwards, M.W.M. (2008) *Comprehensive error analysis and integration of an airborne laser profiling system for Arctic sea ice freeboard measurements*. M.S. thesis, University of Colorado Boulder.

Eklund, A. and Hart, J.K. (1996) Glaciotectonic deformation within a flute from the Isfallsglaciären, Sweden. *Journal of Quaternary Science*, 11(4): pp.299-310.

Eltner, A. and Schneider, D. (2015) Analysis of Different Methods for 3-D Reconstruction of Natural Surfaces from Parallel-Axes UAV Images. *The Photogrammetric Record*, 30(151): pp.279-299.

Eltner, A.; Kaiser, A.; Castillo, C.; Rock, G.; Neugirg, F. and Abellán, A. (2016) Image-based surface reconstruction in geomorphometry – merits, limits and developments. *Earth Surface Dynamics*, 4(2): pp.359-389.

Ely, J.C.; Graham, C.; Barr, I.D.; Rea, B.R.; Spagnolo, M. and Evans, J. (2017) Using UAV acquired photography and structure from motion techniques for studying glacier landforms: application to the glacial flutes at Isfallsglaciären. *Earth Surface Processes and Landforms*, 42(6): pp.877-888.

Enderlin, E.M.; Howat, I.M.; Jeong, S.; Noh, M.-J.; van Angelen, J.H. and van den Broeke, M.R. (2014) An improved mass budget for the Greenland ice sheet. *Geophysical Research Letters*, 41(3): pp.866-872.

Evans, J.; Ó Cofaigh, C.; Dowdeswell, J.A. and Wadhams, P. (2009) Marine geophysical evidence for former expansion and flow of the Greenland Ice Sheet across the north-east Greenland continental shelf. *Journal of Quaternary Science*, 24(3): pp.279-293.

Favier, L.; Durrand, G.; Cornford, S.L.; Gudmundsson, G.H.; Gagliardini, O.; Gillet-Chaulet, F.; Zwinger, T.; Payne, A.J. and Le Brocq, A.M. (2014) Retreat of Pine Island Glacier controlled by marine ice-sheet instability. *Nature Climate Change*, 4(2): pp.117-121.

Fettweis, X.; Franco, B.; Tedesco, M.l van Angelen, J. H.; Lenaerts, J. T. M.; van den Broeke, M. R. and Gallée, H. (2013) Estimating the Greenland ice sheet surface mass balance contribution to future sea level rise using the regional atmospheric climate model MAR. *The Cryosphere*, 7(2): pp.469-489.

Förstner, W. (1986) A feature-based correspondence algorithm for image matching. *International Archives of Photogrammetry and Remote Sensing*, 26(3): pp.150-166.

Fraser, C.S. and Cronk, S. (2009) A hybrid measurement approach for close-range photogrammetry. *ISPRS Journal of Photogrammetry and Remote Sensing*, 64(3): pp.328-333.

Funder, S. and Hansen, L. (1996) the Greenland ice sheet – a model for its culmination and decay during and after the last glacial maximum. *Bulletin of the Geological Society of Denmark*, 42(2): pp.137-152.

Gordon, J.E.; Whalley, W.B.; Gellatly, A.F. and Vere, D.M. (1992) The formation of glacial flutes: assessment of models with evidence from Lyngsdalen, North Norway. *Quaternary Science Reviews*, 11(7): pp.709-731.

Gardner, A. S. and Sharp, M. J. (2010) A review of snow and ice albedo and the development of a new physically based broadband albedo parameterization. *Journal of Geophysical Research: Earth Surface*, 115(F1): pp.1-15.

Garvelmann, J.; Pohl, S. and Weiler, M. (2013) From observation to the quantification of snow processes with a time-lapse camera network. *Hydrology and Earth System Sciences*, 17(4): pp.1415–1429.

Gindraux, S.; Boesch, R. and Farinotti, D. (2017) Accuracy Assessment of Digital Surface Models from Unmanned Aerial Vehicles' Imagery on Glaciers. *Remote Sensing*, 9(2): 15pp.

Glasser, N. and Scambos, T. (2008) A structural glaciological analysis of the 2002 Larsen B Ice-Shelf collapse. *Journal of Glaciology*, 54(1): pp.3-16.

Glasser, N.; Kulessa, B.; Luckman, A.; Jansen, D.; King, E.; Sammonds, P.; Scambos, T. and Jezek, K. (2009) Surface structure and stability of the Larsen C ice shelf, Antarctic peninsula. *Journal of Glaciology*, 55(191): pp.400-410.

Glen, J. (1955) The creep of polycrystalline ice. *Proceedings of the Royal Society A: Mathematical, Physical and Engineering Sciences*, 228(1175): pp.519-538.

Håkansson, L.; Alexanderson, H.; Hjort, C.; Möller, P.; Briner, J.P.; Aldhan, A. and Possnert, G. (2008) Late Pleistocene glacial histroy of Jameson Land, central East Greenland, derived from cosmogenic 10Be and 26Al exposure dating. *Boreas*, 38(2): pp.244-260.

Hambrey, M.J. (1975) The origin of foliation in glaciers: evidence from some Norwegian examples. *Journal of Glaciology*, 14(70): pp.181-185.

Hambrey, M.J. (1976) Structure of the glacier Charles Rabots Bre, Norway. *Geological Society of America Bulletin*, 87(11): pp.1629-1637.

Hambrey, M.J. (1994) *Glacial Environments*. London: UCL Press, 302pp.

Hambrey, M.J. and Lawson, W.J. (2000) "Structural styles and deformation fields in glaciers: a review" in Maltman, A.J., Hubbard, B. and Hambrey, M.J. (eds.) *Deformation of Glacial Materials,* The Geological Society of London Special Publication 176: pp.59-83.

Hanna, E. (2005) Runoff and mass balance of the Greenland ice sheet: 1958–2003. *Journal of Geophysical Research: Atmospheres*, 110(D13): 16pp.

Hanna, E.; Cappelen, J.; Fettweis, X.; Huybrechts, P.; Luckman, A. and Ribergaard, M. (2009) Hydrologic response of the Greenland ice sheet: The role of oceanographic warming. *Hydrological Processes*, 23(1): pp.7-30.

Hanson, B. and Hooke, R.L. (2000) Glacier calving: A numerical model of forces in the calving-speed/water-depth relation. *Journal of Glaciology*, 46(153): pp.188-196.

Haresign, E.C. and Warren, C.R. (2005) "Melt rates at calving termini: A study at Glacier Leon, Chilean Patagonia" in Harris, C. and Murton, J.B. (eds.) *Cryospheric Systems: Glaciers and Permafrost*, The Geological Society of London Special Publication 242: pp.99-110.

Harper, J.T.; Humphrey, N.F. and Pfeffer, W.T. (1998) Crevasse patterns and the strain-rate tensor: a high-resolution comparison. *Journal of Glaciology*, 44(146): pp.68-76.

Harris, C. and Stephens, M. (1988) A combined corner and edge detector. *Proceedings of the Fourth Alvey Vision Conference, Manchester*, pp.147-151.

Hart, J.K. (1995) Subglacial erosion, deposition and deformation associated with deformable beds. *Progress in Physical Geography*, 19(2): pp.173-191.

Hodson, A.; Anesio, A.M.; Ng, F.; Watson, R.; Quirk, J.; Irvine-Fynn, T.; Dye, A.; Clark, C.; McCloy, P.; Kohler, J. and Sattler, B. (2007) A glacier respires: Quantifying the distribution and respiration CO2 flux of cryoconite across an entire Arctic supraglacial ecosystem. *Journal of Geophysical Research: Biogeosciences*, 112, G04S36, doi:10.1029/2007JG000452, 9pp.

Hofton, M.; Malavassi, E. and Blair, J. (2006) Quantifying recent pyroclastic and lava flows at Arenal Volcano, Costa Rica, using medium-footprint lidar. *Geophysical Research Letters*, 33(21): L21306, doi:10.1029/2006GL027822, 5pp.

Holdsworth, G. (1969) Primary transverse crevasses. Journal of Glaciology, 8(52): pp.107-129.

Holland, D.M.; Thomas, R.H.; de Young, B.; Ribergaard, M.H. and Lyberth, B. (2008) Acceleration of Jakobshavn Isbrae triggered by warm subsurface ocean waters. *Nature Geoscience*, 1(10): pp.659-664.

Hooke, R. (1989) Englacial and subglacial hydrology: A qualitative review. *Arctic and Alpine Research*, 21(3): pp.221-233.

Hoppe, G. and Schytt, V. (1953) Some observations on fluted moraine surfaces. *Geografiska Annaler*, 35(2): pp.105-115.

Howat, I.M.; Box, J.E.; Ahn, Y.; Herrington, A. and McFadden, E.M. (2010) Seasonal variability in the dynamics of marine-terminating outlet glaciers in Greenland. *Journal of Glaciology*, 56(198): pp.601-613.

Howat, I.; Joughin, I.; and Scambos, T. (2007) Rapid changes in ice discharge from Greenland outlet glaciers. *Science*, 315(5818): pp.1559-1561.

Howat, I.; Joughin, I.; Tulaczyk, S. and Gogineni, S. (2005) Rapid retreat and acceleration of Helheim Glacier, east Greenland, *Geophysical Research Letters*, 32(22): 4pp.

Hubbard, A.; Ryan, J.; Toberg, N.; Todd, J.; Christoffersen, P.; Snooke, N. and Box, J.E. (2015) Tidewater dynamics at Store Glacier, West Greenland from daily repeat UAV survey. *AGU Fall Meeting Abstracts 2015AGUFM.C33G.03H*.

Hugenholtz, C.H.; Moorman, B.J.; Riddell, K. and Whitehead, K. (2012) Small unmanned aircraft systems for remote sensing and earth science research. *Eos, Transactions American Geophysical Union*, 93(25): p.236.

Hugenholtz, C.H.; Whitehead, K.; Barchyn, T.E.; Brown, O.W.; Moorman, B.J.; LeClair, A.; Hamilton, T. and Riddell, K. (2013) Geomorphological mapping with a small unmanned aircraft system (sUAS): Feature detection and accuracy assessment of a photogrammetrically-derived digital terrain model. *Geomorphology* 194(1): pp.16-24.

Iken, A. (1977) Movement of a large ice mass before breaking off. *Journal of Glaciology*, 19(81): pp.595-605.

Immerzeel, W.; Kraaijenbrink, P. and Andreassen, L. (2017) Use of an Unmanned Aerial Vehicle to assess recent surface elevation change of Storbreen in Norway. *The Cryosphere*, unpublished manuscript, doi:10.5194/tc-2016-292, 31pp.

Immerzeel, W.W.; Kraaijenbrink, P.D.A.; Shea, J.M.; Shrestha, A.B.; Pellicciotti, F.; Bierkens, M.F.P. and de Jong, S.M. (2014) High-resolution monitoring of Himalayan glacier dynamics using unmanned aerial vehicles. *Remote Sensing of Environment*, 150(1): pp.93-103.

Inall, M.E.; Murray, T.; Cottier, F.R.; Scharrer, K.; Boyd, T.J.; Heywood, K.J. and Bevan, S.L. (2014) Oceanic heat delivery via Kangerdlugssuaq Fjord to the south-east Greenland ice sheet. *Journal of Geophysical Research: Oceans*, 119(2): pp.631-645.

Irvine-Fynn, T.; Hodson, A.; Moorman, B.; Vatne, G. and Hubbard, A. (2011) Polythermal glacier hydrology: A review. Reviews of Geophysics, 49(4): 37pp.

Jackson, R.H. and Straneo F. (2016) Heat, salt, and freshwater budgets for a glacial fjord in Greenland. *Journal of Physical Oceanography*, 46(9): pp.2735-2768.

James, M.R. and Robson, S. (2012) Straightforward reconstruction of 3D surfaces and topography with a camera: Accuracy and geoscience application. *Journal of Geophysical Research: Earth Surface*, 117(F3), F03017, doi:10.1029/2011JF002289, 17pp.

James, M.R. and Robson, S. (2014) Mitigating systematic error in topographic models derived from UAV and ground-based image networks. *Earth Surface Processes and Landforms*, 39(10): pp,1413-1420.

James, M.R.; Robson, S. and Smith, M.W. (2017) 3-D uncertainty-based topographic change detection with structure-from-motion photogrammetry: precision maps for ground control and directly georeferenced surveys. *Earth Surface Processes and Landforms*, 42(12): pp.1769-1788.

James, T.D.; Murray, T.; Selmes, N.; Scharrer, K. and O'Leary, M. (2014) Buoyant flexure and basal crevassing in dynamic mass loss at Helheim Glacier. *Nature Geoscience*, 7(8): pp.593-596.

Joughin, I.; Das, S.B.; King, M.A.; Smith, B.E.; Howat, I.M. and Moon, T. (2008b) Seasonal speedup along the western flank of the Greenland Ice Sheet. *Science*, 320(5877): pp.781-783.

Joughin, I.; Howat, I.; Alley, R.B.; Eksrom, G.; Fahnestock, M.; Moon, T.; Nettles, M.; Truffer, M.; Tsai, V.C. (2008a) Ice-front variation and tidewater behavior on Helheim and Kangerdlugssuaq Glaciers, Greenland. *Journal of Geophysical Research: Earth Surface*, 113(F1), 11pp.

Joughin, I.; Smith, B.E.; Howat, I.M.; Floricioiu, D.; Alley, R.B.; Truffer, M. and Fahnestock, M. (2012) Seasonal to decadal scale variations in the surface velocity of Jakobshavn Isbrae, Greenland: Observation and model-based analysis. Journal of Geophysical Research, 117 (F2): 20pp.

Joughin, I.; Smith, B.; Howat, I.; Scambos, T. and Moon, T. (2010) Greenland flow variability from ice-sheet-wide velocity mapping. *Journal of Glaciology*, 56(197): pp.415-430.

Joughin, I.; Smith, B.E. and Medley, B. (2014b) Marine ice sheet collapse potentially under way for the Thwaites Glacier basin, West Antarctica. *Science*, 344(6185): pp.735-738.

Joughin, I.; Smith, B.E.; Shean, D.E. and Floricioiu, D. (2014a) Brief Communication: Further summer speedup of Jakobshavn Isbræ. *The Cryosphere*, 8(1): pp.209-214.

Jouvet, G.; Weidmann, Y.; Seguinot, J.; Funk, M.; Abe, T.; Sakakibara, D.; Seddik, H. and Sugiyama, S. (2017) Initiation of a major calving event on the Bowdoin Glacier captured by UAV photogrammetry. *The Cryoshpere*, 11(2): pp.911-921.

Kääb, A.; Girod, L. and Berthling, I. (2014) Surface kinematics of periglacial sorted circles using Structure-from-Motion technology. *The Cryosphere*, 8(3): pp.1041-1056.

Kaser, G.; Hardy, D.R.; Mölg, T.; Bradley, R.S. and Hyera, T.M. (2004) Modern glacier retreat on Kilimanjaro as evidence of climate change: observations and facts. *International Journal of Climatology*, 24(3): pp.329-339.

Katoh, N.; Nakabayashi, K.; Ito, M. and Ohno, S. (1998) Effect of ambient light on the color appearance of softcopy images: Mixed chromatic adaptation for self-luminous displays. *Journal of Electronic Imaging*, 7(4): pp.794-806.

Keutterling, A. and Thomas, A. (2006) Monitoring glacier elevation and volume changes with digital photogrammetry and GIS at Gepatschferner glacier, Austria. *International Journal of Remote Sensing*, 27(19): pp.4371-4380.

Khan, S.A.; Wahr, J.; Bevis, M.; Velicogna, I. and Kendrick, E. (2010) Spread of ice mass loss into northwest Greenland observed by GRACE and GPS. *Geophysical Research Letters*, 37(6): 5pp.

Kjær, K.H.; Larsen, E.; van der Meer, J.; Ingólfsson, Ó.; Krüger, J.; Benediktsson, Í.Ö.; Knudsen, C.G. and Schomacker, A. (2006) Subglacial decoupling at the sediment/bedrock interface: a new mechanism for rapid flowing ice. *Quaternary Science Reviews*, 25(21): pp.2704-2712.

Kraaijenbrink, P.D.A.; Shea, J.M.; Pellicciotti, F.; de Jong, S.M. and Immerzeel, W.W. (2016) Object-based analysis of unmanned aerial vehicle imagery to map and characterise surface features on a debris-covered glacier. *Remote Sensing of Environment*, 186(1): pp.581-595.

Krabill, W.; Abdalati, W.; Frederick, E.; Manizade, S.; Martin, C.; Sonntag, J.; Swift, R.; Thomas, R. and Yungel, J. (2002) Aircraft laser altimetry measurement of elevation changes of the Greenland ice sheet: Technique and accuracy assessment. *Journal of Geodynamics*, 34(3-4): pp.357-376.

Kraus, K. (2007) *Photogrammetry: Geometry from Images and Laser Scans*, 2nd edition. Berlin: De Gruyter, 459pp.

Krug, J.; Weiss, J.; Gagliardini, O. and Durand, G. (2014) Combining damage and fracture mechanics to model calving. *The Cryosphere*, 8(6): pp.2101-2117.

Lane, S.N.; James, T.D. and Crowell, M.D. (2000) Application of digital photogrammetry to complex topography for geomorphological research. *The Photogrammetric Record*, 16(95): pp.793-821.

Laussedat, A. (1899) *La métrophotographie*. Paris: Gauthier-Villars, 55pp.

Long, A.J. and Roberts, D.H. (2002) A revised chronology for the 'Fjord Stafe' moraine in Disko Bugt, west Greenland. *Journal of Quaternary Science*, 17(5-6): pp.561-579.

Lowe, D. G. (1999) Object recognition from local scale-invariant features. *The Proceedings of the 7th IEEE International Conference on Computer Vision, Kerkyra, Greece*, 2: pp.1150-1157.

Luckman, A. and Murray, T. (2005) Seasonal variation in velocity before retreat of Jakobshavn Isbræ, Greenland. *Geophysical Research Letters*, 32(8): 4pp.

Luckman, A.; Benn, D.I.; Cottier, F.; Bevan, S.; Nilsen, F.; Inall, M. (2015) Calving rates at tidewater glaciers vary strongly with ocean temperature. *Nature Communications*, 6(1): p.8566.

Luckman, A.; Jansen, D.; Kulessa, B.; King, E.C.; Sammonds, P. and Benn, D.I. (2012) Basal crevasses in Larsen C Ice Shelf and implications for their global abundance. *The Cryoshpere*, 6(1): pp.113-123.

Luhmann, T.; Robson, S.; Kyle, S. and Boehm, J. (2014) *Close-Range Photogrammetry and 3-D Imaging*, 2nd edition. Berlin: De Gruyter, 683pp.

Ma, Y.; Tripathy, C.S. and Bassis, J.N. (2017) Bounds on the calving cliff height of marine terminating glaciers. *Geophysical Research Letters*, 44(3): pp.1369-1375.

MacArthur, A.; Robinson, I.; Rossini, M.; Davis, N. and MacDonald, K. (2014) A dual-field-of-view spectrometer system for reflectance and fluorescence measurements (piccolo doppio) and correction of etaloning. *Proceedings of the Fifth International Workshop on Remote Sensing of Vegetation Fluorescence, (Paris)*: pp.22-24.

Mallalieu, J.; Carrvick, J.L.; Quincey, D.J.; Smith, M.W. and James, W.H.M. (2017) An integrated Structure-from-Motion and time-lapse technique for quantifying ice-margin dynamics. *Journal of Glaciology*, 63(242): pp.937-949.

Matsuoka, N. and Murton, J. (2008) Frost weathering: Recent advances and future discussions. *Permafrost and Periglacial Processes*, 19(2): pp.195-210.

Matthews, N.A. (2008) Aerial and close-range photogrammetric technology: providing resource documentation, interpretation, and preservation. *Technical Note 428*, Bureau of Land Management, Denver, Colorado, 42pp.

Mark, B.G.; Bury, J.; McKenzie, J.M.; French, A. and Baraer, M. (2010) Climate change and tropical Andean glacier recession: Evaluating hydrologic changes and livelihood vulnerability in the Cordillera Blanca, Peru. *Annals of the Association of American* Geographers, 100(4): pp.794-805.

McGrath, D.; Steffen, K.; Scambos, T.; Rajaram, H.; Casassa, G. and Lagos, J.L.R. (2012) Basal crevasses and associated surface crevassing on the Larsen C ice shelf, Antarctica, and their role in ice-shelf instability. *Annals of Glaciology*, 53(60): pp.10-18.

Meier, M. (1958) The mechanics of crevasse formation. *International Association of Scientific Hydrology Publication 46* (General Assembly of Toronto 1957 – Snow and Ice), pp.500-508.

Meier, M. (1960) Mode of flow of Saskatchewan Glacier, Alberta, Canada. *U.S. Geological Survey Professional Paper*, 351: 68pp.

Meier, M.; Conel, J.; Hoerni, J.; Melbourne, W.; Pings, C. and Walker, P. (1957) Preliminary study of crevasse formation: Blue Ice Valley, Greenland, 1955. *U.S. Army Snow, Ice and Permafrost Research Establishment, Report 38*.

Medrzycka, D.; Benn, D.I.; Box, J.E.; Copland, L. and Balog, J. (2016) Calving behaviour at Rink Isbræ, West Greenland, from time-lapse photos. *Arctic, Antarctic and Alpine Research*, 48(2): pp.263-277.

Meunier-Cardinal, G.; Demuth, M.N. and Kinnard, C. (2016) Using UAV photogrammetry to study topographic change: application to Saskatchewan Glacier, Alberta, Canada. *American Geophysical Union Fall General Assembly 2016*, abstract #C41C-0680.

Mikhail, E.; Bethel, J. and McGlone, J. (2001) *Introduction to Modern Photogrammetry*. New York, USA: John Wiley and Sons, Inc., 479pp.

Moon, T.; Joughin, I. and Smith, B. (2015) Seasonal to multiyear variability of glacier surface velocity, terminus position, and sea ice/ice mélange in northwest Greenland. *Journal of Geophysical Research: Earth Surface*, 120(5): pp.818-833

Morlighem, M.; Bondzio, J.; Seroussi, H.; Rignot, E.; Larour, E.; Humbert, A. and Rebuffi, S. (2016) Modelling of store Gletscher's calving dynamics, West Greenland, in response to ocean thermal forcing. *Geophysical Research Letters*, 43(6): pp.2659-2666.

Morlighem, M.; Rignot, E.; Mouginot, J.; Seroussi, H. and Larour, E. (2014) High-resolution ice thickness mapping in South Greenland, *Annals of Glaciology*. 55(67): pp.64-70.

Mottram, R.H. and Benn, D.I. (2009) Testing crevasse depth models: a field study at Breioamerkurjokull, Iceland. *Journal of Glaciology*, 55(192): pp.746-752.

Motyka, R.J.; Hunter, L.; Echelmeyer, K. and Connor, C. (2003) Submarine melting at the terminus of a temperate tidewater glacier, LeConte Glacier, Alaska, U.S.A. *Annals of Glaciology*, 36(1): pp.57-65.

Münchow, A.; Padman, L.; Fricker, H.A. (2014) Interannual changes of the floating ice shelf of Petermann Gletscher, North Greenland, from 2000 to 2012. *Journal of Glaciology*, 60(221): pp.489-499.

Murray, T.; Scharrer, K.; James, T.D.; Dye, S.R.; Hanna, E.; Booth, A.D.; Selmes, N.; Luckman, A.; Hughes, A.L.C.; Cook, S. and Huybrechts, P. (2010), Ocean regulation hypothesis for glacier dynamics in southeast Greenland and implications for ice sheet mass changes. *Journal of Geophysical Research: Atmospheres*, 115(F3): 15pp.

Murray, T.; Scharrer, K.; Selmes, N.; Booth, A.D.; James, T.D.; Bevan, S.L.; Bradley, J.; Cook, S.; Cordero Llana, L.; Drocourt, Y.; Dyke, L; Goldsack, A.; Hughes, A.L.; Luckman, A.J. and McGovern, J. (2015b) Extensive retreat of Greenland tidewater glaciers, 2000–2010. *Arctic, Antarctic and Alpine Research*, 47(3): pp.427-447.

Murray, T.; Selmes, N.; James, T.; Edwards, S.; Martin, I.; O'Farrell, T.; Aspey, R.; Rutt, I.; Nettles, M. and Baugé, T. (2015a) Dynamics of glacier calving at the ungrounded margin of Helheim Glacier, southeast Greenland. *Journal of Geophysical Research: Earth Surface*, 120(6): pp.964-982.

Nick, F.M.; Luckman, A.; Vieli, A.; van der Venn, C.J.; van As, D.; van de Wal, RS.W.; Pattyn, F.; Hubbard, A.L. and Floricioiu, D. (2012) The response of Petermann Glacier, Greenland, to large calving events, and its future stability in the context of atmospheric and oceanic warming. *Journal of Glaciology*, 58(208): pp.229-239.

Nick, F.M.; van der Veen, C.J.; Vieli, A. and Benn, D.I. (2010) A physically based calving model applied to marine outlet glaciers and implications for the glacier dynamics. *Journal of Glaciology*, 56(199): pp.781-794.

Noël, B.; van de Berg, W.; van Meijgaard, E.; Munneke, P.K.; van de Wal, R. and van den Broeke, M. (2015) Evaluation of the updated regional climate model RACMO2. 3: summer snowfall impact on the Greenland Ice Sheet. *The Cryosphere*, 9(5): pp.1831-1844.

Nye, J.F. (1952) The mechanics of glacier flow. *Journal of Glaciology*, 2(12): pp.82-93.

Nye, J.F. (1957) The distribution of stress and velocity in glaciers and ice sheets. *Proceedings of the Royal Society A: Mathematical, Physical and Engineering Sciences*, 239(1216): pp.113-133.

Ó Cofaigh, C.; Dowdeswell, J.A.; Evans, J.; Kenyon, N.H.; Taylor, J.; Mienert, J. and Wilken, M. (2004) Timing and significance of glacially influences mass-wasting in the submarine channels of the Greenand Basin. *Marine Geology*, 207(1-4): pp.39-54.

Ó Cofaigh, C.; Dowdeswell, J.A.; Jennings, A.E.; Hogan, K.A.; Kilfeather, A.; Hienstra, J.E.; Noormets, R.; Evans, J.; Mc Carthy, D.J.; Andrews, J.T.; Lloyd, J.M. and Moros, M. (2013) An extensive and dynamic ice sheet on the West Greenland shelf during the last glacial cycle. *Geology*, 41(2): pp.219-222.

O'Leary, M. and Christoffersen, P. (2013) Calving on tidewater glaciers amplified by submarine frontal melting. *The Cryosphere*, 7(1): p.119.

O'Neel, S.; Echelmeyer, K.A. and Motyka, R.J. (2003) Short-term variations in calving of a tidewater glacier: LeConte Glacier, Alaska, U.S.A. *Journal of Glaciology*, 49(167): pp.587-598.

Paterson, W.S.B. (1994) *The Physics of Glaciers*, 3rd edition. Oxford: Pergamon, 704pp.

Patterson, M. and Brescia, A. (2008) Integrated sensor systems for UAS. *Proceedings of the 23rd Bristol International Unmanned Air Vehicle Systems Conference*, 1(4): pp.476-527.

Patterson, M.C.L. and Morris, J. (2009) Small UAS imaging capabilities. *Proceedings of the 24th Bristol International Unmanned Air Vehicle Systems Conference*, 2(5): pp.798-829.

Petlicki, M.; Cieply, M.; Jania, J.A.; Prominska, A. and Kinnard, C. (2015) Calving of a tidewater glacier driven by melting at the waterline. *Journal of Glaciology*, 61(229): pp.851-863.

Pierrot-Deseilligny, M. and Clery, I. (2011) APERO, an open source bundle adjustment software for automatic calibration and orientation of set of images. *International Archives for Photogrammetry and Remote Sensing*, XXXVIII-5(W16), pp.269-276.

Pollard, D.; DeConto, R.M. and Alley, R.B. (2015) Potential Antarctic ice sheet retreat driven by hydrofracturing and ice cliff failure. *Earth and Planetary Science Letters*, 412(1): pp.112-121.

Pritchard, H.D.; Arthern, R.J.; Vaughan, D.G. and Edwards, L.A. (2009) Extensive dynamic thinning on the margins of the Greenland and Antarctic ice sheets. *Nature*, 461(7266): pp.971-975.

Przybilla, H. and Wester-Ebbinghaus, W. (1979) Bildflug mit ferngelenktem Kleinflugzeug. *Bildmessung und Luftbildwessen*, 47(5): pp.137-142.

Quincey, D. J. and Luckman, A. (2009) Progress in satellite remote sensing of ice sheets, *Progress in Physical Geography*, 33(4): pp.547-567.

Raymond, C.F. (1971) Flow in a transverse section of the Athabasca Glacier, Alberta, Canada. *Journal of Glaciology*, 10(58): pp.55-84.

Rea, B.R. and Evans, D.J. (2011) An assessment of surge-induced crevassing and the formation of crevasse squeeze ridges. *Journal of Geophysical Research: Earth Surface*, 116(F4), F04005, doi:10.1029/2011JF001970, 17pp.

Reeh, N. (1985) Was the Greenland ice sheet thinner in the late Wisconsinan than now? *Nature*, 317(6040): pp.797-799.

Remondino, F. and Fraser, C. (2006) Digital camera calibration methods: Considerations and comparisons. *The International Archives of the Photogrammetry and Remote Sensing Commission V Symposium 'Image Engineering and Vision Metrology'*, IAPRS Vol XXXVI, pp.266-272.

Rignot, E. and Kanagaratnam, P. (2006) Changes in the velocity structure of the Greenland ice sheet. *Science*, 311(5763): pp.986-990.

Rignot, E. and Mouginot, J. (2012) Ice flow in Greenland for the International Polar Year 2008–2009. *Geophysical Research Letters*, 39(11): 7pp.

Rignot, E.; Fenty, I.; Xu, Y.; Cai, C. and Kemp, C. (2015) Undercutting of marine-terminating glaciers in West Greenland. *Geophysical Research Letters*, 42(14): pp.5909-5917.

Rignot, E.; Fenty, I.; Xu, Y.; Cai, C.; Velicogna, I.; Ó Cofaigh, C.; Dowdeswell, J.A.; Weinrebe, W.; Catania, G. and Duncan, D. (2016) Bathymetry data reveal glaciers vulnerable to ice-oceaninteraction in Uummannaq and Vaigatglacial jords, west Greenland. *Geophysical Research Letters*, 43(6): pp.2667-2674.

Rignot, E.; Koppes, M. and Velicogna, I. (2010) Rapid submarine melting of the calving faces of West Greenland glaciers. *Nature Geosciences*, 3(3): pp.187-191.

Rippin, D.M.; Pomfret, A. and King, N. (2015) High resolution mapping of supra-glacial drainage pathways reveals link between micro-channel drainage density, surface roughness and surface reflectance. *Earth Surface Processes and Landforms*, 40(10): pp.1279-1290.

Rivera, A.; Corripio, J. G.; Brock, B.; Clavero, J. and Wendt, J. (2008) Monitoring ice-capped active Volćan Villarrica, southern Chile, using terrestrial photography combined with automatic weather stations and global positioning systems. *Journal of Glaciology*, 54(188): pp.920-930.

Russell-Head, D.S. (1980) The melting of free-drifting icebergs. *Annals of Glaciology*, 1(1): pp.119-122.

Ruxton, G.D. (2006) The unequal variance t-test is an underused alternative to Student's t-test and the Mann-Whitney U test. *Behavioural Ecology*, 17(4): pp.688-690.

Ryan, J.C.; Hubbard, A.; Box, J.E.; Brough, S.; Cameron, K.; Cook, J.M.; Cooper, M.; Doyle, S.H.; Edwards, A.; Holt, T.; Irvine-Fynn, T.; Jones, C.; Pitcher, L.H.; Rennermalm, A.K.; Smith, L.C.; Stibal, M. and Snooke, N. (2017) Derivation of High Spatial Resolution Albedo from UAV Digital Imagery: Application over the Greenland Ice Sheet. *Frontiers in Earth Sciences*, 5(40), 13pp.

Ryan, J.C.; Hubbard, A.L.; Box, J.E.; Todd, J.; Christoffersen, P.; Carr, J.R.; Holt, T.O. and Snooke, N. (2015) UAV photogrammetry and structure from motion to assess calving dynamics at Store Glacier, a large outlet draining the Greenland ice sheet. *The Cryosphere*, 9(1): pp.1-11.

Scambos, T.; Ross, R.; Bauer, R.; Yermolin, Y.; Skvarca, P.; Long, D.; Bohlander, J. and Haran, T. (2008) Calving and ice-shelf break-up processes investigated by proxy: Antarctic tabular iceberg evolution during northward drift. *Journal of Glaciology*, 54(187): pp.579-591.

Schuster, R. and Rigsby, G. (1954) Preliminary report on crevasses. *U.S. Army Snow, Ice and Permafrost Research Establishment, Special Report 11*.

Seligman, G. (1955) Comments on crevasse depths. *Journal of Glaciology*, 2(17): p.514.

Shepherd, A.; Hubbard, A.; Nienow, P.; McMillan, M. and Joughin, I. (2009) Greenland ice sheet motion coupled with daily melting in late summer. *Geophysical Research Letters*, 36(1): 4pp.

Showstack, R. (2017) “Map Provides High-Resolution Look at Nearly Entire Arctic Region”, Earth & Space Science News (accessed at: https://eos.org/articles/map-provides-high-resolution-look-at-nearly-entire-arctic-region, viewed 13th January 2018).

Smith, L. A. (2007) *System model of a UAV and sensor package for the measurement of sea ice freeboard, roughness, and topography*. M.S. thesis, University of Colorado Boulder.

Smith, M.W.; Carrivick, J.L and Quincey, D.J. (2016) Structure from motion photogrammetry in physical geography. *Progress in Physical Geography*, 40(2): pp.247-275.

Snavely, N. (2008) *Scene reconstruction and visualization from Internet photo collections*, unpublished PhD thesis, University of Washington: 192pp.

Solbø, S. and Storvold, R. (2013) Mapping Svalbard glaciers with the Cryowing UAS. *International Archives of the Photogrammetry, Remote Sensing and Spatial Information Sciences,* 40(1/W2), ISPRS Rostock Workshop, Germany, 4-6 September 2013: pp.373-377.

Straneo, F.; Hamilton, G.S.; Sutherland, D.A.; Stearns, L.A.; Davidson, F.; Hammill, M.O.; Stenson, G.B. and Rosing-Asvid, A. (2010) Rapid circulation of warm subtropical waters in a major glacial fjord in East Greenland. *Nature Geosciences*, 3(3): pp.182-186.

Straneo, F.; Heimbach, P.; Sergienko, O.; Hamilton, G.; Catania, G.; Griffies, S.; Hallberg, R.; Jenkins, A.; Joughin, I.; Motyka, R.; Pfeffer, W.T.; Price, S.F.; Rignot, E.; Scambos, T.; Truffer, M. and Vieli, A. (2013) Challenges to understanding the dynamic response of Greenland’s marine terminating glaciers to oceanic and atmospheric forcing. *Bulletin of the American Meteorological Society*, 94(8): pp.1131-1144.

Straneo, F.; Sutherland, D.A.; Holland, D.; Gladish, C.; Hamilton, G.S.; Johnson, H.L.; Rignot, E.; Xu, Y. and Koppes, M. (2012) Characteristics of ocean waters reaching Greenland’s glaciers. *Annals of Glaciology*, 53(60): pp.202-210.

Spetsakis, M.E. and Aloimonos, Y. (1991) A multi-frame approach to visual motion perception. *International Journal of Computer Vision*, 6(3): pp.245-255.

Sutherland, D.A. and Straneo, F. Estimating ocean heat transports and submarine melt rates in Sermilik Fjord, Greenland, using lowered acoustic Doppler current profiler (LADCP) velocity profiles. *Annals of Glaciology*, 53(60): pp.50-58.

Szeliski, R. and Kang, S.B. (1994) Recovering 3-D shape and motion from image streams using nonlinear least squares. *Journal of Visual Communication and Image Representation*, 5(1): pp.10-28.

Toberg, N.; Ryan, J.; Christoffersen, C.; Snooke, N.; Todd, J. and Hubbard, A. (2016) Estimating ice-melange properties with repeat UAV surveys over Store Glacier, West Greenland. *EGU General Assembly Conference Abstracts*, vol. 18, no. EPSC2016-16354.

Todd, J. and Christoffersen, P. (2014) Are seasonal calving dynamics forced by buttressing from ice mélange or undercutting by melting? Outcomes from full-Stokes simulations of Store Glacier, West Greenland. *The Cryosphere*, 8(6): pp.2353-2365.

Todd, J.; Christoffersen, P.; Zwinger, T.; Råback, P.; Chauché, N.; Benn, D.; Luckman, A.; Ryan, J.; Toberg, N.; Slater, D. and Hubbard, A. (2018) A full-stokes 3-D calving model applied to a large Greenlandic glacier. *Journal of Geophysical Research: Earth Surface*, 123, doi:10.1002/2017JF004349, 23pp.

Triggs, B.; McLauchlan, P.; Hartley, R. and Fitzgibbon, A. (2000) “Bundle Adjustment – A Modern Synthesis” in Triggs, B.; Zisserman, A. and Szeliski, R. (eds.) *Vision Algorithms: Theory and Practice*, Lecture Notes in Computer Science vol 1883. Berlin: Springer, pp.298-372.

Truffer, M. and Motyka, R. (2016) Where glaciers meet water: Subaqueous melt and its relevance to glaciers in various settings. *Reviews of Geophysics*, 54(1): pp.220-239.

Tschudi, M.A. (2013) Acquisition of Ice Thickness and Ice Surface Characteristics in the Seasonal Ice Zone by CULPIS-X during the US Coast Guard's Arctic Domain Awareness Program. *Public Report, University of Colorado Boulder*: 20pp.

Tschudi, M.A.; Tooth, M. and Barton-Grimley, R.A. (2016) Acquisition of Airborne Sea Ice Remote Sensing Data with CULPIS-X: An Instrument Mounted on a US Coast Guard C-130. *Proceedings of the American Geophysical Union Fall General Assembly*, Abstract No.C43D-04.

Ultee, L. and Bassis, J. (2016) The future is Nye: An extension of the perfect plastic approximation to tidewater glaciers. *Journal of Glaciology*, 62(236): pp.1143-1152.

van As, D.; Hubbard, A. L.; Hasholt, B.; Mikkelsen, A. B.; van den Broeke, M. R. and Fausto, R. S. (2012) Large surface meltwater discharge from the Kangerlussuaq sector of the

Greenland ice sheet during the record-warm year 2010 explained by detailed energy balance observations. *The Cryosphere*, 6(1): pp.199-209.

van de Wal, R.S.W.; Smeets, C.J.P.P.; Boot, W.; Stoffelen, M.; van Kampen, R.; Doyle, S.H.; Wilhelms, F.; van den Broeke, M.R.; Reijmer, C.H.; Oerlemans, J. and Hubbard, A. (2015) Self-regulation of ice flow varies across the ablation area in South-West Greenland. *The Cryosphere*, 9(2): pp.603-611.

van den Broeke, M.; Bamber, J.; Ettema, J.; Rignot, E.; Schrama, E.; van de Berg, W.J.; van Meijgaard, E.; Velicogna, I. and Wouters, B. (2009) Partitioning recent Greenland mass loss. *Science*, 326(5955): pp.984-986.

van den Broeke, M. R.; Smeets, C. J. P. P. and van de Wal, R. S. W. (2011) The seasonal cycle and interannual variability of surface energy balance and melt in the ablation zone of the west Greenland ice sheet. *The Cryosphere*, 5(2): pp.377-390.

van der Veen, C.J (1998a) Fracture mechanics approach to penetration of surface crevasses on glaciers. *Cold Regions Science and Technology*, 27(1): pp.31-47.

van der Veen, C.J (1998b), Fracture mechanics approach to penetration of bottom crevasses on glaciers. *Cold Regions Science and Technology*, 27(3): pp.213-223.

van der Veen, C.J (1999a) Crevasses on glaciers. *Polar Geography*, 23(3): pp.213-245.

van der Veen, C.J. (2013) *Fundamentals of Glacier Dynamics*, 2nd edition. Boca Raton, Florida, USA: CRC Press, 403pp.

Velicogna, I. (2009) Increasing rates of ice mass loss from the Greenland and Antarctic ice sheets revealed by GRACE. *Geophysical Research Letters*, 36(19): 4pp.

Velicogna, I. and Wahr, J. (2006) Acceleration of Greenland ice mass loss in spring 2004. *Nature*, 443(7109): pp.329-331.

Vieli, A. and Nick, F.M. (2011) Understanding and modelling rapid dynamic changes of tidewater outlet glaciers: issues and implications. *Surveys in Geophysics*, 32(4-5): pp.437-458.

von Bueren, S.; Burkart, A.; Hueni, A.; Rascher, U.; Tuohy, M. and Yule, I. (2015) Deploying four optical UAV-based sensors over grassland: challenges and limitations. *Biogeosciences*, 12(1): pp.163-175.

Vornberger, P. and Whillans, I. (1990) Crevasse deformation and examples from Ice Stream B, Antarctica. *Journal of Glaciology*, 36(122): pp.3-10.

Wagner, T.; James, T.; Murray, T. and Vella, D. (2016) On the role of buoyant flexure in glacier calving. *Geophysical Research Letters*, 43(1): pp.232-240A.

Walter, J.I.; Jason, E.; Tulaczyk, S.; Brodsky, E.E.; Howat, I.M.; Yushin, A.H.N. and Brown, A. (2012) Oceanic mechanical forcing of a marine-terminating Greenland glacier. *Annals of Glaciology*, 53(60): pp.181-192.

Warren, C.R. and Kirkbride, M.P. (2003) Calving speed and climatic sensitivity of New Zealand lake-calving glaciers. *Annals of Glaciology*, 36(1): pp.173-178.

Warren, C.R.; Benn, D.I.; Winchester, V. and Harrison, S. (2001) Buoyancy-driven lacustrine calving, Glacier Nef, Chilean Patagonia. *Journal of Glaciology*, 47(156); pp.135-146.

Warren, C.R.; Glasser, N.F.; Harrison, S.; Winchester, V.; Kerr, A.R. and Rivera, A. (1995) Characteristics of tide-water calving at Glaciar San Rafael, Chile. *Journal of Glaciology*, 41(138): pp.273-289.

Watson, C.S.; Quincey, D.J.; Smith, M.W.; Carrivick, J.L.; Rowan, A.V.; James, M.R. (2017) Quantifying ice cliff evolution with multi-temporal point clouds on the debris-covered Khumbu Glacier, Nepal. *Journal of Glaciology*, 63(241): pp.823-837.

Weertman, J. (1973) Can a water-filled crevasse reach the bottom surface of a glacier? *IASH Publications*, 95(1): pp.139-145.

Weertman, J. (1974) Stability of the junction of an ice sheet and an ice shelf. *Journal of Glaciology*, 13(67): pp.3-11.

Weidick, A. (1968) *Observations on Some Holocene Glacier Fluctuations in West Greenland*. Copenhagen: C. A. Reitzel, 203pp.

Weidick, A. (1972) Holocene shorelines and glacial stages in Greenland – an attempt at correlation. *Grønlands Geologiske Undersøgelse*, 41(1): pp.1-39.

Weidick, A. (1995) “Greenland, with a section on Landsat images of Greenland” in Williams, R.S. and Ferrigno, J.G. (eds.) *Satellite image atlas of glaciers of the world*, USGS Professional Paper 1386-C. Washington, D.C.: US Geological Survey.

Weidick, A. and Bennike, O. (2007) Quaternary glaciation history and glaciology of Jakobshavn Isbræ and the Disko Bugt region, West Greenland: a review. *Geological Survey of Denmark and Greenland Bulletin 14*, 78pp.

Weidick, A.; Kelly, M. and Bennike, O. (2004) Late Quaternary development of the southern sector of the Greenland Ice Sheet, with particular reference to the Qassumiut lobe. *Boreas*, 33(4): pp.284-299.

Welch, B.L. (1947) The generalisation of 'student's' problem when several difference population variances are involved. *Biometrika*, 34(1-2): pp.28-35.

Wester-Ebbinghaus, W. (1980) Aerial photography by radio controlled model helicopter. *The Photogrammetric Record*, 10(55): pp.85-92.

Westoby, M.J.; Brasington, J.; Glasser, N.F.; Hambrey, M.J. and Reynolds, J.M. (2012) 'Structure-from-Motion' photogrammetry: A low-cost, effective tool for geoscience applications. *Geomorphology*, 179(1): pp.300-314.

Wiscombe, W. J. and Warren, S. G. (1980) A model for the spectral albedo of snow. I: Pure snow. *Journal of Atmospheric Sciences*, 37(12): pp.2712-2733.

Williams, K.M. (1993) Ice sheet and ocean interactions, margin of the East Greenland ice sheet (14ka to present): diatom evidence. *Palaeoceanography*, 8(1): pp.69-83.

Whitehead, K.; Moorman, B.J. and Hugenholtz, C.H. (2013) Brief Communication: Low-cost, on-demand aerial photogrammetry for glaciological measurement. *The Cryosphere*, 7(6): pp.1879-1884.

Wolf, P.R.; Dewitt, B.A. and Wilkinson, B.E. (2014) *Elements of Photogrammetry with Applications in GIS*, 4th edition. Boston: McGraw-Hill Education, 696pp.

Wu, C. (2014) Critical configurations for radial distortion self-calibration. *IEEE Conference on Computer Vision and Pattern Recognition (CVPR), Columbus, USA*, pp.25-32.

Xie, S.; Dixon, T.H.; Voytenko, D.; Holland, D.M.; Holland, D. and Zheng, T. (2016) Precursor motion to iceberg calving at Jakobshavn Isbræ, Greenland, observed with terrestrial radar interferometry. *Journal of Glaciology*, 62(236): pp.1134-1142.

Zwally, H.J.; Abdalati, W.; Herring, T.; Larson, K.; Saba, J. and Steffen, K. (2002a) Surface melt-induced acceleration of Greenland ice-sheet flow. *Science*, 297(5579): pp.218-22, doi:10.1126/science.1072708, 2002.

Zwally, H.; Schutz, B.; Abdalati, W.; Abshire, J.; Bentley, C.; Brenner, A.; Bufton, J.; Dezio, J.; Hancock, D.; Harding, D.; Herring, T.; Minster, B.; Quinn, K.; Palm, S.; Spinhirne, J. and Thomas, R. (2002b) ICESat's laser measurements of polar ice, atmosphere, ocean, and land. *Journal of Geodynamics*, 34(3/4): pp.405-445.

Appendix 1: Survey 10_1 Fixed Transect Crevasse Orientation Rose Diagrams

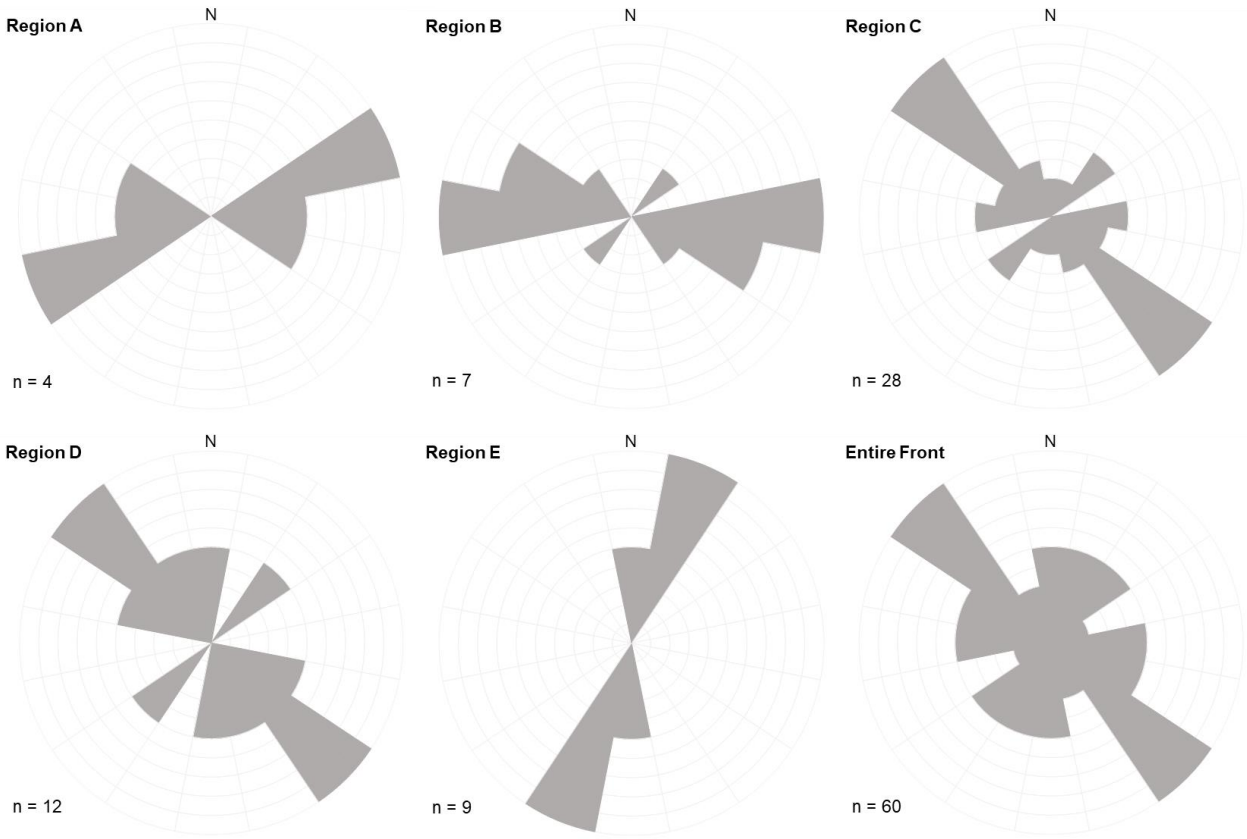

Appendix 2: Survey 14_1 Fixed Transect Crevasse Orientation Rose Diagrams

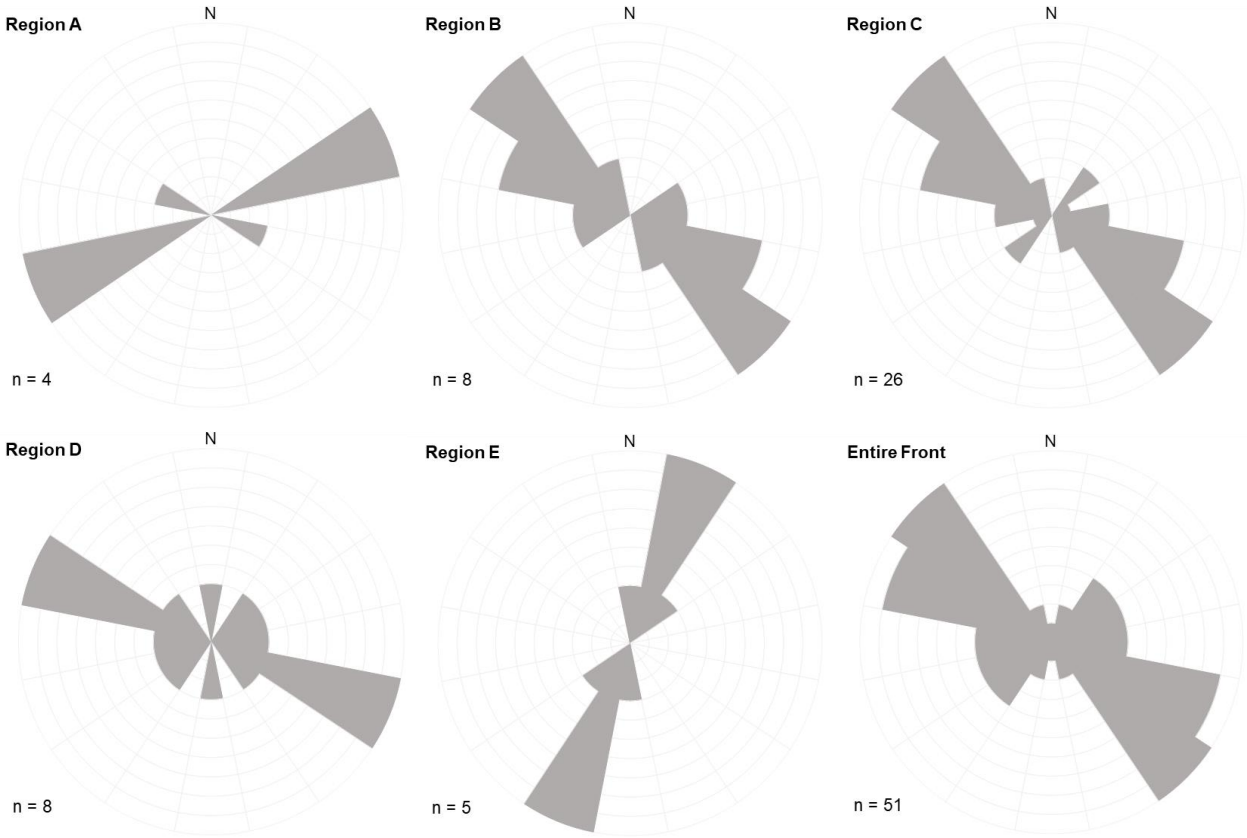

Appendix 3: Survey 10_1 Moving Transect Crevasse Orientation Rose Diagrams

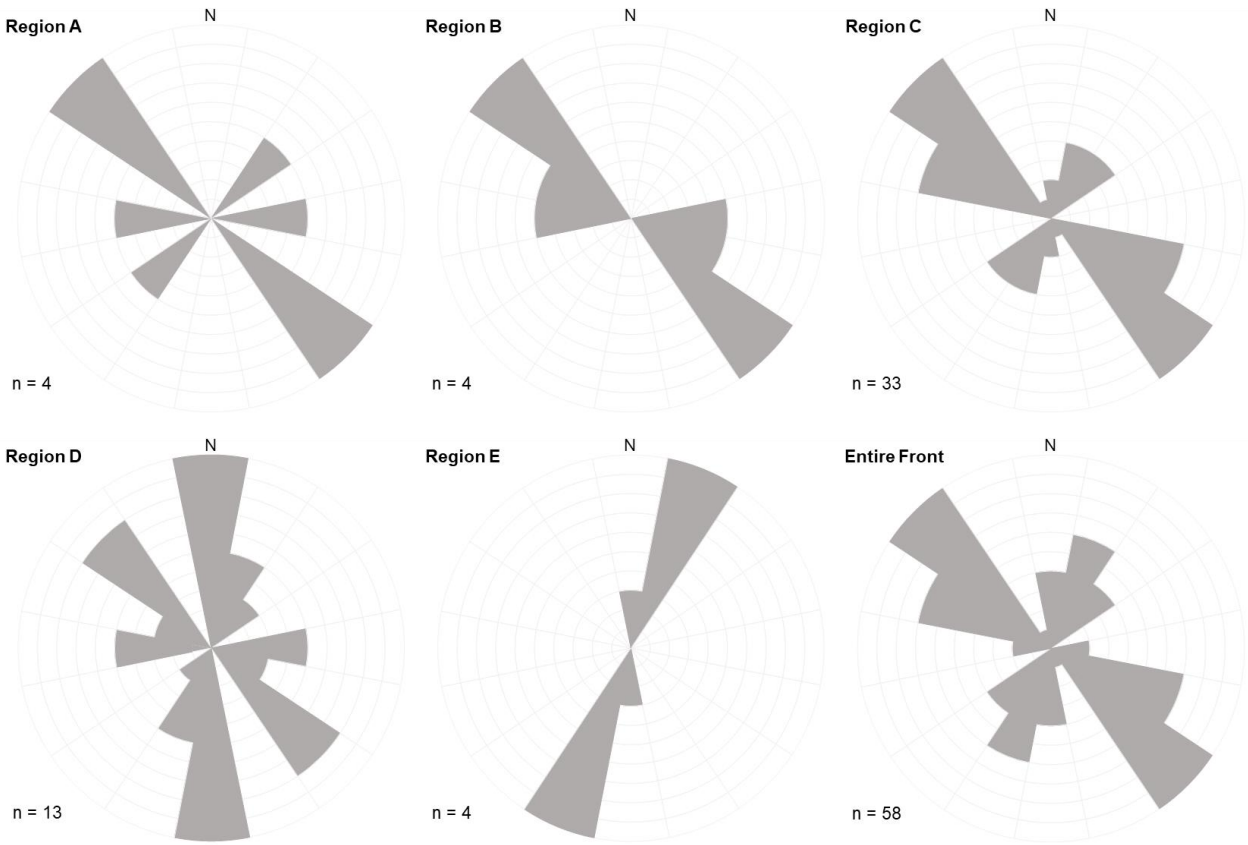

Appendix 4: Survey 10_1 Moving Transect Crevasse Orientation Rose Diagrams

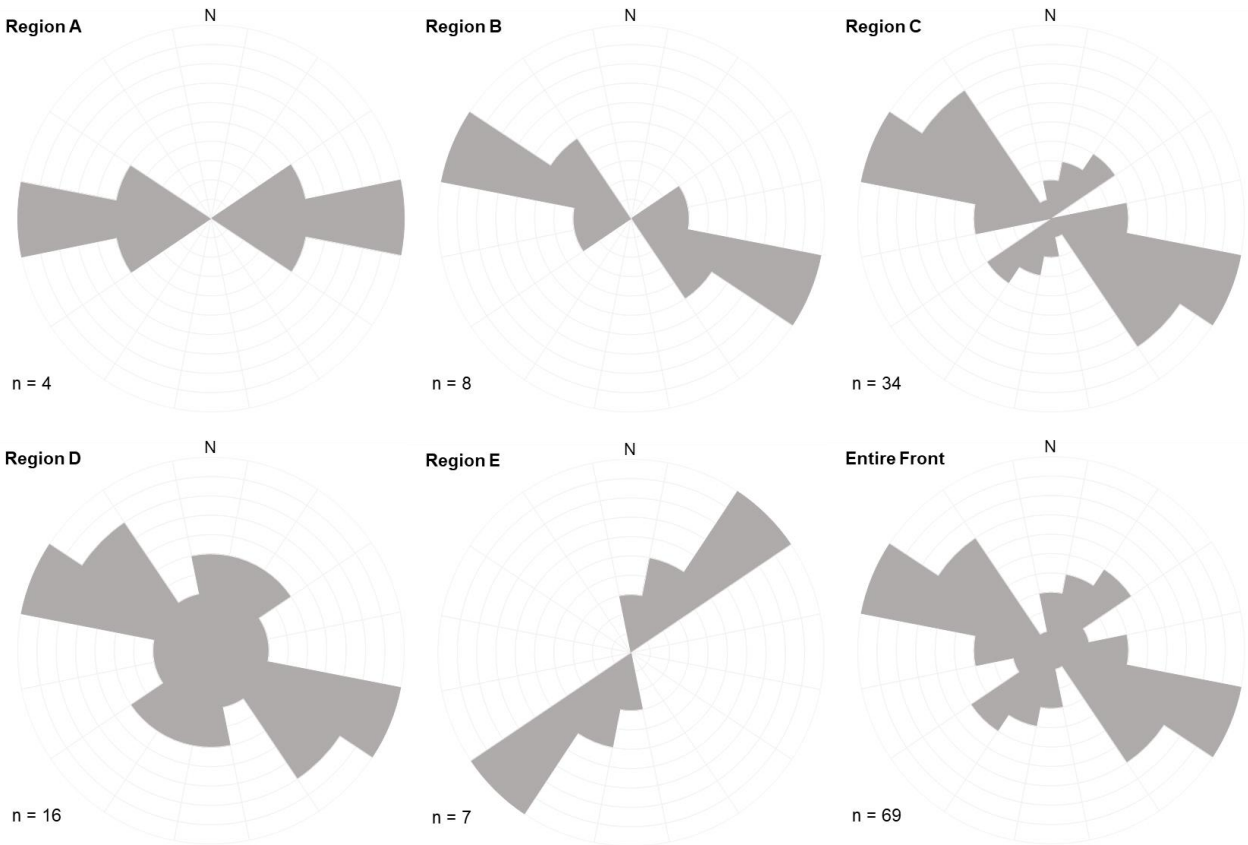

Appendix 5: Transect 1 Depth Profiles

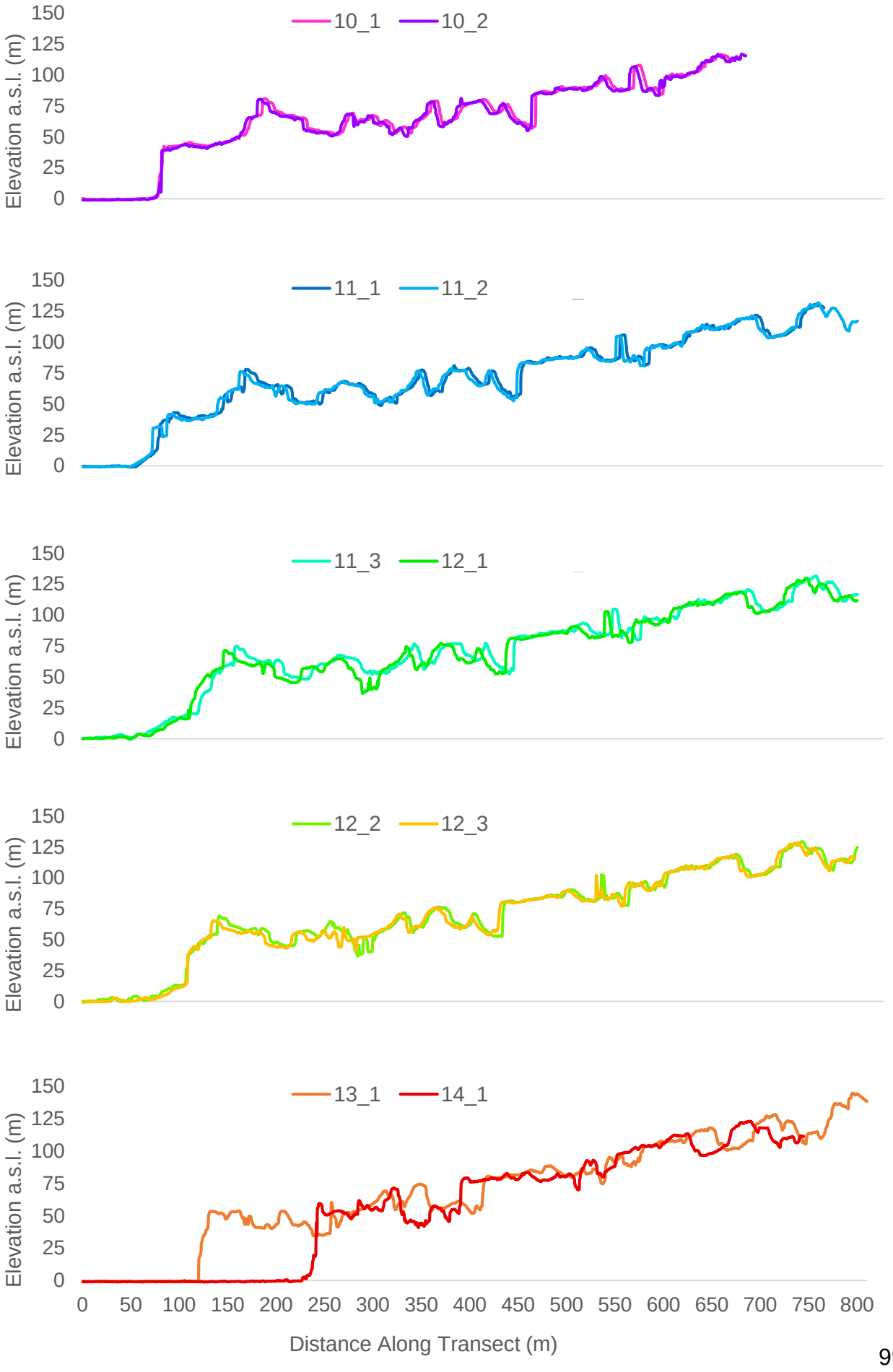

Appendix 6: Transect 2 Depth Profiles

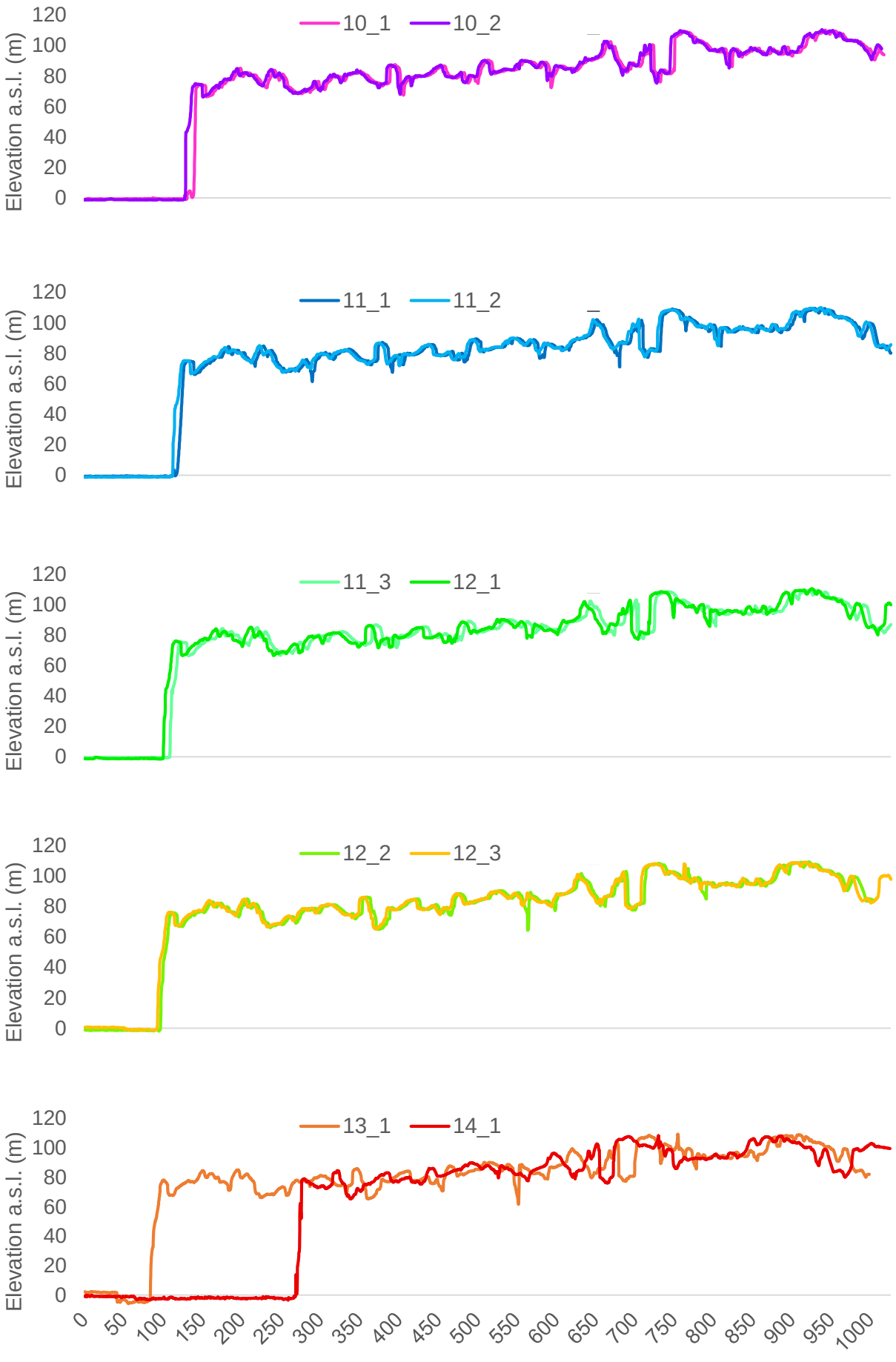

Appendix 7: Transect 3 Depth Profiles

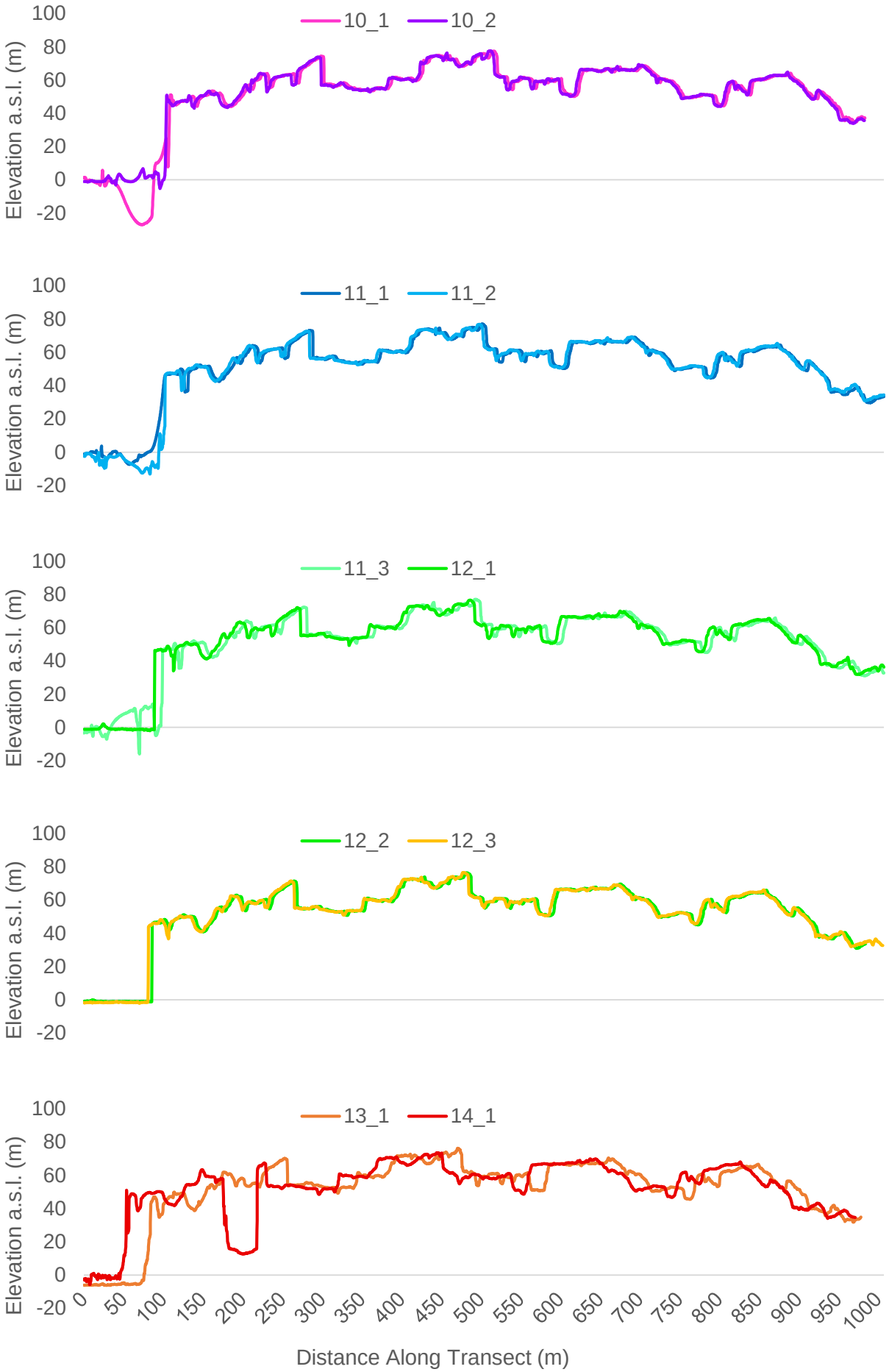

Appendix 8: Transect 4 Depth Profiles